Master Thesis

Gravitational Redshift of Clusters in the Symmetron and Chameleon $f(R)$ Models

Max Grönke

June 2013

Institute of Theoretical Astrophysics
University of Oslo

Abstract

The gravitational redshift in clusters of galaxies can be measured to probe gravity as was first done by Wojtak et al. (2011). Using N-body simulations we are able to analyze the gravitational redshift profiles for the symmetron and the Hu-Sawicky $f(R)$ models. The characteristic feature of these models is the screening mechanism that hides the fifth force in dense environments recovering general relativity. We find that due to the nature of the screening, the deviation with respect to ΛCDM is highly dependent on the halo mass. So the $f(R)$ parameters $|f_{R0} - 1| = 10^{-5}$, $n = 1$ cause an enhancement of the gravitational signal by up to 60% for halos with masses between $3 \times 10^{12}\, M_{\odot} h^{-1}$ and $10^{14}\, M_{\odot} h^{-1}$. However, for both larger and smaller halos there is hardly any deviation present. The characteristic mass range, where the fifth force is most active, varies with the model parameters. Additionally, we observe not only a stronger but also a possible weaker gravitational redshift. This contradicts the usual assumption that the presence of a fifth force leads to a deeper potential well but may happen if screening in the central regions is active which results in a shift of the additional clustering to larger radii.

Acknowledgment

First, I would like to thank my two supervisors, David F. Mota and Claudio Llinares, for their valuable help and their support throughout my thesis. I am thankful to David F. Mota for the trust he put in me by giving me an exciting and challenging thesis topic.

A special thanks goes to Claudio Llinares, who devoted his time and energy to help me proceeding with my work, even whilst abroad. He also read through my thesis and gave me very constructive feedback.

I would also like to thank all the people I have been working with throughout this thesis and, especially, to Hans A. Winther for the numerous discussions and answers he provided to my stupid questions.

In addition, I am grateful to Rahel Frick, Andres Spicher and Michael Küffmeier for reading through my thesis and giving me feedback.

Moreover, thanks to my family for supporting me and helping me financially to pursue my studies in Oslo. Thanks also to my friends and fellow students, especially Elisabeth Jordahl and Eunseong Lee, for making this time particularly pleasant.

Contents

Introduction 1
Overview . . . 2
Notation and conventions . . . 3

1 Preliminaries 5
1.1 General relativity in a nutshell . . . 5
1.1.1 The Einstein-Hilbert action . . . 6
1.1.2 Gravitational redshift . . . 7
1.1.3 The Friedmann equations . . . 8
1.2 Dark energy . . . 10
1.2.1 ΛCDM . . . 10
1.2.2 Quintessence . . . 11
1.2.3 Einstein and Jordan frame . . . 12
1.2.4 Scalar-tensor theories . . . 13
1.2.5 $f(R)$-gravity . . . 14
1.2.6 $f(R)$-gravity as a scalar-tensor theory . . . 16

2 Review of the Chameleon and Symmetron Models 18
2.1 Introduction to the chameleon mechanism . . . 19
2.1.1 The chameleon in outer space . . . 21
2.1.2 The chameleon close to masses . . . 22
2.2 The symmetron model . . . 24
2.2.1 Cosmology . . . 25
2.2.2 Spherical solution . . . 26
2.3 The Hu-Sawicky $f(R)$ model . . . 27
2.4 Gravitational redshift in the symmetron and chameleon models . . . 30

3 The N-body Code and Simulation Parameters 32
3.1 Introduction to N-body simulations . . . 32
3.1.1 Concepts . . . 32
3.1.2 Gravity calculation . . . 34
3.2 The simulation code . . . 37
3.2.1 RAMSES code structure . . . 37

3.2.2 The ISIS code . . . 37
3.3 Simulation parameters . . . 39
3.4 Post-processing: Identifying the halos . . . 40

4 Spherical Collapse and Virialization 43
4.1 Derivation of the virialization equation . . . 43
4.2 Spherical collapse in standard models . . . 47
4.2.1 Einstein-de Sitter universe . . . 47
4.2.2 ΛCDM model . . . 48
4.3 Spherical collapse in screened modified gravity . . . 51
4.3.1 Symmetron implementation . . . 53
4.3.2 $f(R)$ implementation . . . 60
4.3.3 Conclusions of the spherical collapse model . . . 61
4.4 Virialization state in N-body simulations . . . 62
4.4.1 Virialization parameter in scalar-tensor theories . . . 68

5 Gravitational Redshift in Screened Modified Gravity 69
5.1 Obtaining the gravitational redshift . . . 69
5.2 The NFW profile . . . 70
5.3 Uncertainty estimation . . . 71
5.4 Cluster profiles in the ΛCDM model . . . 74
5.5 The $f(R)$ models . . . 75
5.5.1 Matter power spectra and halo mass functions . . . 75
5.5.2 Chameleons in the wild: The fifth force unbound . . . 76
5.5.3 Gravitational redshift profiles . . . 79
5.5.4 The halo density profiles . . . 82
5.5.5 Velocity profiles . . . 83
5.6 The symmetron models . . . 85
5.6.1 Matter power spectra and halo mass functions . . . 85
5.6.2 Symmetron additional force . . . 86
5.6.3 Gravitational redshift profiles . . . 88
5.6.4 Halo density profiles . . . 89
5.6.5 Velocity profiles . . . 90
5.7 Connection to observational data . . . 92
5.8 Systematic effects . . . 94
5.9 Summary of results . . . 95

6 Conclusions 98
6.1 Outlook . . . 99

A Appendix 101
A.1 Derivation of the Klein-Gordon equation . . . 101
A.2 Gauss Seidel method with successive overrelaxation . . . 101

Bibliography 104

Introduction

Although there is overwhelming evidence that dark energy exists (see Amendola & Tsujikawa (2010, Chap. 5) or Wang (2009, Chap. 4-7) for observational aspects), its nature is still a mystery. There are two possible explanations for this: Either dark energy is some type of yet unknown matter or general relativity is not fully correct and therefore requires some modification which can account for the phenomena attributed to dark energy.

In the first approach, the new matter would have to possess an equation of state equal or close to -1 and its detection would be a milestone of particle physics. In this case, the presently well-known problems of such a cosmological constant solution, namely the coincidence and fine-tuning problem, would be uncovered as midleading hints.

Pursuing the second approach, often titled the modification of gravity, intense efforts were made in order to establish new theories (see e.g. Clifton et al. (2012) for a theoretical overview). The main problems concerning the development of new gravitational theories are of theoretical, like the existence of ghosts, as well as observational kind, meaning the experimental constraints from local experiments are very tight. One explanation for the possibly undiscovered variations are so-called screening mechanisms, where the local constraints are fulfilled because of the additional force is hidden in dense environments such as the solar system.

In this work, two models with screening are discussed: The symmetron model (Hinterbichler & Khoury, 2010) and an $f(R)$-gravity model that uses chameleon screening (Hu & Sawicki, 2007). The first model works through the dependency of the vacuum expectation value of the scalar field on the local matter density, whereas in the latter, the mass of the scalar field is linked to the matter density. Both mechanisms result in the same outcome: In low-density regions, a fifth force is mediated and in high-density regions this force is suppressed. This behavior requires astrophysical tests in order to examine the existence of these scalar fields.

Due to the non-linearity of the screening, N-body simulations are a preferable tool to make observational predictions. For both models, this has been done before (in the symmetron case by Brax et al. (2012), Davis et al. (2011) and Winther et al. (2011) and in the chameleon case by Brax et al. (2013), Li et al. (2012), Li & Hu (2011) and Zhao et al. (2011)) with a focus on large scale imprints (i.e. mostly the deviation in the matter power spectra and halo mass functions were analyzed). In this work, the `ISIS` code (Llinares et al., 2013) was used

to perform a total of 8 simulation runs over a variety of model parameters. The resolution obtained through 512^3 particles in a $256\,\mathrm{Mpc\,h^{-1}}$ box allows us to analyze deviations in halo properties such as the density or velocity dispersion profiles. These observables can be analyzed using lensing (Johnston & Sheldon, 2007; Oguri et al., 2012; Okabe et al., 2013). Possible constraints for the $f(R)$ model have been established by Lombriser et al. (2012) and Schmidt (2010).

Another possible test of gravity scales below 1 Mpc is the use of gravitational redshift, as the wavelength shift of light is directly proportional to the depth of the potential well of the clusters of galaxies. This has been observed for the SDSS survey data by Wojtak et al. (2011) who compared the data points to analytical prediction for general relativity based on the NFW-profile (Navarro et al., 1995), an analytical TeVeS prediction[1] and a semi-analytical profile from Schmidt (2010). For the latter, the NFW prediction has been boosted by the factor 4/3 which is the maximum enhancement of gravitational strength according to $f(R)$ gravity.

We simulate gravitational redshift profiles of clusters in the three gravitational models and show that such comparisons and predictions have to be made with extreme caution when dealing with screening models. The main reason for this is that the deviation may not occur with the same strength in all mass and length scales with the same strength. In particular, three kind of effects were observed: *(i)* An enhanced gravitational redshift profile, which is linked to additional clustering in the center of halos; *(ii)* a weakened effect, pointing to clustering in the outskirts, or *(iii)* no deviation from ΛCDM if the additional force is screened in this regime.

When doing a comparison of cluster properties, it is essential we only study dynamical relaxed objects. Therefore, a big part of this work is about sample selection and virialization, as for scalar-tensor theories the potential energy of the scalar field has to be taken into account as well when determining the virialization state.

Overview

The first part of this work is meant to give a rough introduction to the subject: First, the theory of general relativity and the possibility of its derivation from the Einstein-Hilbert action are revised. Then, the "dark energy problem" is briefly summarized and scalar fields as a possible solution as well as the link to $f(R)$ models are presented. Here, focus is put on the the two screening mechanisms analyzed in this work: The chameleon and the symmetron models, where insights are given as to how the screening in these two cases works. Also, the Hu-Sawicky model is shown to be a chameleon theory.

In the second part, the approach chosen for this work, namely the use of N-body simulations in order to find possible imprints of the modified gravity theories on smaller scales, is

1 The analytical TeVeS profile used was later shown to be based on inappropriate assumptions (Bekenstein & Sanders, 2012).

discussed. In particular, the sample selection and the problematics of virialization of halos is laid out. This is specifically done by applying the spherical collapse model to the symmetron and $f(R)$ case.

Finally, the output from the N-body simulation is presented and discussed with a focus on the variation in the gravitational redshift profiles. The results obtained are also compared against current measurements.

Notation and conventions

Throughout this work units were used so that $c = \hbar = 1$, except in some cases when the symbols are added for clarity. This means all the units can be expressed in terms of energy and the following conversions from SI units apply:

$$\begin{aligned} 1\,\text{meter} &= 5.068 \times 10^{-39}\,\text{GeV}^{-1} \\ 1\,\text{second} &= 1.519 \times 10^{24}\,\text{GeV} \\ 1\,\text{kilogram} &= 5.610 \times 10^{26}\,\text{GeV} \end{aligned}$$

The metric signature adopted is $(-,+,+,+)$ and the Einstein summation convention applies with Greek indices running from 0 to 3 and Latin indices from 1 to 3. In addition, a subscript $_0$ usually refers to the value today.

List of frequently used symbols

Symbol	Name	Definition or Value
G	Gravitational constant	$G = 6.71 \times 10^{-39}\,\text{GeV}^{-2}$
M_{Pl}	Reduced Planck mass	$M_{\text{Pl}} = 1/\sqrt{8\pi G} = 2.44 \times 10^{18}\,\text{GeV}$
$M_\odot$	Mass of Sun	$M_\odot = 1.99 \times 10^{30}\,\text{kg}$
c	Speed of light	$c = 1$
$\hbar$	Reduced Planck constant	$\hbar = 1$
a	Cosmic scale factor, normalized to unity today	
H	Hubble parameter	$H = \dot{a}/a$
ρ	(Energy) density	
p	pressure	
w	Equation of state	$w = p/\rho$
ρ_c	Critical density of the universe	$\rho_c = 3H^2 M_{\text{Pl}}^2 = 3H^2/(8\pi G)$
Ω_i	Relative density	$\Omega_i = \rho_i/\rho_{c,0}$
Φ	Newtonian gravitational potential	
z_g, v_g	Gravitational redshift	$v_g = z_g c$
ϕ	Scalar field	
β	Dimensionless coupling constant	

List of frequently used symbols – continued from previous page

Symbol	Name	Definition or Value
$\dot{}$	Derivative with respect to time	
$_{,\mu}$, ∂_μ	Partial derivative with respect to x^μ	$\partial_\mu = \partial/\partial x^\mu$
$_{,\phi}$, ∂_ϕ	Partial derivative with respect to ϕ	$\partial_\phi = \partial/\partial\phi$
$_{;\mu}$, ∇_μ	Covariant derivative with respect to x^μ	
$\Box$	D'Alembert operator	$\Box = \nabla_\mu \nabla^\mu$
∇, $\vec{\nabla}$	Del- or Nabla-Operator in three spatial dimensions	
$g_{\mu\nu}$	Metric tensor	
$\eta_{\mu\nu}$	Minkowsky tensor	$\eta = \mathrm{diag}(-1,1,1,1)$
$\Gamma^\alpha_{\mu\nu}$	Christoffel symbols	
$R_{\mu\nu}$	Ricci tensor	
R	Ricci scalar	
$G_{\mu\nu}$	Einstein Tensor	
$T_{\mu\nu}$	Energy momentum tensor	
W	Potential energy	
T	Kinetic energy	
E_S	Surface pressure term	
β_{vir}	Virialization parameter	$\beta_{vir} \equiv (2T - E_s)/W + 1$
R_{vir}, R_v	Virial radius	

1

Preliminaries

This chapter gives a short introduction to the mathematical basics needed further on. First, the theory of relativity is discussed in brief and the possibility of its derivation from the Einstein-Hilbert action is mentioned as the same procedure is followed later on for modified actions. Also, the cause of gravitational redshift and the Friedmann equations are given as a bonus. Secondly, some dark energy models are presented with focus on scalar-tensor theories and $f(R)$ gravity since the models analyzed in this work are of this type.

1.1 General relativity in a nutshell

It is not the aim of this work to have the character of a book. Therefore, this section is merely a listing of equations used in a later section for completeness. The books of Carroll (2004), Hartle (2003) and Misner et al. (1973) were used as reference and are recommended as a proper introduction to the general theory of relativity.

Starting with a metric tensor $g_{\mu\nu}$ describing the line element in a 4-dimensional spacetime $\mathrm{d}s^2 = g_{\mu\nu}x^\mu x^\nu$, the Christoffel symbols are defined as

$$\Gamma^\alpha_{\mu\nu} \equiv \frac{g^{\alpha\sigma}}{2}\left(g_{\mu\sigma,\nu} + g_{\nu\sigma,\mu} - g_{\mu\nu,\sigma}\right) \ . \tag{1.1}$$

The Ricci tensor can be obtained:

$$R_{\mu\nu} = \Gamma^\alpha_{\mu\nu,\alpha} - \Gamma^\alpha_{\mu\alpha,\nu} + \Gamma^\alpha_{\mu\nu}\Gamma^\beta_{\alpha\beta} - \Gamma^\alpha_{\mu\beta}\Gamma^\beta_{\alpha\nu} \ . \tag{1.2}$$

The contraction thereof gives the Ricci scalar:

$$R = R^\mu_\mu = g^{\mu\nu}R_{\mu\nu} \ . \tag{1.3}$$

The Einstein equations can then be written as

$$R_{\mu\nu} - \frac{g_{\mu\nu}}{2}R = 8\pi G T_{\mu\nu} \tag{1.4}$$

or, by defining the Einstein tensor as $G_{\mu\nu} \equiv R_{\mu\nu} - g_{\mu\nu}R/2$ and $\kappa = 8\pi G$ one can obtain a more compact version:

$$G_{\mu\nu} = \kappa T_{\mu\nu} \tag{1.5}$$

The tensor $T_{\mu\nu}$ on the right hand side of the equation is the the energy-momentum tensor, which for a perfect fluid takes the form

$$T_{\mu\nu} = (\rho + p)u_\mu u_\nu + p g_{\mu\nu} \ . \tag{1.6}$$

Here p is the pressure, ρ the density and u^μ the 4-velocity of the fluid.

1.1.1 The Einstein-Hilbert action

Equation (1.5) can also be recovered by varying the Einstein-Hilbert action given by

$$S_{EH} = \int \mathrm{d}^4x \, \frac{\sqrt{-g}}{2\kappa} R \tag{1.7}$$

and the action of the matter fields S_m with respect to the metric $g_{\mu\nu}$:

$$\delta S = \frac{1}{2\kappa} \int \mathrm{d}^4x \, \left[\delta(\sqrt{-g})R + \sqrt{-g}\,(\delta g^{\mu\nu} R_{\mu\nu} + g^{\mu\nu}\delta R_{\mu\nu})\right] + \delta S_m \tag{1.8}$$

Note that g is the determinant of $g_{\mu\nu}$ and therefore $\delta(\sqrt{-g}) = -\frac{1}{2}\sqrt{-g} g_{\mu\nu}\delta g^{\mu\nu}$. This can be derived by writing the determinant as $g = g_{\mu\nu}\mathcal{M}^{(\mu\nu)}$, with the determinant of the cofactor matrix $\mathcal{M}^{(\mu\nu)}$ not depending on $g_{\mu\nu}$.

The variation of the Ricci tensor (defined in equation (1.2)) yields

$$\delta R_{\mu\nu} = \delta\Gamma^\alpha_{\mu\nu,\alpha} - \delta\Gamma^\alpha_{\mu\alpha,\nu} + \delta\Gamma^\alpha_{\mu\nu}\Gamma^\beta_{\alpha\beta} + \Gamma^\alpha_{\mu\nu}\delta\Gamma^\beta_{\alpha\beta} - \delta\Gamma^\alpha_{\mu\beta}\Gamma^\beta_{\alpha\nu} - \Gamma^\alpha_{\mu\beta}\delta\Gamma^\beta_{\alpha\nu} \ . \tag{1.9}$$

Comparing this term with the covariant derivative of $\delta\Gamma^\alpha_{\mu\nu}$, which is – as the difference between two connection symbols – a tensor and, therefore, given by

$$\delta\Gamma^\alpha_{\mu\nu;\gamma} = \delta\Gamma^\alpha_{\mu\nu,\gamma} + \Gamma^\alpha_{\sigma\gamma}\delta\Gamma^\sigma_{\mu\nu} - \Gamma^\sigma_{\mu\gamma}\delta\Gamma^\alpha_{\sigma\nu} - \Gamma^\sigma_{\gamma\nu}\delta\Gamma^\alpha_{\mu\sigma} \tag{1.10}$$

a much simpler expression for $\delta R_{\mu\nu}$ can be found:

$$\delta R_{\mu\nu} = \delta\Gamma^\alpha_{\mu\nu;\alpha} - \delta\Gamma^\alpha_{\mu\alpha;\nu} \ . \tag{1.11}$$

Thus, the whole variation of the Ricci scalar is

$$\begin{aligned}
\delta R &= R_{\mu\nu}\delta g^{\mu\nu} + g^{\mu\nu}\delta R_{\mu\nu} && (1.12)\\
&= R_{\mu\nu}\delta g^{\mu\nu} + g^{\mu\nu}\left(\delta\Gamma^\alpha_{\mu\nu;\alpha} - \delta\Gamma^\alpha_{\alpha\mu;\nu}\right) && (1.13)\\
&= R_{\mu\nu}\delta g^{\mu\nu} + \left(g^{\mu\nu}\delta\Gamma^\alpha_{\mu\nu} - g^{\mu\alpha}\delta\Gamma^\nu_{\mu\nu}\right)_{;\alpha} \ . && (1.14)
\end{aligned}$$

In the last equality the fact that the covariant derivative of the metric is zero ($g_{\mu\nu;\alpha} = 0$) has been applied.

Consequently, using the Gauss' theorem, the last term of (1.8) vanishes if the variation of the metric goes to zero at infinity and we are left with

$$\delta S = \frac{1}{2\kappa} \int \mathrm{d}^4x \sqrt{-g} \left[R_{\mu\nu} - \frac{1}{2} R g_{\mu\nu} - \kappa T_{\mu\nu} \right] \delta g^{\mu\nu} \ . \tag{1.15}$$

Here the definition of the energy-momentum tensor

$$\delta S_m = -\frac{1}{2} \int \mathrm{d}^4x \sqrt{-g} T_{\mu\nu} \delta g^{\mu\nu} \tag{1.16}$$

has been used. Using the Lagrangian density, Eq. (1.16) can be rewritten as

$$T_{\mu\nu} = -\frac{2}{\sqrt{-g}} \frac{\delta \mathcal{L}_m}{\delta g^{\mu\nu}} \ . \tag{1.17}$$

Demanding the action principle $\delta S = 0$, results in Eq. (1.5).

1.1.2 Gravitational redshift

The picture often referred to is that photons lose energy as they have to "climb out" of potential wells caused by the bending of space-time due to the existence of matter. The following section provides the mathematical background to this.

First note that in general the quantity

$$\boldsymbol{\xi} \cdot \mathbf{p} = g_{\mu\nu} \xi^\mu p^\nu \tag{1.18}$$

is conserved (Hartle, 2003, Chap. 8) with $\boldsymbol{\xi}$ being the Killing vector and $\mathbf{p}$ the four-momentum. The four-momentum consists of the energy and the classical three-momentum, i.e.: $p^\mu = (E,\vec{p})$ and the Killing vector is a normalized vector that points in the direction in which the metric is preserved. In the following we will assume a time-independent metric and therefore the Killing vector is $\xi^\mu = (1,0,0,0)$. In addition, the assumption $g_{0i} = 0$ is made.

As the four-velocity is normalized ($u_\mu u^\mu = -1$) and we assume a stationary observer ($u^i = 0$), we obtain for the time component:

$$u^0_{\mathrm{obs}} = \frac{1}{\sqrt{-g_{00}}} \ . \tag{1.19}$$

This means, the energy of a photon received by the observer, which is in general given by $E = -\mathbf{p} \cdot \mathbf{u}$, becomes

$$E_{\mathrm{obs}} = (-g_{00})^{-1/2} (\boldsymbol{\xi} \cdot \mathbf{p})_{\mathrm{obs}} \ . \tag{1.20}$$

Using the conservation of $\boldsymbol{\xi} \cdot \mathbf{p}$ stated above and $E = h/\lambda$, we obtain for the redshift:

$$z \equiv \frac{\lambda_{\mathrm{obs}}}{\lambda_\star} - 1 = \sqrt{\frac{(g_{00})_\star}{(g_{00})_{\mathrm{obs}}}} - 1 \; . \tag{1.21}$$

Here the subscripts $_\star$ and $_{\mathrm{obs}}$ were used for quantities to be evaluated at the emitters and observers position, respectively.

The metric usually used to quantify this effect is the Schwarzschild metric, which describes the consistence of space-time around a spherically symmetric, non-rotating object. The line element is given by:

$$\mathrm{d}s^2 = -\,\mathrm{e}^{2\Phi}\,\mathrm{d}t^2 + \mathrm{e}^{-2\mu}\left[\mathrm{d}r^2 + r^2\left(\mathrm{d}\theta + \sin^2\theta\,\mathrm{d}\varphi^2\right)\right] \; , \tag{1.22}$$

with the constants Φ and μ reducing to the gravitational potential in the Newtonian limit (Misner et al., 1973, Chap. 23).

As this metric fulfills the requirements of the assumptions made above, the redshift is given by (1.21) and reads:

$$z = \mathrm{e}^{\Phi_\star - \Phi_{\mathrm{obs}}} - 1 \approx \Phi_\star - \Phi_{\mathrm{obs}} \; . \tag{1.23}$$

1.1.3 The Friedmann equations

Using the Friedmann-Lemaître-Robertson-Walker (FLRW) spacetime, which describes a homogeneous and isotropic universe, the line-element is given by

$$\mathrm{d}s^2 = g_{\mu\nu}\,\mathrm{d}x^\mu\,\mathrm{d}x^\nu = -\,\mathrm{d}t^2 + a^2(t)\left(\frac{\mathrm{d}r^2}{1-kr^2} + r^2\,\mathrm{d}\Omega^2\right) \tag{1.24}$$

with the curvature k, the expansion factor $a(t)$ and the differential solid angle $\mathrm{d}\Omega^2 = \mathrm{d}\theta^2 + \sin^2\theta\,\mathrm{d}\varphi^2$. The values 1, 0 and -1 for k correspond to an open, flat and closed universe respectively.

The energy-momentum tensor for a perfect fluid takes the form of Eq. (1.6). In comoving coordinates u^μ is simply (−1,0,0,0) and $g_{\mu\nu} = \eta_{\mu\nu} = \mathrm{diag}(-1,1,1,1)$. Consequently, in this case, the non-zero elements of the energy-momentum tensor are $T_{(00)} = -\rho$ and $T_{(ii)} = p$.

Inserting these two ingredients into Eq. (1.5) leads to

$$H^2 = \frac{8\pi G}{3}\rho - \frac{k}{a^2} \tag{1.25}$$

for the (00) component and

$$2\frac{\ddot{a}}{a} + H^2 = -8\pi G p + \frac{k}{a^2} \tag{1.26}$$

for the spacial components. The Hubble parameter is defined by

$$H \equiv \frac{\dot{a}}{a} \,. \tag{1.27}$$

Rewriting the two equations and using $w \equiv p/\rho$ one can obtain the second Friedmann equation (which can also be found directly using the trace of the Einstein equations):

$$\frac{\ddot{a}}{a} = -\frac{4}{3}\pi G\rho(3w+1) + \frac{k}{a^2} \tag{1.28}$$

and the continuity equation

$$\dot{\rho} + 3H\rho(1+w) = 0 \,. \tag{1.29}$$

The solution hereof is

$$\rho = \rho_0 \left(\frac{a_0}{a}\right)^{3(1+w)} \,. \tag{1.30}$$

Quantities with a subscript $_0$ denote the values today and the expansion factor is normalized to unity today.

Now these solutions can be rewritten in a more compact form with the help of some useful definitions. First, the critical density is

$$\rho_c = \frac{3H^2}{8\pi G} \,. \tag{1.31}$$

Using this relation, the relative density of the fluid components can be expressed as:

$$\Omega_i = \frac{\rho_i}{\rho_c} \,. \tag{1.32}$$

In a similar way the relative curvature is

$$\Omega_k = -\frac{k}{(aH)^2} \,. \tag{1.33}$$

Finally, the evolution of a universe filled with different matter i with relative densities today $\Omega_{i,0}$ and equation of state w_i is given as:

$$\frac{H^2}{H_0^2} = \sum_i \Omega_{i,0} a^{-3(1+w_i)} + \Omega_{k0} a^{-2} \,. \tag{1.34}$$

From this equation a general analytic solution for $a(t)$ cannot be found. Nevertheless, under the assumption of a unique fluid with equation of state w dominating in a flat universe ($\Omega_k = 0$), integration yields:

$$a(t) = \begin{cases} e^{H_0 t} & \text{if } w = -1 \\ \left(\frac{3}{2}(1+w)H_0 t\right)^{2/(3(1+w))} & \text{otherwise} \end{cases} \tag{1.35}$$

This means, a flat universe filled with radiation ($w_r = 1/3$) evolves as $a(t) \propto \sqrt{t}$ or ordinary matter ($w_m = 1$) as $a \propto t^{2/3}$.

See for instance Hartle (2003, Chap. 18) or Carroll (2004, Chap. 8) for a detailed description about the evolution of different universe models.

1.2 Dark energy

Supernovae observations (Perlmutter et al., 1999; Riess et al., 1998) showed that the expansion of the universe is accelerating. From the second Friedmann equation (1.28) it can be seen that such a behavior would be possible with a new component of the energy-momentum tensor with an effective equation of state $w < -1/3$. This could be new a form of matter that behaves totally differently to any known form of matter or it could be a modification of the field equations of general relativity.

What this component is, is absolutely unclear but it is called *dark energy* and the additional observational evidence about its existence is overwhelming (see for example Amendola & Tsujikawa (2010, Chap. 5)). Some of the evidence are:

- The age of the universe without dark energy is smaller than the age of globular clusters measured by Carretta et al. (2000) or Hansen et al. (2002).
- Measurements of the cosmic microwave background as done by the WMAP (Larson et al., 2011) or Planck (Planck Collaboration et al., 2013) project estimate the amount of dark energy of around 73% and restrain w very close to -1.
- Other phenomena such as Barionic Acoustic Oscillations and development of Large-Scale Structures.

The field of dark energy research is huge and various books and reviews have been published (e.g. Amendola & Tsujikawa (2010) and Clifton et al. (2012) which have mainly been used as reference for this section). This section tries to give a brief argument on how the analyzed models fit into the bigger picture of the dark energy sector. In order to do this, first the standard model – ΛCDM – is introduced, then the "Quintessence" part show how scalar field can play a role and at last scalar-tensor theories, $f(R)$-models and their possible equivalence are shown. For the last point a short intermezzo, where the concept of conformal frames is explained, was also added.

1.2.1 ΛCDM

The easiest model that accounts for these points is based on the introducing a new term $-2\sqrt{-g}\Lambda/16\pi G$ with the cosmological constant Λ into the action Eq. (1.7). The new field equations then reads:

$$R_{\mu\nu} - \frac{g_{\mu\nu}}{2}R + \Lambda g_{\mu\nu} = 8\pi G T_{\mu\nu} \; . \tag{1.36}$$

This model is called ΛCDM because of its main components: Dark energy (Λ) and cold dark matter (CDM).

To redefine the Einstein or the energy-momentum tensor in order to obtain the same form as in (1.5) is a matter of taste and interpretation: Is gravity itself modified or is another type of matter included in the universe? Although this is often just two sides of the same coin, it is very common to follow the latter path and assign the density $\rho_\Lambda = \Lambda/8\pi G$ and its

equation of state $w_\Lambda = p_\Lambda/\rho_\Lambda = -1$. Inserting these in Eq. (1.6) leaves the initial additional term of $-\Lambda g_{\mu\nu}$ as stated above.

An equation of state equal to minus one leads to interesting behavior of the fluid: As can be seen from the continuity equation Eq. (1.29), the density stays constant. This means dark energy gains more importance since the density of the other forms of matter decreases in an expanding space. Another fact is the exponential expansion, stated already in Eq. (1.35).

There are two major problems with the ΛCDM model: Firstly, although the density of matter ρ_m decreases with a^{-3} and the density of dark energy ρ_Λ stays constant, these two quantities are roughly the same just today. Because this happens only once in the whole history of the universe, it seems to be a very big coincidence this event happened just recently. Therefore, this problem is called "coincidence problem". The second famous problem with the cosmological constant is the so called "fine tuning problem": The observed value of Λ is around 120 orders of magnitude smaller than the vacuum energy found with a cut-off at the Planck scale. This discrepancy can be lowered to around 50 orders of magnitude with certain super-symmetric theories (Martin, 2012), but it is still too large to "fine tune" it away.

Other problems including missing satellite galaxies (Mateo, 1998) and non-matching of observed and simulated galaxy profiles (de Blok, 2010) are more related to CDM.

1.2.2 Quintessence

A hypothetical form of matter that could account for the dark energy phenomena is a simple scalar field. In an FLRW metric the pressure and density of a scalar field are given as usual by the time and space components of the energy-momentum tensor (Fujii & Maeda, 2007, Sec. 5.2):

$$\begin{aligned} p_\phi &= T^{(\phi)}_{ii} = \frac{1}{2}\dot{\phi}^2 - V(\phi) \\ \rho_\phi &= -T^{(\phi)}_{00} = \frac{1}{2}\phi^2 + V(\phi)\ . \end{aligned} \tag{1.37}$$

Consequently, the equation of state is

$$w_\phi = \frac{p_\phi}{\rho_\phi} = \frac{\frac{1}{2}\dot{\phi}^2 - V(\phi)}{\frac{1}{2}\dot{\phi}^2 + V(\phi)}\ . \tag{1.38}$$

This makes a scalar field a dark energy candidate because if $\dot{\phi}^2/2 \ll V(\phi)$ ("slowly rolling") the matter of state is $w_\phi \approx -1$. However, in opposition to the equation of state of a cosmological constant w_ϕ is changing in time.

In order to study the behavior of the quintessence model, the same steps as for the ΛCDM model can be done: Vary the action and demand that this variation is zero. So let's start

with the action, which has an extra term for the scalar field ϕ and is given(Fujii & Maeda, 2007) by

$$S_\phi = -\int \mathrm{d}^4x\,\sqrt{-g}\left\{\frac{1}{2}\partial_\mu\phi\partial^\mu\phi + V(\phi)\right\} \tag{1.39}$$

with the potential $V(\phi)$. Variation of the action with respect to ϕ results in the Klein-Gordon equation

$$\Box\phi - V'(\phi) = 0\ . \tag{1.40}$$

This can be derived using $\delta S_\phi = S_\phi(\phi+\delta\phi) - S_\phi(\phi)$. Assuming the variation $\delta\phi$ vanishes at the boundary, the first term becomes then $-\int \mathrm{d}^4x\,\sqrt{-g}\partial_\mu\phi\partial^\mu\delta\phi$. After partial integration we obtain the form above. For the full derivation see Appendix A.1

Assuming a homogeneous scalar field and a surrounding FLRW metric the equation turns into:

$$\ddot{\phi} + 3H\dot{\phi} + V' = 0\ . \tag{1.41}$$

In quintessence models, a wide range of initial conditions may converge quickly to the same cosmological evolution, so called "tracker solutions" (Steinhardt et al., 1999). As these tracker solutions may solve partly the coincidence problem, they still need fine tuning (e.g. of the potential) in order to explain why the accelerated expansion happens today (Armendariz-Picon et al., 2000).

1.2.3 Einstein and Jordan frame

In modified gravity models the Einstein-Hilbert action Eq. (1.7) is usually modified. Nevertheless, because general relativity can explain a large number of observations, the modified actions are often constructed in a way that the Einstein-Hilbert action can be recovered in some limit.

Name	Equation
Metric	$g_{\mu\nu} = \mathcal{C}\tilde{g}_{\mu\nu}$
Determinant	$g = \mathcal{C}^4\tilde{g}$
Christoffel Symbol	$\Gamma^\alpha_{\mu\nu} = \tilde{\Gamma}^\alpha_{\mu\nu} + \mathcal{C}^{-1}\left(\delta^\alpha_\nu\tilde{\nabla}_\mu\mathcal{C} + \delta^\alpha_\mu\tilde{\nabla}_\nu\mathcal{C} - \tilde{g}_{\mu\nu}\tilde{\nabla}^\alpha\mathcal{C}\right)/2$
Ricci Tensor	$R_{\mu\nu} = \tilde{R}_{\mu\nu} + \mathcal{C}^{-2}\left(3\tilde{\nabla}_\mu\mathcal{C}\tilde{\nabla}_\nu\mathcal{C} - \mathcal{C}\tilde{g}_{\mu\nu}\tilde{\Box}\mathcal{C} - 2\mathcal{C}\tilde{\nabla}_\mu\tilde{\nabla}_\nu\mathcal{C}\right)/2$
Ricci Scalar	$R = \tilde{R}/\mathcal{C} + 3\mathcal{C}^{-3}\left(\tilde{\nabla}_\alpha\mathcal{C}\tilde{\nabla}^\alpha\mathcal{C} - 2\mathcal{C}\tilde{\Box}\mathcal{C}\right)/2$
D'Alembert Operator	$\Box\phi = \mathcal{C}^{-2}\left(\tilde{\nabla}_\alpha\phi\tilde{\nabla}^\alpha\mathcal{C} + \mathcal{C}\tilde{\Box}\phi\right)$

Table 1.1: Table of some important quantities expressed in terms of the metric $g_{\mu\nu}$ under the conformal transformation $g_{\mu\nu} \to \tilde{g}_{\mu\nu}$ as defined in equation (1.42).

It is possible to conformally transform the metric (meaning scales are altered, but angles are unchanged) and state the theory in a different "frame". Mathematically, this transformation can be stated as:

$$g_{\mu\nu} = \mathcal{C}(x)\tilde{g}_{\mu\nu} \tag{1.42}$$

with $\mathcal{C}(x)$ being a positive function of the spacetime coordinate x^μ. The line elements of the two frames are therefore related by $\mathrm{d}s^2 = \mathcal{C}(x)\,\mathrm{d}\tilde{s}^2$. Physically, this change is possible because causality is linked to angles in spacetime, i.e. the metrics $\tilde{g}_{\mu\nu}$ and $g_{\mu\nu}$ contain the same causal structure, although the norm of the vectors can be changed.

The relations occurring between some quantities of the conformally related frames will be important later on and are therefore summarized in the table 1.1.

As $\mathcal{C}(x)$ is an arbitrary positive function, the theory can be stated in an infinite number of frames. Two of these frames are very important and frequently used: The Einstein and the Jordan frame.

In the Jordan frame the energy-momentum tensor is covariantly conserved ($T^{\mu\nu}_{\ ;\nu} = 0$) and massless test particles follow the geodesic equation in this metric (Clifton et al., 2012).

In the Einstein frame the action takes the same form as the original Einstein-Hilbert action (linear in the Ricci scalar) with the addition of some extra matter fields that arouse in the transformation.

Which of the frames is the "physical" one is subject of discussion (see e.g. Faraoni et al. (1998)).

From now on, because the two frames will be used frequently, the function $\mathcal{C}(x)$ will be used to describe the transformation between them and not as a general transformation function.

1.2.4 Scalar-tensor theories

Probably one of the best studied modifications of General relativity fall under the group of scalar-tensor theories, amongst which the most prominent is the Brans-Dicke theory (Brans & Dicke, 1961). Scalar-tensor theories can be understood as a generalization of the quintessence model described before. Instead of having a completely free scalar field, a coupling to matter of order unity is introduced. This stronger coupling is on the one hand much more natural (Carroll, 1998) but on the other hand it gives rise to a fifth force which would be observationally detectable.

In the Einstein frame, the action for scalar-tensor theories is given (Clifton et al., 2012) by

$$S = \int \mathrm{d}^4x\,\sqrt{-\tilde{g}}\left\{\frac{\tilde{R}}{2\kappa} - \frac{1}{2}\tilde{\nabla}_\mu\phi\tilde{\nabla}^\mu\phi - V(\phi)\right\} + S_m(g_{\mu\nu},\Psi_m)\ . \tag{1.43}$$

Here, the additional scalar field component S_ϕ as used in Eq. (1.39) is added to the Einstein-Hilbert action as an additional component. Keep in mind that particles (here represented

by a matter field Ψ_m) will follow geodesics of their Jordan frame metric $g_{\mu\nu}$.[1] Therefore, in the Einstein frame particles feel an additional "fifth" force.

Variation of this action with respect to the metric $\tilde{g}_{\mu\nu}$ leads to

$$\tilde{G}_{\mu\nu} = \kappa\left(\tilde{T}_{\mu\nu} + \tilde{\nabla}_\mu\phi\tilde{\nabla}_\nu\phi\right) - \kappa\tilde{g}_{\mu\nu}\left(\frac{1}{2}\nabla_\alpha\phi\nabla^\alpha\phi + V(\phi)\right) . \tag{1.44}$$

Since ϕ is a second degree of freedom, the action can also be varied with respect to ϕ which results in the equation of motion of the scalar field

$$\tilde{\Box}\phi - V'(\phi) = V'_+(T,\mathcal{C}) . \tag{1.45}$$

The right hand side depends on the trace of the energy-momentum tensor $T = T_{\mu\nu}g^{\mu\nu}$, which was defined in Eq. (1.17) and the definition of the function $\mathcal{C}$, which links the Einstein and the Jordan frame. In later sections, the function $\mathcal{C}$ is fixed and the behavior of the scalar field will be studied. What we can notice already now comparing this result with the equation of motion obtained for the quintessence model (see Eq. (1.40)), is that ϕ behaves like a free scalar field in an effective potential $V_{eff} = V_+ + V$.

1.2.5 $f(R)$-gravity

In the $f(R)$ gravity the Ricci scalar R in the Einstein-Hilbert action (1.7) is replaced by a general function $f(R)$ and the new action reads:

$$S = \frac{1}{2\kappa}\int \mathrm{d}^4x\,\sqrt{-g}f(R) . \tag{1.46}$$

The motivation behind this approach is to assume that $f(R) = R$ is valid for small ranges where a higher order is to be used for larger scales. Unfortunately while a simple model like $f(R) = R+\alpha R^2$ can be responsible for inflation, it can not explain the late time acceleration (Amendola & Tsujikawa, 2010, Chap. 9).

In addition to the late time acceleration, the model has to fulfill also local gravity constraints. Therefore, only more complex models are not ruled out. Three examples are:

- The model of Hu & Sawicki (2007) given by

$$f(R) = R - \frac{\mu R_c}{1 + (R/R_c)^{-2n}} \tag{1.47}$$

- Starobinsky (2007) come up with

$$f(R) = R - \mu R_c\left[1 - \left(1 + \frac{R^2}{R_c^2}\right)^{-n}\right] \tag{1.48}$$

1 The assumption was made that the scalar field couples to all the matter types with the same strength. Otherwise there would be several Jordan-frame metrics $g^{(i)}_{\mu\nu}$.

- And the approach from Appleby & Battye (2007):

$$f(R) = R + R_c \log\left(\mathrm{e}^{-\mu} + (1 - \mathrm{e}^{-\mu})\,\mathrm{e}^{-R/R_c}\right) \tag{1.49}$$

In all examples n, μ and R_c are positive constants.

Without specifying the shape of $f(R)$ further, one can carry out the variation of the action (1.46) as done before for the Einstein-Hilbert action:

$$\delta S = \frac{1}{2\kappa}\int \mathrm{d}^4x\,\sqrt{-g}\left\{-\frac{1}{2}f(R)g^{\mu\nu}\delta g_{\mu\nu} + f_R\left(R_{\mu\nu}\delta g^{\mu\nu} + g^{\mu\nu}\delta R_{\mu\nu}\right)\right\} + \delta S_m \tag{1.50}$$

where the commonly used definition $f_R \equiv \partial f/\partial R$ has been applied. Note that in this case, the last term inside the parenthesis does not vanish as the multiplication with f_R may lead to nonzero boundary terms. Therefore, the full variation of $R_{\mu\nu}$ has to be analyzed. Recall that

$$\delta R = R_{\mu\nu}\delta g^{\mu\nu} + g^{\mu\nu}\left(\delta\Gamma^{\alpha}_{\mu\nu;\alpha} - \delta\Gamma^{\alpha}_{\alpha\mu;\nu}\right) \tag{1.51}$$

as stated in Eq. (1.13). Varying the Christoffel symbols defined in Eq. (1.1) results in

$$\delta\Gamma^{\alpha}_{\mu\nu} = \frac{g^{\alpha\sigma}}{2}\left(\delta g_{\mu\sigma;\nu} + \delta g_{\nu\sigma;\mu} - \delta g_{\mu\nu;\sigma}\right)\ . \tag{1.52}$$

This can be derived by using the fact that $\delta g_{\mu\nu,\alpha} = \delta g_{\mu\nu;\alpha} + \Gamma^{\sigma}_{\nu\alpha}\delta g_{\mu\sigma} + \Gamma^{\sigma}_{\mu\alpha}\delta g_{\nu\sigma}$ and the non-tensorial terms (i.e. the ones including a connection symbol) have to cancel because as stated before $\delta\Gamma^{\alpha}_{\mu\nu}$ is a tensor.

Rewriting Eq. (1.51) using Eq. (1.52) leads to:

$$\begin{aligned}\delta R =& R_{\mu\nu}\delta g^{\mu\nu} + \nabla^{\mu}\nabla^{\nu}\delta g_{\mu\nu} - g^{\mu\nu}\Box\delta g_{\mu\nu}\\ =& R_{\mu\nu}\delta g^{\mu\nu} - \nabla_{\mu}\nabla_{\nu}\delta g^{\mu\nu} - g_{\mu\nu}\Box\delta g^{\mu\nu}\ .\end{aligned} \tag{1.53}$$

Now, the total variation of the action can be written as

$$\begin{aligned}\delta S = \int \mathrm{d}^4x\,\frac{\sqrt{-g}}{2\kappa}\Big\{ &-\frac{f}{2}g_{\mu\nu}\delta g^{\mu\nu}\\ &+ f_R\left(R_{\mu\nu}\delta g^{\mu\nu} - \nabla^{\mu}\nabla^{\nu}\delta g_{\mu\nu} + g_{\mu\nu}\Box\delta g^{\mu\nu}\right)\Big\} + \delta S_m\end{aligned} \tag{1.54}$$

$$= \int \mathrm{d}^4x\,\frac{\sqrt{-g}}{2\kappa}\delta g^{\mu\nu}\left\{-\frac{f}{2}g_{\mu\nu} + f_R R_{\mu\nu} - \nabla_{\mu}\nabla_{\nu}f_R + g_{\mu\nu}\Box f_R\right\} + \delta S_m\ , \tag{1.55}$$

where in the last equality integration by parts (with the assumption that the boundary terms are negligible) has been performed twice. Furthermore, as done before, by demanding $\delta S = 0$ and using the definition of the energy-momentum tensor (1.16) we obtain:

$$f_R R_{\mu\nu} - \frac{f}{2}g_{\mu\nu} - \nabla_{\mu}\nabla_{\nu}f + g_{\mu\nu}\Box f_R = \kappa T_{\mu\nu} \tag{1.56}$$

1.2.6 $f(R)$-gravity as a scalar-tensor theory

In the previous sections it was presented that the framework of a scalar-tensor theory is very convenient to find viable models that help solving the known ΛCDM problems. On the other hand, the $f(R)$ framework can be a very natural extension to general relativity. In this section, it is shown that the two frameworks are under just two sides of the same coin, i.e. that under certain conditions an $f(R)$ theory can be rephrased as a scalar-tensor theory and the other way around.

In order to show the possible equivalence between the $f(R)$-models and scalar-tensor theories, we start with the "arbitrary" action

$$S = \int \mathrm{d}^4x \, \frac{\sqrt{-g}}{2\kappa} \left\{ f(\chi) + f'(\chi) \left[R - \chi \right] \right\} \ , \tag{1.57}$$

where χ is a new field that depends on x^μ just as R.

Variation with respect to χ yields

$$\frac{\delta S}{\delta \chi} = \frac{1}{2\kappa} \int \mathrm{d}^4x \, \sqrt{-g} f''(\chi) \left[R - \chi \right] \ . \tag{1.58}$$

This means that $\chi = R$ given $f''(\chi) \neq 0$. Plugging this result back into the starting equation (1.57), we obtain

$$S = \frac{1}{2\kappa} \int \mathrm{d}^4x \, \sqrt{-g} f(R) \ , \tag{1.59}$$

which is the same as the action of the $f(R)$-gravity Eq. (1.46). Consequently, if the action (1.57) can be brought to the same form as Eq. (1.43), the equality between the theories has been proven.

Starting point is the transformation of this action to the Einstein frame. Using the general transformation rules summarized in table 1.1, the equation can be written as

$$S = \int \mathrm{d}^4x \, \sqrt{-\tilde{g}} \mathcal{C}^2 \left\{ f + f' \left(\frac{\tilde{R}}{\mathcal{C}} + \frac{3 \tilde{\nabla}_\alpha \mathcal{C} \tilde{\nabla}^\alpha \mathcal{C} - 6 \mathcal{C} \tilde{\Box} \mathcal{C}}{2 \mathcal{C}^3} - \chi \right) \right\} \ . \tag{1.60}$$

Here and for the rest of this section, units such that $\kappa = 1$ have been chosen. From this intermediate result we can see in order to obtain a linear term in $\tilde{R}$, the relation $\mathcal{C} = 1/f'$ has to hold.

With the transformation function $\mathcal{C}$ specified, we obtain after some rearranging:

$$S = \int \mathrm{d}^4x \, \sqrt{-\tilde{g}} \left\{ \frac{\tilde{R}}{2} + \frac{f - f'\chi}{2f'^2} - \left(\frac{3}{2f'} \right)^2 \tilde{\nabla}_\alpha f' \tilde{\nabla}^\alpha f' + \frac{3}{2f'} \tilde{\Box} f' \right\} \tag{1.61}$$

Now, we can introduce the scalar field ϕ and identify the second term of the integrand with its potential V:

$$f'(\chi) \equiv \mathrm{e}^{2\beta\phi/M_{\mathrm{Pl}}} \ , \qquad V = -\frac{f - f'\chi}{2f'^2} \ . \tag{1.62}$$

Here, β is the dimensionless coupling constant. The factor 2 in the exponent is introduced in accordance with the literature. An assumption to be made at this point is that ϕ vanishes at the boundary, so the total divergence terms ($\int \mathrm{d}^4x\,\sqrt{-g}\Box\phi$) disappear, which leaves

$$S = \int \mathrm{d}^4x\,\sqrt{-\tilde{g}}\left\{\frac{\tilde{R}}{2} - 3\beta^2\tilde{\nabla}_\alpha\phi\tilde{\nabla}^\alpha\phi - V\right\}\,. \tag{1.63}$$

Comparing this result with the canonical form of (1.43), it is clear that $\beta = 1/\sqrt{6}$. If the coupling parameter takes a different value in a scalar-tensor theory, this theory cannot be formulated as an $f(R)$-model.

To summarize the results of this section: An $f(R)$ model can be treated as a scalar-tensor theory, with the scalar field appearing through the conformal transformation of the metric given by

$$g_{\mu\nu} = \mathrm{e}^{2\beta\phi/M_{\mathrm{Pl}}}\,\tilde{g}_{\mu\nu} \quad \text{with } \beta = \frac{1}{\sqrt{6}}\,. \tag{1.64}$$

The potential of this scalar field is given by (1.62), which can be rewritten as $\chi = R$ resulting in

$$V = -\frac{f - f_R R}{2f_R^2}\,. \tag{1.65}$$

Here the notation introduced in the section about $f(R)$ models, 1.2.5, namely $f_R \equiv \mathrm{d}f/\mathrm{d}R$ has been restored.

2

Review of the Chameleon and Symmetron Models

As the matter proportion in the universe is similar to the one of dark energy, there might be some relation between those. This motivation supports "coupled dark energy" models like the Brans-Dicke theory (Brans & Dicke, 1961) or Dilaton (Brax et al., 2010a).

A simple coupled dark energy model is the "coupled quintessence" model, in which a scalar field is coupled to matter with the coupling strength β. This can potentially solve the coincidence problem, as the energy ratio of the two components dark energy and dark matter was constant or similar throughout the whole history of the universe and did not change dramatically in the recent past (Wetterich, 1995).

However, as shown in section 1.2.4, there is an additional force acting on the particles in scalar-tensor theories. If the coupling constant is around unity, this fifth force should have been detected.

A possible solution to this problem are so called "screening mechanisms" that lead to a suppression of this additional force in the solar system and therefore avoiding detection through local experiments.

In this chapter the two screening mechanisms that this work is related to are reviewed: The chameleon and the Symmetron models. In both models the screening is environment dependent but works through different mechanisms:

- The **chameleon Mechanism** (Brax et al., 2004; Khoury & Weltman, 2004a,b) the effective mass of the field depends on the local matter density in such a way that in outer space the field is very light and a fifth force is mediated. If the matter density is high, the field becomes heavy and the fifth force is suppressed. The chameleon model is reviewed in section 2.1 and the connection to $f(R)$ theory is made in section 2.3.
- In the **Symmetron Model** (Hinterbichler & Khoury, 2010; Hinterbichler et al., 2011; Olive & Pospelov, 2008) the vacuum-expectation value (VEV) of the scalar field depends on the local matter density. In high density regions the VEV is close to zero but when the matter density is lower, the symmetry of the potential is broken and the

VEV is higher, leading to an additional force in these regions. The symmetron model in its implications are discussed in section 2.2.

2.1 Introduction to the chameleon mechanism

In the following a short introduction to the chameleon theory is given. Better, more in-depth reviews, which were also used as reference are for example Khoury & Weltman (2004a) and Waterhouse (2006).

The equation to start is the general action of a scalar-tensor theory in the Einstein frame describing a scalar field ϕ with potential $V(\phi)$ as stated already in (1.43):

$$S = \int \mathrm{d}^4x \sqrt{-g} \left\{ \frac{R}{2\kappa} - \frac{1}{2}\nabla_\mu\phi\nabla^\mu\phi - V(\phi) \right\} + S_m(g^{(i)}_{\mu\nu}, \Psi_m) \ . \tag{2.1}$$

Here, each of the matter fields couples to its Jordan frame metric $g^{(i)}_{\mu\nu}$ which is linked to the Einstein frame metric via[1]

$$g^{(i)}_{\mu\nu} \equiv \mathrm{e}^{2\beta_i\phi/M_{\mathrm{Pl}}}\, g_{\mu\nu} \tag{2.2}$$

with the dimensionless coupling constants β_i. This conformal transformation is of the same kind as the one obtained in the previous section 1.2.6 where the equivalence of the $f(R)$-model and the Scalar-tensor theories was shown. However, leaving the coupling β_i free means that the chameleon mechanism chapter cannot necessarily be described in the framework of the $f(R)$-models. This is only the case if $\beta_i = 1/\sqrt{6}$ for all β_i.

After variation of Eq. (2.1) we obtain

$$\Box\phi - V_{,\phi}(\phi) - \sum_i \frac{1}{\sqrt{-g}} \frac{\partial \mathcal{L}}{\partial g^{(i)}_{\mu\nu}} \frac{2\beta_i}{M_{pl}} g^{(i)}_{\mu\nu} = 0 \ . \tag{2.3}$$

This equation is similar to the equation of motion for the scalar field Eq. (1.45) with the exception that we can specify the effective potential more precisely. Here the action of matter fields $\psi^{(i)}_m$ has been expressed with the Lagrangian density:

$$S_m = -\int \mathrm{d}^4x\, \mathcal{L}\left(\psi^{(i)}_m, g^{(i)}_{\mu\nu}\right) \ . \tag{2.4}$$

Using the energy-momentum tensor for the ith matter component

$$T^{(i)}_{\mu\nu} = \frac{2}{\sqrt{g_{(i)}}} \frac{\partial \mathcal{L}}{\partial g^{\mu\nu}_{(i)}} \tag{2.5}$$

1 In order to be in consistence with the literature, the quantities in the *Einstein frame* will be without and the ones describing the *Jordan frame* with an embraced indice or a tilde. As this is just the opposite as used in the previous chapter, hopefully nothing is too confusing.

and the assumption that the matter is a perfect fluid $g^{(i)}_{\mu\nu}T^{\mu\nu}_i = -\rho_{(i)} + 3p_{(i)} = -(1-3w_i)\rho_{(i)}$ one can rewrite the equation of motion to

$$\Box\phi - V_{,\phi}(\phi) + \sum_i \frac{2\beta_i}{M_{\rm Pl}} \mathrm{e}^{4\beta_i\phi/M_{\rm Pl}}(1-3w_i)\tilde{\rho}^{(i)} = 0 \,, \tag{2.6}$$

where the exponential term arises from the fact that $g = \det(\mathbf{g}) = \exp(-8\beta_i\phi/M_{\rm Pl})\det(\mathbf{g^{(i)}})$. Please note that for radiation ($w = 1/3$), the equation of motion is not dependent on the surrounding density. In Section 2.4 we will see that for this case no fifth force arises.

It would be very convenient to express the equation of motion in terms of some energy density instead of the rather abstract energy-momentum tensor. Therefore, we look for a quantity $\rho^{(i)}$ obeying the continuity equation $\rho^{(i)} \propto a^{-3(1+w_i)}$ in the Einstein frame. Starting from the conservation of the energy-momentum tensor in the Jordan frame $\tilde{\nabla}_\nu \tilde{T}^{\mu\nu} = 0$ (Fujii & Maeda, 2007), with the covariant derivative $\tilde{\nabla}_\mu$ corresponding to the metric $\tilde{g}_{\mu\nu}$, one finds this quantity is

$$\rho^{(i)} = \mathrm{e}^{3(1+w_i)\beta_i/M_{\rm Pl}}\,\tilde{\rho}^{(i)} \,. \tag{2.7}$$

This simplifies the equation of motion to

$$\Box\phi - V_{,\phi}(\phi) - \sum_i (1-3w_i)\frac{\beta_i}{M_{\rm Pl}}\rho^{(i)}\,\mathrm{e}^{(1-3w_i)\beta_i\phi/M_{\rm Pl}} = 0 \,. \tag{2.8}$$

Introducing an effective potential so that $\Box\phi = V_{\rm eff,\phi}(\phi)$ results in

$$V_{\rm eff}(\phi) = V(\phi) + \sum_i \rho^{(i)}\,\mathrm{e}^{(1-3w_i)\beta_i\phi/M_{\rm Pl}} \,. \tag{2.9}$$

The shape of the potential $V(\phi)$ has to be in a way that ϕ acts as a cosmological constant, i.e. ϕ has to slowly roll down the potential (see section 1.2.2 for an introduction of the slow-roll mechanism). In order to solve the coincidence problem the scalar field should not have began to start rolling recently, but instead should be always rolling down the potential. Therefore, $V(\phi)$ should be monotonically decreasing. Furthermore, the following should be fulfilled for all $i \in \mathbb{N}$ (Khoury & Weltman, 2004a):

$$\lim_{\phi\to\infty} V(\phi) = 0, \quad \lim_{\phi\to\infty} \frac{\partial^{(i)}V}{\partial\phi^{(i)}} \Big/ \frac{\partial^{(i-1)}V}{\partial\phi^{(i-1)}} = 0 \quad \text{and} \quad \lim_{\phi\to 0} \frac{\partial^{(i)}V}{\partial\phi^{(i)}} \Big/ \frac{\partial^{(i-1)}V}{\partial\phi^{(i-1)}} = \infty \tag{2.10}$$

Common choices for the potential are, e.g. the inverse power-law potential

$$V(\phi) = \frac{M^{4+n}}{\phi^n} \tag{2.11}$$

or the exponential potential given by

$$V(\phi) = M^4\,\mathrm{e}^{M^n/\phi^n} \,. \tag{2.12}$$

In both cases M and n are positive constants and M has the units of mass.

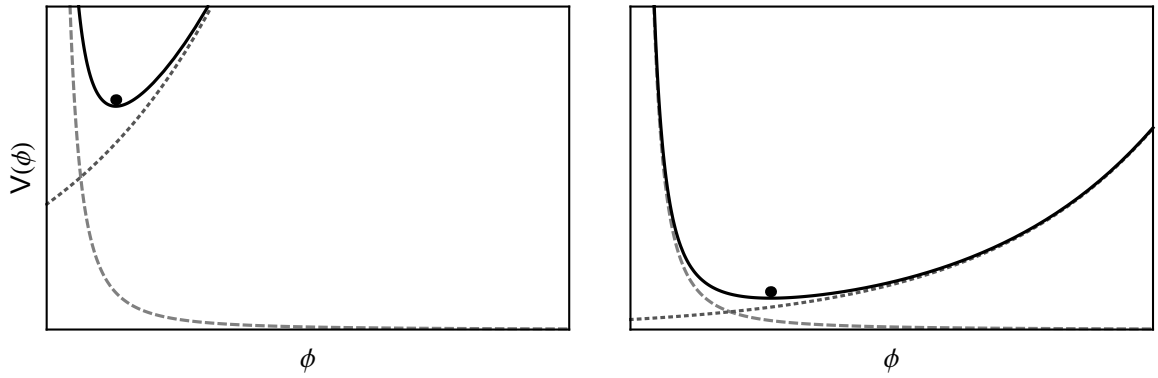

Figure 2.1: chameleon mechanism at work: The solid, dashed and dotted lines show respectively the effective potential V_{eff}, the bare potential V and the density dependent component. The black dot illustrates the minimum of the effective potential. On the *left* side the situation is shown in a high-density region: The effective minimum is very close to $\phi = 0$ and the fifth force is screened. In the *right* graph the field is in a lower density region. ϕ can be at much higher values and therefore a non-neglectable fifth force may be present.

As shown in Fig. 2.1 the effective potential $V_{\rm eff}$ can have a minimum in a region where the matter density ρ_i is not zero and if $V(\phi)$ and β_i have the same sign. The value where the scalar field settles $\phi_{\rm min}$ is therefore given by

$$V_{,\phi}(\phi_{\rm min}) + \sum_i (1-3w_i)\frac{\beta_i}{M_{\rm Pl}}\rho_i \, \mathrm{e}^{(1-3w_i)\beta_i\phi_{\rm min}/M_{\rm Pl}} = 0 \tag{2.13}$$

and the mass of the field is defined as

$$m^2_{\rm min} \equiv V_{{\rm eff},\phi\phi}(\phi_{\rm min}) = V_{,\phi\phi}(\phi_{\rm min}) + \sum_i (1-3w_i)^2 \frac{\beta_i^2}{M_{\rm Pl}^2}\rho_i \, \mathrm{e}^{(1-3w_i)\beta_i\phi_{\rm min}/M_{\rm Pl}} \ . \tag{2.14}$$

This term is important as the mass is the inverse of the characteristic range of the fifth force (Khoury & Weltman, 2004a).

2.1.1 The chameleon in outer space

Using the standard FLRW metric introduced in section 1.1.3 and assuming spatial homogeneity of the scalar field ($\partial_i \phi^i = 0$) the first term of the equation of motion (2.8) turns into

$$\Box\phi = g^{\mu\nu}\nabla_\mu\nabla_\nu\phi \tag{2.15}$$

$$= g^{00}\partial_0\partial_0\phi - g^{ii}\Gamma^0_{ii}\phi_{,0} \tag{2.16}$$

$$= -\ddot{\phi} - 3H\dot{\phi} \ . \tag{2.17}$$

Consequently, we obtain the usual solution for a homogeneous scalar field in the potential $V_{\rm eff}$:

$$\ddot{\phi} + 3H\dot{\phi} = -V_{{\rm eff},\phi}(\phi) \tag{2.18}$$

2.1.2 The chameleon close to masses

In the following only one pressureless particle species is considered that couples to the metric $\tilde{g}_{\mu\nu}$ with coupling parameter β. That is i is fixed and w_i is taken to be zero.

The motion of a particle in the Jordan frame is given by the geodesics of the transformed metric:

$$\ddot{x}^\alpha + \tilde{\Gamma}^\alpha_{\mu\nu}\dot{x}^\mu\dot{x}^\nu = 0 \tag{2.19}$$

Here $\tilde{\Gamma}^\alpha_{\mu\nu}$ are the Christoffel symbols of the metric $\tilde{g}_{\mu\nu}$. Calculating the Christoffel symbols as in section 1.1 leads to

$$\ddot{x}^\alpha + \Gamma^\alpha_{\mu\nu}\dot{x}^\mu\dot{x}^\nu + \frac{\beta}{M_{\mathrm{Pl}}}\left(2\phi_{,\mu}\dot{x}^\mu\dot{x}^\alpha + g^{\alpha\sigma}\phi_{,\sigma}\right) = 0\ . \tag{2.20}$$

Taking now the non-relativistic limit ($\dot{x}^\mu \ll c$, $g_{\mu\nu} \approx \eta_{\mu\nu}$) and assuming a static field ($\phi_{,0} = 0$) we obtain:

$$\ddot{\mathbf{x}} = -\frac{\beta}{M_{\mathrm{Pl}}}\vec{\nabla}\phi \tag{2.21}$$

This shows that ϕ can be interpreted as the potential giving rise to the chameleon force.

Commonly (as in Khoury & Weltman (2004a)) the variation of the fifth force close to a spherical body with radius R_c and density ρ_c embedded in a medium with density ρ_∞ is discussed. The solution is sketched here in brief so that the qualitative behavior of the fifth force is clear. For a full derivation see Khoury & Weltman (2004a) or Waterhouse (2006).

The equation to solve is the equation of motion of the field (2.8). Expressed in polar coordinates including the assumptions that $g_{\mu\nu} \approx \eta_{\mu\nu}$ and the non relativistic matter introduced above this reads

$$\frac{\mathrm{d}^2\phi}{\mathrm{d}r^2} + \frac{2}{r}\frac{\mathrm{d}\phi}{\mathrm{d}r} = V_{,\phi} + \frac{\beta}{M_{\mathrm{Pl}}}\rho(r)\,\mathrm{e}^{\beta\phi/M_{\mathrm{Pl}}} \tag{2.22}$$

with the density given as

$$\rho(r) = \begin{cases}\rho_c & \text{if } r < R_c \\ \rho_\infty & \text{if } r > R_c\ .\end{cases} \tag{2.23}$$

In both regions the effective potential V_{eff} has a minimum whose positions are given by ϕ_c and ϕ_∞, respectively. The mass of the field at both positions will be denoted as m_c and m_∞.

In order to solve this equation the following boundary conditions are used

$$\frac{\mathrm{d}\phi}{\mathrm{d}r} = 0 \text{ at } r = 0 \tag{2.24}$$

$$\phi \to \phi_\infty \text{ as } r \to \infty\ . \tag{2.25}$$

Both make sense from a physical perspective: Firstly,a singularity at the origin is unphysical and secondly the fifth force should vanish very far away from the object.

In the literature two analytical solutions are usually given: One called the "thin-shell" or "screened" solution is an approximation for relatively large objects. Here, the potential takes the value ϕ_c for regions that are ΔR_C below the surface of the sphere. In this "core" region the chameleon is fully screened and there is not only no fifth force within this area but the contribution of volume elements lying within this region is negligible for the ϕ value outside the sphere. Far away from the object the value $\phi \approx \phi_\infty$ is fixed. Consequently, the solution outside the body is an interpolation between ϕ_c and ϕ_∞:

$$\phi^{(s)}(r) \approx -\frac{3\beta}{4\pi M_{\mathrm{Pl}}} \frac{\Delta R_c}{R_c} \frac{M_c \, \mathrm{e}^{-m_\infty r}}{r} + \phi_\infty \tag{2.26}$$

with r being the distance from the center of the sphere, M_c the mass of the sphere and the thickness of the shell being defined via

$$\frac{\Delta R_c}{R_c} = \frac{|\phi_\infty - \phi_c|}{6\beta M_{\mathrm{Pl}} \Phi_c} \tag{2.27}$$

where $\Phi_c = M_c/(8\pi M_{\mathrm{Pl}}^2 R_c)$ denotes the Newtonian potential of the object. In order that this approximation can be used, this ratio has to be much smaller than one: $\Delta R_c/R_c \ll 1$.

In the other approximation, not surprisingly referred to as "thick-shell" and "unscreened", the object is smaller and $\Delta R_c/R_c > 1$. Here the whole body contributes to the ϕ-field outside the object and not just the "shell" as before. The exterior solution is then given by

$$\phi^{(u)}(r) \approx -\frac{\beta}{4\pi M_{\mathrm{Pl}}} \frac{M_c \, \mathrm{e}^{-m_\infty r}}{r} + \phi_\infty \, . \tag{2.28}$$

The strength of the fifth force in these two cases can be approximated using Eq. (2.21). With the reasonable assumption that m_∞ is small, the additional acceleration for the thin shell – that is the screened – solution is

$$\ddot{\mathbf{x}}^{(s)}_{\mathrm{Fifth}} \approx -\frac{6GM_c\beta^2\beta^2}{r^2} \frac{\Delta R_c}{R_c} \hat{\mathbf{e}}_r = 6\beta^2 \frac{\Delta R_c}{R_c} \ddot{\mathbf{x}}_{\mathbf{N}} \tag{2.29}$$

with $\ddot{\mathbf{x}}_N = -GM_c/r^2 \hat{\mathbf{e}}_r$ being the acceleration due to the Newtonian force.

For the thick shell, i.e. the unscreened solution, the result obtained is

$$\ddot{\mathbf{x}}^{(u)}_{\mathrm{Fifth}} \approx -\frac{2GM_c\beta^2}{r^2} \hat{\mathbf{e}}_{\mathbf{r}} = 2\beta^2 \ddot{\mathbf{x}}_{\mathbf{N}} \, . \tag{2.30}$$

This means, the maximum enhancement of the gravitational force is $2\beta^2$ which is equal to $1/3$ for $f(R)$-models as shown in Section 1.2.6.

The results derived here will be used when studying spherical collapse in screened modified gravity models in Section 4.2.

2.2 The symmetron model

The symmetron was presented in Hinterbichler & Khoury (2010) and Hinterbichler et al. (2011), articles which outline this section will follow.

As in the chameleon theory presented in the previous section, the action in the Einstein frame is given by $S = S_{EH} + S_\phi + S_{\text{matter}}$:

$$S = \int \mathrm{d}^4x \left\{ \sqrt{-g} \left(\frac{M_{\text{Pl}}^2}{2} R - \frac{1}{2} \nabla_\mu \phi \nabla^\mu \phi - V(\phi) \right) + \sqrt{-\tilde{g}} \mathcal{L}_m(\psi^{(i)}, \tilde{g}_{\mu\nu} \right\} \tag{2.31}$$

where the matter fields $\psi^{(i)}$ couple to the Jordan frame metric given by[1]

$$\tilde{g}_{\mu\nu} \equiv A^2(\phi) g_{\mu\nu} \, . \tag{2.32}$$

This leads to a equation of motion for the scalar field given by

$$\Box\phi - V_{,\phi} + A^3(\phi) A_{,\phi}(\phi) \tilde{T} = 0 \tag{2.33}$$

with the trace of the energy-momentum tensor is

$$\tilde{T} = \tilde{g}^{\mu\nu} \tilde{T}_{\mu\nu} = -\frac{2\tilde{g}^{\mu\nu}}{\sqrt{-\tilde{g}}} \frac{\delta \mathcal{L}_m}{\delta \tilde{g}^{\mu\nu}} \, . \tag{2.34}$$

The coupling to matter $A(\phi)$ as well as the potential $V(\phi)$ have to be of a form so that they are symmetric under $\phi \to -\phi$. A commonly considered coupling is

$$A(\phi) = 1 + \frac{\phi^2}{2M^2} + \mathcal{O}\left(\frac{\phi^4}{M^4} \right) \tag{2.35}$$

and the simplest potential can be stated as

$$V(\phi) = -\frac{1}{2}\mu^2\phi^2 + \frac{1}{4}\lambda\phi^4 \, . \tag{2.36}$$

Here, the variables μ and M have the unit of mass and λ is a positive dimensionless coupling constant.

This leaves the effective potential from Eq. (2.33) using non relativistic matter ($\tilde{T} \approx -\tilde{\rho}$) as

$$V_{\text{eff}} = V(\phi) + A^3(\phi) A_{,\phi}(\phi) \tilde{\rho} \tag{2.37}$$

$$= \frac{1}{2} \left(\frac{\rho}{M^2} - \mu^2 \right) \phi^2 + \frac{1}{4}\phi^4 \, , \tag{2.38}$$

where the density $\rho = A^3(\phi)\tilde{\rho}$, which is conserved in the Einstein frame, has been used. In this equation non-ϕ dependent terms have been neglected as they do not change the behavior of the scalar field.

1 This conformal transformation is the equivalent to $\mathcal{C} = A^2$ with the function $\mathcal{C}$ introduced in section 1.2.3.

As done in the previous section, one can write the Christoffel symbols in the Jordan frame as

$$\tilde{\Gamma}_{\mu\nu} = \Gamma^{\alpha}_{\mu\nu} + \delta^{\alpha}_{\nu}\partial_{\mu}\left(\log(A)\right) + \delta^{\alpha}_{\mu}\partial_{\nu}\left(\log(A)\right) - g_{\mu\nu}\partial^{\alpha}\left(\log(A)\right) \ . \tag{2.39}$$

Therefore, the geodesic equation is

$$\ddot{x}^{\alpha} + \Gamma^{\alpha}_{\mu\nu}\dot{x}^{\mu}\dot{x}^{\nu} + 2\partial_{\sigma}\left(\log(A)\right)\dot{x}^{\sigma}\dot{x}^{\alpha} + g^{\alpha\sigma}\partial_{\sigma}(\log(A)) = 0 \ . \tag{2.40}$$

Here, the fact that $g_{\mu\nu}\dot{x}^{\mu}\dot{x}^{\nu} = -1$ has been used for the last term. Taking now the non-relativistic limit in flat spacetime, we obtain for the spacial coordinates:

$$\ddot{\mathbf{x}} = -\vec{\nabla}\left(\log A\right) \ . \tag{2.41}$$

This means one can interpret $\log(A)$ as an additional potential, giving rise to an fifth force.

As Fig. 2.2 shows, the minimum of this effective potential is located at $\phi_{min} = 0$ if $\rho > M^2\mu^2$ (left panel) and different from zero if the density falls below that threshold (right panel). Especially $\phi_{min} = \pm\mu/\sqrt{\lambda}$ if $\rho = 0$. Consequently, the fifth force is screened in regions with high density.

2.2.1 Cosmology

As in the section about the chameleon model the behavior of the symmetron model in outer space is studied using the FLRW metric and non-interacting perfect fluids ($\tilde{T} = \sum_i(-1 + 3w_i)\tilde{\rho}_i$). Then the equation of motion (2.33) becomes

$$\ddot{\phi} + 3H\dot{\phi} + V_{,\phi} + A^3(\phi)A_{,\phi}\sum_i(1 - 3w_i)\tilde{\rho}_i = 0 \tag{2.42}$$

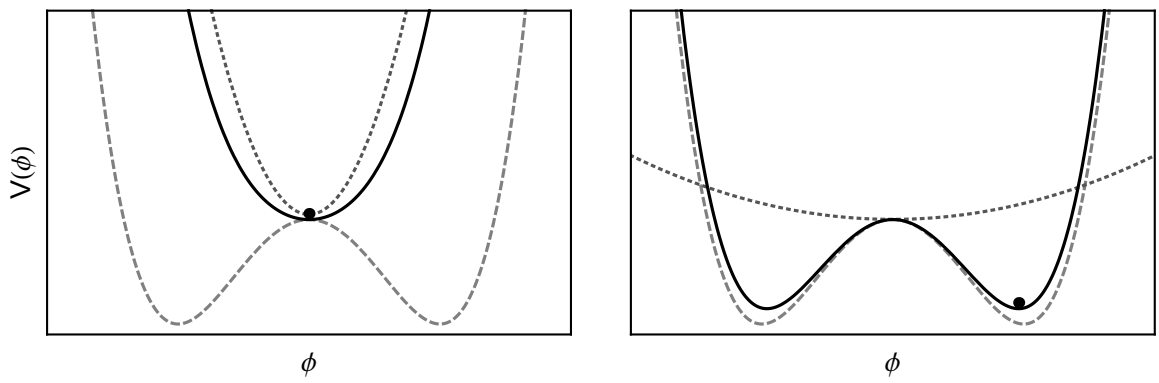

Figure 2.2: The symmetron screening effect: The solid, dashed and dotted lines show respectively the effective potential V_{eff}, the bare potential V and the density dependent component. The black dot illustrates a minimum of the effective potential. On the *left* side the situation is shown in a high-density region: The effective minimum is at $\phi = 0$ and the fifth force is screened. In the *right* graph the field is in a lower density region. ϕ can be at much higher values and therefore a non-neglectable fifth force may be present.

or using the definition of ρ introduced above:

$$\ddot{\phi} + 3H\dot{\phi} + V_{,\phi} + \sum_i \frac{A_{,\phi}}{A^{3w_i}}(1-3w_i)\rho_i = 0 \tag{2.43}$$

This is the same result as obtained for the chameleon model but with changed effective potential:

$$V_{\text{eff}} = V(\phi) + \sum_i A^{1-3w_i}(\phi)\rho_i \tag{2.44}$$

The geodesic equation (2.40) for non-relativistic particles ($v \ll 1$) will become in FLRW metric

$$\ddot{x}^i + 2H\dot{x}^i + 2\partial_0(\log A)\dot{x}^i + \frac{1}{a^2}\partial^i(\log A) = 0\,. \tag{2.45}$$

Often, the time derivative term is neglected as it is assumed that A changes slowly.

2.2.2 Spherical solution

Similarly as done in the previous section a case were a sphere of density ρ and radius R in vacuum is studied. Therefore, the equation of motion (2.33) in the Newtonian limit is written in spherical coordinates and the definition of $\rho = A^3\tilde{\rho}$ has been used:

$$\frac{\mathrm{d}^2\phi}{\mathrm{d}r^2} + \frac{2}{r}\frac{\mathrm{d}\phi}{\mathrm{d}r} = V_{,\phi} + A_{,\phi}\rho \tag{2.46}$$

The boundary conditions are that the solution has to smooth at the origin and take a fixed value at infinity:

$$\left.\frac{\mathrm{d}\phi}{\mathrm{d}r}\right|_{r=0} = 0 \tag{2.47}$$

$$\lim_{r\to\infty} = \phi_\infty \tag{2.48}$$

For the interior solution the right hand side of (2.46), namely the derivative of the effective potential $V_{eff,\phi}$ can be approximated by $V^{(in)}_{eff,\phi}(\phi) = \rho\phi M^2$ because $\rho \gg \mu^2 M^2$. Using this assumption the solution, which also satisfies the boundary condition Eq. (2.47), is

$$\phi^{(in)}(r) = C_1\frac{R}{r}\sinh\left(\frac{\rho}{M}r\right)\,. \tag{2.49}$$

The constant C_1 will be fixed by demanding a smooth solution at the boundary between the interior and the exterior solution.

In order to find the exterior solution, the effective potential outside the sphere is approximated as

$$V^{(out)}_{eff} = \mu^2(\phi - \phi_\infty)^2\,. \tag{2.50}$$

This is a reasonable assumption since the potential only gets important near ϕ_∞. Under this simplification the solution of Eq. (2.46) which fulfills Eq. (2.48) is

$$\phi^{(out)}(r) = C_2 \frac{R}{r} \mathrm{e}^{-\sqrt{2}\mu(r-R)} + \phi_\infty \,. \tag{2.51}$$

Fixing the two integration constants C_1 and C_2 is done by demanding a smooth solution at the boundary $r = R$. This results in:

$$C_1 = \phi_\infty u \,\mathrm{sech} u \tag{2.52}$$

$$C_2 = \phi_\infty \left(u \tanh \frac{1}{u} - 1 \right) \tag{2.53}$$

Here u^2 is a thin-shell factor and can be interpreted the same way as in the chameleon model

$$u^2 \equiv \frac{\Delta R_s}{R_s} = \frac{M^2}{6 M_{\mathrm{Pl}}^2 \Phi} \tag{2.54}$$

with the Newtonian gravitational potential $\Phi = \rho R^2 / 6 M_{\mathrm{Pl}}^2$.

In order to complete the connection to the chameleon mechanism to simplify matters for the future treatment, it is possible (Hinterbichler & Khoury, 2010; Hinterbichler et al., 2011) to consider the additional force on a test particle around the spherical object. As the mass of the scalar field in vacuum should be very light, Eq. (2.41) can be expanded around μ in order to get a approximation for the behavior of the fifth force:

$$\ddot{\mathbf{x}}_{\mathrm{Fifth}} \approx -\frac{\mu}{\sqrt{\lambda} M^2} \frac{\partial \phi}{\partial r} \,. \tag{2.55}$$

As done in the chameleon section before, two kinds of solutions can be considered in order to expand Eq. (2.51), the screened ($\Delta R / R \ll 1$) and unscreened ($\Delta R / R \gg 1$) one. In the screened case the additional acceleration compared to the Newtonian one is

$$\ddot{\mathbf{x}}^{(\mathbf{s})}_{\mathrm{Fifth}} \approx 6 \frac{\Delta R}{R} \frac{\mu^2 M_{\mathrm{Pl}}^2}{\lambda M^4} \,, \tag{2.56}$$

and for unscreened objects this becomes

$$\ddot{\mathbf{x}}^{(\mathbf{u})}_{\mathrm{Fifth}} \approx 2 \frac{\mu^2 M_{\mathrm{Pl}}^2}{\lambda M^4} \,. \tag{2.57}$$

Note, if we identify $\frac{\mu^2 M_{\mathrm{Pl}}^2}{\lambda M^4}$ with β the result is the same as in the chameleon case.

This relations will be used for the spherical collapse model in Section 4.2.

2.3 The Hu-Sawicky $f(R)$ model

As we have seen in section 1.2.6, $f(R)$-models can be treated as scalar-tensor theories, if we redefine the metric the following way:

$$\tilde{g}_{\mu\nu} = \mathrm{e}^{2\beta\phi/M_{\mathrm{Pl}}} g_{\mu\nu} \quad \text{with } \beta = \frac{1}{\sqrt{6}} \,. \tag{2.58}$$

Under this transformation to the Einstein frame metric $g_{\mu\nu}$, a scalar field appears with

$$f_R = \mathrm{e}^{-2\beta\phi/M_{\mathrm{Pl}}} \tag{2.59}$$

and a potential

$$V(\phi) = M_{\mathrm{Pl}}^2 \frac{f_R R - f}{2f_R^2} \,. \tag{2.60}$$

as stated in Eq. (1.62). This means, certain $f(R)$-models have a resulting potential $V(\phi)$, which fulfills the condition Eq. (2.10) and fall, therefore, in the category of chameleon models.

One of these is the previously introduced model by Hu & Sawicki (2007), in which

$$f(R) = R - m^2 \frac{c_1 (R/m^2)^n}{1 + c_2 (R/m^2)^n} \tag{2.61}$$

where c_1, c_2, m and n are positive constants. Furthermore, m is given by

$$m^2 = M_{\mathrm{Pl}}^2 \bar{\rho}_{m0}/3 = \frac{H_0^2}{\Omega_{m0}} \tag{2.62}$$

with $\bar{\rho}_{m0}$ being the average matter density today.

Taking the high curvature limit, that is expanding Eq. (2.61) around $m^2/R \to 0$ results in

$$f(R) \approx R - \frac{c_1}{c_2} m^2 + \frac{c_1}{c_2^2} m^2 \left(\frac{m^2}{R} \right)^n \,. \tag{2.63}$$

Notice how the constant second term plays the role of a cosmological constant and in the case $c_1/c_2^2 \to 0$ and $c_1/c_2 m^2 \to 2\Lambda$ we recover the standard ΛCDM case.

As we can see the model has three free parameters: c_1, c_2 and n. In order to obtain background ΛCDM evolution we set

$$\frac{c_1}{c_2} m^2 = 2\Lambda = 16\pi G \rho_\Lambda \,. \tag{2.64}$$

Furthermore, it is convenient to introduce the background curvature today $f_{R0} \equiv \mathrm{d}f/\mathrm{d}R\big|_{a=a_0}$ and write Eq. (2.63) as

$$f(R) = R - 16\pi G \rho_\Lambda - \frac{f_{R0} - 1}{n} \frac{R_0^{n+1}}{R^n} \,. \tag{2.65}$$

The two remaining parameters n and f_{R0} specify the evolution of the Compton wavelength of the scalar field and the deviation from ΛCDM respectively. The constraints get weaker with increasing n because the screening mechanism works more efficiently (Ferraro et al., 2011) and for $f_{R0} \to 1$ ΛCDM is recovered.

Using now (2.59) and (2.65) we obtain in leading order

$$\frac{2\beta\phi}{M_{\rm Pl}} = (f_{R0}-1)\frac{R_0^{n+1}}{R^{n+1}} \,. \tag{2.66}$$

Therefore, the potential (2.60) can be written as

$$V(\phi) = \left(1+\frac{4\beta\phi}{M_{\rm Pl}}\right)\rho_\Lambda + \frac{n+1}{2n}M_{\rm Pl}^2(f_{R0}-1)R_0\left(\frac{2\beta\phi}{M_{\rm Pl}(1-f_{R0})}\right)^{n/(n+1)} \,. \tag{2.67}$$

According to Brax et al. (2008) the condition for an $f(R)$ model to have chameleon like behavior is

$$V'(\phi) < 0, V''(\phi) > 0, V'''(\phi) < 0 \tag{2.68}$$

which is fulfilled for the potential given in the region

$$0 < \phi < M_{\rm Pl}\frac{1-f_{R0}}{2\beta}\left(\frac{R_0 M_{\rm Pl}^2}{4\rho_\Lambda}\right)^{n+1} \tag{2.69}$$

The curvature today can be found using the Einstein equations Eq. (1.5) with a FLRW metric and is given by

$$\begin{aligned} R_0 &= M_{\rm Pl}^{-2}\sum_i \rho_i(1-3w_i) \\ &= 3H_0^2\left(\Omega_{m,0}+4\Omega_{\Lambda,0}\right) \end{aligned} \tag{2.70}$$

where in the first line the sum is over all matter species and in the second line radiation is ignored as it has a neglectable energy content today. This transforms Eq. (2.69) into

$$0 < \phi < M_{\rm Pl}\frac{1-f_{R0}}{2\beta}\left(\frac{\Omega_{m,0}}{4\Omega_{\Lambda,0}}+1\right)^{n+1} \,. \tag{2.71}$$

This means, the Hu-Sawicky model has a chameleon mechanism if the free parameter f_{R0} is between 0 and 1. This can be also shown by analyzing the effective potential used in Section 2.1. In first order this reads

$$V_{eff} = V(\phi) + \frac{\beta\phi}{M_{\rm Pl}}\rho$$

and the minimum is given by $V'_{eff}\big|_{\phi=\phi_{min}} = 0$ and can be written as

$$\begin{aligned} \phi_{min} &= \frac{M_{\rm Pl}|1-f_{R0}|}{2\beta}\left[\frac{M_{\rm Pl}^2 R_0}{\rho+4\rho_\Lambda}\right]^{n+1} \\ &= \frac{M_{\rm Pl}|1-f_{R0}|}{2\beta}\left[\frac{\Omega_{m,0}+4\Omega_{\Lambda,0}}{\Delta_\rho+4\Omega_{\Lambda,0}}\right]^{n+1} \end{aligned} \tag{2.72}$$

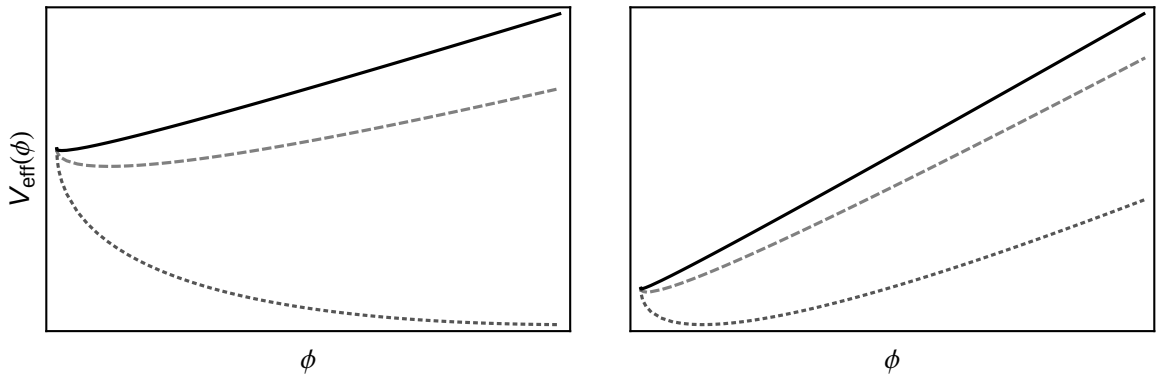

Figure 2.3: The chameleon effect in the Hu-Sawicky model. The left panel shows a lower density region ($\Delta_\rho = 170$) and the right panel a higher density region ($\Delta_\rho = 500$) where the minima is closer to $\phi = 0$. The solid black, dashed gray and dotted gray lines represent the values $|f_{R0} - 1| = (10^{-6}, 10^{-5}, 10^{-4})$, respectively. This behavior is the same as observed in Fig. 2.1.

with $\Delta_\rho = \rho/\rho_{c,0}$. It is to note that ϕ_{min} approaches zero with a growing ρ which causes the screening of the fifth force as seen before.

The screening effect is illustrated in Fig. 2.3 for three different values of f_{R0}. While for the low density region ($\Delta_\rho = 1$) shown in the left panel no screening is active, on the right panel only the $1 - f_{R0} = 10^{-4}$ model is not fully screened. Therefore, not only the additional force is weaker for values of f_{R0} closer to one – which can be noted through the slope of the curve, that is not directly proportional to the fifth force but related to it[1] – but also the screening kicks in for a lower densities.

2.4 Gravitational redshift in the symmetron and chameleon models

Already Eq. (2.22) in the chameleon case and Eq. 2.33) in the symmetron case show that photons with an equation of state $w_\gamma = 1/3$ and therefore traceless energy-momentum tensor do not "feel" the influence of the fifth force. Another way of seeing this is by transforming the geodesics of a photon with a conformal transformation as introduced in Sec. 1.2.3. Photons travel on null-geodesics (Hartle, 2003, Sec. 5.5), meaning if u^μ is the 4-velocity of a photon then the equation

$$g_{\mu\nu} u^\mu u^\nu = 0 \tag{2.73}$$

holds. In terms of the conformally transformed metric, this equation becomes

$$\tilde{g}_{\mu\nu} u^\mu u^\nu = 0 \,, \tag{2.74}$$

1 Since the fifth force is given by $\mathbf{F}_{\text{Fifth}} \propto \vec{\nabla}\phi$, as shown in Sec. 2.1

which is exactly the same equation as above. Physically speaking: The lightcone is preserved under a conformal transformation. This result is not too suprising as angles and causality are per definition preserved.

Consequently, gravitational redshift is only influenced by the Newtonian potential and not by $V_{\text{eff}}(\phi)$. Nevertheless, the gravitational redshift profile of clusters of galaxies can be different in these screened modified gravities as the underlying density distribution is affected by the additional force and therefore indirectly also the gravitational redshift profile.

3

The N-body Code and Simulation Parameters

In this chapter a short introduction in the tool of choice for this work is given. It is split into three parts: In the first part, a short general introduction to cosmological N-body simulations and their key concepts is given. The description of the simulation code used for this work is presented in the second part. Finally, in the last part, the runtime parameters for the simulation runs are provided and the halo-finding procedure is explained.

3.1 Introduction to N-body simulations

Steadily increasing computational power and the highly non-linear nature of the problem have made N-body simulations a very popular tool for studying large scale structure formation in the universe.

In the last decade a number of simulations have been performed and some of them included an impressive number of particles (see e.g. Kuhlen et al. (2012) for an overview). Different algorithms have been developed to optimize this computationally expensive task.

In the following section a brief overview over existing algorithms is given with focus on the code used in this project.

3.1.1 Concepts

N-body simulations can be split in two categories: Collisional and collisionless N-body codes. In order to determine which algorithm is more appropriate to model a physical system, a range of interactions can be defined. According to Hockney & Eastwood (1988), for gravitational systems this is given by

$$\lambda_i = \frac{Gm^2}{\frac{1}{2}mv^2} \,. \tag{3.1}$$

If the average of λ_i is small compared to the mean inter-particle spacing, a computationally much less expensive collisionless N-body code can be used instead of the collisional algorithm. Fortunately the galaxy density in the universe is very low which allows us to use collisionless N-body codes for cosmological applications.

A collisionless system is described by the collisionless Boltzmann equation (CBE)

$$\frac{\mathrm{d}f}{\mathrm{d}t} = \frac{\partial f}{\partial t} + \frac{\partial f}{\partial \mathbf{x}} \cdot \dot{\mathbf{x}} + \frac{\partial f}{\partial \dot{\mathbf{x}}} \cdot \ddot{\mathbf{x}} = 0, \tag{3.2}$$

where $f(\mathbf{x},\dot{\mathbf{x}},t)$ is the probability density function giving the probability that inside the six-dimensional differential volume $\mathrm{d}^3\mathbf{x}\,\mathrm{d}^3\dot{\mathbf{x}}$ at time t $\mathrm{d}N$ particles are located.

$$f(\mathbf{x},\dot{\mathbf{x}},t)\mathrm{d}^3\mathbf{x}\ \mathrm{d}^3\dot{\mathbf{x}} = \mathrm{d}N \tag{3.3}$$

For gravitational systems Eq. (3.2) can be simplified using the equation $\ddot{\mathbf{x}} = -\nabla\Phi$:

$$\frac{\partial f}{\partial t} + \frac{\partial f}{\partial \mathbf{x}} \cdot \dot{\mathbf{x}} - \frac{\partial f}{\partial \dot{\mathbf{x}}} \cdot \frac{\partial \Phi}{\partial \mathbf{x}} = 0. \tag{3.4}$$

The resulting expression is a non linear partial differential equation in seven dimensions. This means it is not directly numerically solvable if it is not in or close to equilibrium state ($\frac{\partial f}{\partial t} = 0$). Consequently a different method is needed.

N-body simulations are based on the idea to model only N different points in phase space and to obtain the observables afterwards as an ensemble average in a Monte-Carlo like fashion via

$$\langle O \rangle (t) = \frac{1}{N} \int \mathrm{d}^3\mathbf{x}\ \mathrm{d}^3\dot{\mathbf{x}}\, O(\mathbf{x},\dot{\mathbf{x}},t) f(\mathbf{x},\dot{\mathbf{x}},t) \tag{3.5}$$

$$\approx \frac{1}{N} \sum_{i=1}^{N} O(\mathbf{x}_i,\dot{\mathbf{x}}_i,t) f(\mathbf{x}_i,\dot{\mathbf{x}}_i,t)\ , \tag{3.6}$$

here $\mathbf{x}_i$ and $\dot{\mathbf{x}}_i$ are the position and the speed of the ith particle respectively.

Because of $\frac{\mathrm{d}f}{\mathrm{d}t} = 0$ as stated in the CBE Eq. (3.2), Eq. (3.6) can be rewritten as

$$\langle O \rangle (t) \approx \frac{1}{N} \sum_{i=1}^{N} O(\mathbf{x}_i,\dot{\mathbf{x}}_i,t) W_i, \tag{3.7}$$

where $W_i = f(\mathbf{x}_i,\dot{\mathbf{x}}_i,t)|_{t=t_0}$ is the weight of the particles representing the distribution function at the initial time t_0.

The actual initial conditions $(\mathbf{x}_i,\dot{\mathbf{x}}_i)|_{t=t_0}$ are chosen by the user. Thus, a lot of particles may be placed in an area of particular interest to achieve a higher resolution locally (Bertschinger, 2011).

3.1.2 Gravity calculation

To obtain the wanted particle trajectories, for each particle i the equations

$$\dot{\mathbf{v}}_i = -\nabla\Phi(\mathbf{x}_i) \tag{3.8}$$

$$\dot{\mathbf{x}}_i = \mathbf{v}_i \tag{3.9}$$

$$\nabla^2\Phi = 4\pi G\rho \tag{3.10}$$

have to be solved (Teyssier, 2002). For cosmological applications this is done in comoving coordinates, meaning that $\mathbf{x}_i'$ and $\mathbf{v}_i'$ are taken with respect to the expanding background spacetime:

$$\mathbf{x}_i' = \frac{\mathbf{x}_i}{a(t)}, \tag{3.11}$$

where $a(t)$ denotes the cosmological expansion factor.

Expressing $\dot{\mathbf{v}}_i$ in the comoving coordinates and using this in Eq. (3.8) results in:

$$\dot{\mathbf{v}}_i' + 2\mathbf{v}_i' H = -\frac{1}{a}\nabla\Phi - \mathbf{x}_i'\frac{\ddot{a}}{a}\,, \tag{3.12}$$

where H is the Hubble constant introduced Section 1.1.3.

By defining the spatial derivative with respect to the comoving coordinates $\nabla' \equiv a\nabla$ and

$$\Phi' \equiv a\Phi + \frac{1}{2}\ddot{a}a^2\mathbf{x}_i'^2\,, \tag{3.13}$$

Poisson's equation (3.10) can also be expressed in the comoving coordinate set

$$\nabla'^2\Phi' = 4\pi G\rho a^3 + 3\ddot{a}a^2\,. \tag{3.14}$$

This equation can be further simplified using the result from the second Friedmann equation (1.28) and defining the comoving density $\rho' \equiv \rho a^3$ which leads (Hockney & Eastwood, 1988) to the set of equations:

$$\dot{\mathbf{v}}_i' + 2H\mathbf{v}_i' = -\frac{1}{a^3}\nabla'\Phi' \tag{3.15}$$

$$\dot{\mathbf{x}}_i' = \mathbf{v}_i' \tag{3.16}$$

$$\nabla'^2\Phi' = 4\pi G\left(\rho' - \rho_0\right) \tag{3.17}$$

These equations can be derived in an alternative way, taking the Newtonian gauge metric[1] given by

$$\mathrm{d}s^2 = -(1+2\Phi)\,\mathrm{d}t^2 + a(t)^2(1-2\Phi)\delta_{ij}\,\mathrm{d}x^i\,\mathrm{d}x^j \tag{3.18}$$

as a basis. Then, the geodesic equation for particle i becomes

$$\ddot{\mathbf{x}}_i + 2H\dot{\mathbf{x}}_i + \frac{1}{a^2}\nabla\Phi = 0 \tag{3.19}$$

which is identical to Eq. (3.15).

1 The Newtonian gauge has strictly speaking two scalar degrees of freedom often denoted as Φ and Ψ. However, without anisotropic stress the Einstein equations give $\Phi = -\Psi$ (Dodelson, 2003).

Obtaining the density

In order to solve these equations it is crucial to obtain the particle density at a given position $\rho(\mathbf{x})$. Simply utilizing the Monte Carlo estimate (3.7) will just lead to a sum of delta functions. A commonly used solution is to widen the delta peaks which leads to the density estimate (Silverman, 1986)

$$\rho \approx \sum_i \frac{m_i}{\varepsilon^3} \tilde{K}\left(\frac{|\mathbf{x}-\mathbf{x}_i|}{\varepsilon}\right) , \tag{3.20}$$

with the normalized function $\tilde{K}(x)$ being the kernel function, m_i the mass of the particle i and ε the softening length that controls how fast the kernel function falls off.

Applying (3.17) to (3.20) results in an estimate for the potential Φ (Dehnen & Read, 2011):

$$\Phi(\mathbf{x}) \approx -\sum_i \frac{Gm_i}{\varepsilon} \hat{K}\left(\frac{|\mathbf{x}-\mathbf{x}_i|}{\varepsilon}\right) \tag{3.21}$$

The choice of the kernel function and the softening length is not trivial. E.g. the Plummer softening is used widely (Dehnen & Read, 2011) where

$$\tilde{K}(x) = 3/(4\pi)\left(x^2+1\right)^{-5/2} \quad \text{and} \quad \hat{K}(x) = \left(x^2+1\right)^{-1/2} . \tag{3.22}$$

Therefore, the estimate for the potential becomes

$$\Phi(\mathbf{x}) \approx -G\sum_i \frac{m_i}{\sqrt{|\mathbf{x}-\mathbf{x}_i|^2+\varepsilon^2}} . \tag{3.23}$$

The advantages of this (as in most other kernel functions used) is the non-singularity at $x = 0$ and the reduction of numerical artifacts due to close encounters which are not described by collisionless but instead by collisional N-body codes (Dehnen & Read, 2011).

Another choice often used in grid-based force calculation methods (see below) is the cloud in cell (CIC) scheme (Birdsall & Fuss, 1969). Here the kernel function in equation (3.20) is given by a linear interpolation:

$$\tilde{K}(x) = \begin{cases} 1-x & \text{if } |x|<1 \\ 0 & \text{otherwise} \end{cases} \tag{3.24}$$

Force calculation methods

In theory it is possible to carry out the sum of Eq. (3.23) (i.e. its derivative) in order to obtain the force. In practice this direct summation is too slow and a number of more rapid algorithms were developed.

The simplest grid-based method is the **particle-mesh (PM)** algorithm (Hockney & Eastwood, 1988; Klypin & Shandarin, 1983). The density is calculated at every node of a regular

grid. This allows to solve the equations (3.17) and (3.15) for the potential and the acceleration respectively at every grid point using the computationally cheap fast Fourier transform (FFT) (Cooley & Tukey, 1965). Afterwards the acceleration can be interpolated back to the particles' positions and their coordinates updated accordingly. The automatic periodic boundary conditions that come with the FFT and the high performance ($\mathcal{O}(N)+\mathcal{O}(N\log N)$ (Bertschinger, 1998)) made this algorithm popular for cosmological usage. The main disadvantage of this algorithm is the poorly modeled force for particles that are closer than several grid spacings. This means in order to obtain good results the global grid resolution has to be increased which is computationally very expensive.

A logical extension to the PM method is therefore to calculate the forces for particles closer than two or three grid spacings via direct summation. This idea leads to the **particle-particle/particle-mesh ($\mathbf{P^3M}$)** algorithm (Efstathiou & Eastwood, 1981; Hockney et al., 1974). The relative high precision achieved through the direct summation stands against the high computational cost if dense regions occur.

One possible solution to this is to use multiple grids: In the coarse grid Poisson's equation is solved with periodic boundary conditions whereas in high-density regions a finer grid will be added with fixed (Dirichlet) boundary conditions. This **adaptive particle-particle/particle-mesh ($\mathbf{AP^3}$)** method (Couchman, 1991) still uses direct summation for particles closer than several grid spacings but lowers the computational cost by using locally the PM method in the finer grids.

Another approach is to stick to direct summation but to group close particles together and treat them as one particle if necessary. This means for a particle further away from a given group of particles, it is then not necessary to interact with each particle belonging to the group but instead with the group as a whole. To achieve this the **TREE** algorithm (Barnes & Hut, 1986) starts also with a regular grid. Note that this grid is not used to solve the Fourier transformed Poisson's equation as the methods described before but that each cell represents a group of particles. If a group contains more particles than some threshold, the cell is split with the newly created cells being the children of the original cell. The result is a tree structure of cells with each "leaf" (a cell that has no children cells) having roughly the same number of particles. The further apart a particle is to a given point, the higher up the tree is the node with which the particle can interact. This leaves a direct interaction only for very few particles. A big advantage of this approach is the speed ($\mathcal{O}(N)\log N$) by keeping the errors low (Hernquist, 1987). To achieve periodic boundary conditions important for cosmological usage, various TREE codes (i.e. Bouchet & Hernquist (1988)) use a method named Ewald (1921) summation.

A unification of the TREE and the AP^3M methods is found in the **adaptive mesh refinement (AMR)** algorithm (Jessop et al., 1994; Kravtsov et al., 1997). Instead of simply adding finer grids onto the coarse grid at various regions as done in the AP^3M method, a tree of subgrids is built. It is therefore possible to use very fine grids locally which makes direct summation obsolete. This has two main advantages: First the force resolution is fully spatially adaptive and not uniform as in the TREE or (A)P^3M methods. Knebe et al. (2000) show that this approach preserves halo properties better. Secondly, leaving out the direct particle-particle interaction simplifies the usage of a modified Lagrangian.

3.2 The simulation code

The simulation code used called `ISIS` (Llinares et al., 2013) is based on the `RAMSES` code by Teyssier (2002). The AMR method (see section 3.1 for an introduction to the various N-body methods) used allows to include directly modified Lagrangian as mentioned before. In the following the structure of the original `RAMSES` code is summarized and the scalar field equations are introduced.

3.2.1 RAMSES code structure

The `RAMSES` code (Teyssier, 2002) is a heavily parallelized multi-grid algorithms and performs for every timestep the following sub-steps:

1. Compute the density ρ on the mesh using the cloud in cell scheme described above.
2. Solve the Poisson's equations in order to get the potential Φ. In order to achieve this, the Gauss Seidel method with successive overrelaxation and chessboard ordering is employed. Additionally, Dirichlet boundary conditions are used. This step will be explained in more detail below.
3. Compute acceleration on the mesh.
4. Compute the particles' acceleration using an inverse CIC.
5. Update the velocity of each particle using the acceleration.
6. Update the position of each particle using the velocity.

In order to obtain the potential for the finer grids in step 2, the boundary conditions have to be fixed first. Therefore, the potential already obtained for the grid next in cell size is linearly interpolated to a temporary buffer region used as the boundary values. The next step is to solve the Poisson's equation with these boundary conditions. To achieve this the Gauss Seidel method with successive overrelazation and cheeseboard ordering (Press et al., 1992) is used. The concept of the Gauss Seidel method with successive overrelaxation is explained in the appendix in Sec. A.2.

3.2.2 The ISIS code

The simulation code used in this work is `ISIS` (Llinares et al., 2013), which is a modification of `RAMSES` (Teyssier, 2002), that includes the development of a scalar field ϕ. Hence, the equation (3.15) is altered to

$$\dot{\mathbf{v}}_i' + 2H\mathbf{v}_i' = -\frac{1}{a^3}\nabla'\Phi' - \mathbf{F}(t,\phi,...) \tag{3.25}$$

where $\mathbf{F}$ describes the supplementary influence of the scalar field on the particles' trajectories and, consequently, is a function of time, ϕ and its derivatives. In addition, the equation describing the development of the scalar field itself is solved

$$\nabla^2\phi = S(t, \rho, \phi) \tag{3.26}$$

with the source function of the scalar field on the right hand side.

For scalar-tensor theories as defined in Sec. 2.2, i.e. introduced via $\tilde{g}_{\mu\nu} = A^2(\phi)g_{\mu\nu}$, the functions $\mathbf{F}$ and S are given by

$$\mathbf{F} = 2\frac{\partial}{\partial t}(\log A)\mathbf{x} + \frac{1}{a^2}\vec{\nabla}(\log A) \tag{3.27}$$

$$\mathbf{S} = V_{,\phi} - A_{,\phi}\rho \; . \tag{3.28}$$

These equations where derived in a general form in Section 2.2 (see Eqs. (2.37) and (2.40)). The Newtonian gauge metric (3.18) can then be used as in Sec. 3.1.2 to bring them in the above form. It is to note, that the usual approximation (Oyaizu, 2008), that is to work in the quasi-static limit, i.e. to drop the terms including time-derivatives, has been applied.

In a similar form these equations where also implemented in the `ECOSMOG` code (Li & Hu, 2011), which is also based on the `RAMSES` code, an N-body code by Zhao et al. (2011) based on `MLAPM` (Knebe et al., 2001) and in a code by Oyaizu (2008).

Symmetron implementation

The symmetron implementation in `ISIS` uses the same functions $V(\phi)$ and $A(\phi)$ introduced in Sec. 2.2. Equation (3.25) turns for this model into

$$\ddot{\mathbf{x}} + 2H\dot{\mathbf{x}} + \frac{1}{a^2}\nabla\Phi + \frac{1}{(Ma)^2}\phi\nabla\phi = 0 \; . \tag{3.29}$$

The same result as could be obtained using the general modified geodesics (2.40) using the Newtonian gauge metric.

Similar to Winther et al. (2011), instead of the original parameters (μ, M, λ), more physical parameters where introduced which are all linked to the properties of the scalar field in vacuum. Firstly, the range of the field

$$L = \frac{1}{\sqrt{2}\mu} \; , \tag{3.30}$$

secondly, the expansion factor for which the symmetry is broken in the background level

$$a^3_{ssb} = \frac{\Omega_{m,0}\rho_{c,0}}{\mu^2 M^2} \tag{3.31}$$

and last a dimensionless coupling constant

$$\beta = \frac{\mu M_{\rm Pl}}{M^2\lambda} \; . \tag{3.32}$$

In addition, the scalar field itself is normalized to its vacuum expectation value:

$$\chi \equiv \phi/\phi_0 = \frac{\phi a_{ssb}^3}{6H_0^2 M_{\rm Pl} L^2 \beta \Omega_{m,0}} \tag{3.33}$$

With these redefinitions Eq. (3.29) can be rewritten as

$$\ddot{\mathbf{x}} + 2H\dot{\mathbf{x}} + \frac{1}{a^2}\nabla\Phi + \frac{6H_0^2 L^2 \beta^2}{a^2 a_{ssb}^3}\chi\nabla\chi = 0\ . \tag{3.34}$$

The equation of motion of the scalar field (3.26) is in this case

$$\nabla^2\chi = \frac{a^2}{2L^2}\left[\left(\frac{a_{ssb}}{a}\right)^3 \eta\chi - \chi + \chi^3\right] \tag{3.35}$$

with $\eta \equiv \rho_m a^3/(\Omega_{m,0}\rho_{c,0})$. This means η describes the local density normalized to the average matter density.

$f(R)$ implementation

The Hu-Sawicky model was discussed in Sec. 2.3, where the parameters used in the simulation, namely n and f_{R0}, are also introduced. Basically, the effective potential and the conformal transformation described there can be used directly to solve the modified geodesics and the scalar field evolution numerically, as done for the symmetron model. The equation tho solve would be

$$\frac{1}{a^2}\nabla^2 f_R = \Omega_m H_0^2\left[\left(1 + 4\frac{\Omega_\Lambda}{\Omega_m}\right)\left(\frac{f_{R0}-1}{f_R - 1}\right)^{\frac{1}{n+1}} - \left(a^{-3} + 4\frac{\Omega_\Lambda}{\Omega_m}\right) - \eta a^{-3}\right]\ . \tag{3.36}$$

Practically, solving this equation numerically is not possible due to the singularity at $f_R = 0$. Therefore, a field redefinition

$$f_R \propto \mathrm{e}^u \tag{3.37}$$

is a better choice. This leads to the code formulas described in detail in Llinares et al. (2013), which are similar but not identical to the implementations by Li et al. (2012) and Oyaizu (2008).

3.3 Simulation parameters

All simulation runs contained 512^3 particles with a mass of $9.26138 \times 10^9\, M_\odot/h$ which represent the total matter distribution. This corresponds to a matter content of 26.7% ($\Omega_{b,0} = 0.045$, $\Omega_{\rm cdm,0} = 0.222$ and $\Omega_{\Lambda 0} = 0.733$). The simulation box has a side-length of $256\, h^{-1}$Mpc and periodic boundary conditions. The data sets used are the snapshots taken at $z = 0$.

Name	$\lvert f_{R0} - 1\rvert$	n
fofr4	10^{-4}	1
fofr5	10^{-5}	1
fofr6	10^{-6}	1

(a) $f(R)$ runs

Name	z_{ssb}	β	L in Mpc h^{-1}
symm_A	1	1	1
symm_B	2	1	1
symm_C	1	2	1
symm_D	3	1	1

(b) symmetron runs

Table 3.1: Parameters of the different simulation runs. *Left:* The $f(R)$ parameters are n and the value of $\mathrm{d}f/\mathrm{d}R$ today. *Right:* The symmetron parameters are the redshift of the symmetry breaking $z_{ssb} = 1/a_{ssb} - 1$, the coupling β and the length scale of the fifth force L.

All simulation runs were using the same initial conditions, which were generated by the `MPGRAFIC` (Prunet et al., 2008) program. The parameters for the $f(R)$ and the symmetron models are summarized in table 3.1.

In the case of the $f(R)$-gravity the parameter n was fixed to 1 while f_{R0} took values from 10^{-6}, which resulted in hardly any deviation from ΛCDM, to 10^{-4}, which is on the border of violating cluster abundance constraints (Ferraro et al., 2011). The runs were named *fofr4*, *fofr5* and *fofr6* for the values 10^{-4}, 10^{-5} and 10^{-6}, respectively.

For the symmetron model mainly the time of the symmetry breaking was varied while leaving the others constant: a_{ssb} was set to the values 1/2, 1/3 and 1/4 for the simulation runs *symm_A*, *symm_B* and *symm_D*, respectively. For each of these models β and $L/(\mathrm{Mpc}/h)$ were chosen to be unity. The run named *symm_C* stands out as it has the same symmetry breaking time as *symm_A* but an altered β value of 2.

3.4 Post-processing: Identifying the halos

The output of an N-body simulation is usually limited to the position and a few other attributes of the single particles. In order to determine the position and other attributes of gravitationally bound objects – halos or clusters – the N-body simulation output needs to be post-processed with a so-called *halo finder*.

To achieve this mainly two different approaches are used: In the spherical overdensity (SO) algorithms the particle density peaks are found and then particles around them are being defined as part of the halo until the particle density falls below a certain threshold. This top-down design is implemented in AHF (Knollmann & Knebe, 2009), BDM (Klypin et al., 1999), SKID (Stadel, 2001) and others. Alternatively, nearby particles can be grouped together either using a linking length in the friends-of-friends (FOF) algorithms or by "hopping" from a particle to the densest neighbor (HOP). These down-top designs are used in the FOF case e.g. by SUBFIND (Springel et al., 2001), FOF (Davis et al., 1985) or pFOF (Habib et al., 2009) and AdaptaHOP (Tweed et al., 2009) in the HOP case. Both of these approaches can be extended to phase-space, as it is done e.g. in 6DFOF (Diemand et al., 2006). For

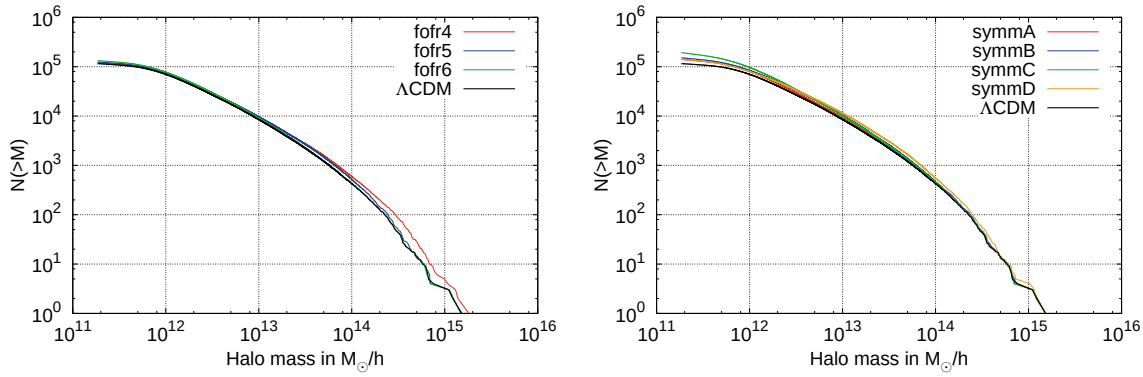

Figure 3.1: Halo mass functions of the data sets. *Left panel:* The ΛCDM and the $f(R)$ data sets. The total number of halos is 115 858, 120 203, 124 404 and 133 241 for the ΛCDM, fofr4, fofr5 and fofr6 data sets, respectively. *Right panel:* The ΛCDM and the symmetron data sets. The total number of halos for the symmetron models is 141 131, 152 307, 193 814 and 141 100 in alphabetic order.

a more detailed overview of current halo finding algorithms as well as their comparison see Knebe et al. (2011).

The halo finder chosen for this work is Rockstar (Behroozi et al., 2013), a publicly available FOF code. Through its ability to work in six dimensions (even seven if simulation snapshots for multiple timesteps are available) and adaptive linking length, Rockstar shows excellent results in halo finding as well as in calculating the halo properties (Knebe et al., 2011). Additionally, Rockstar is a highly efficient code with only $5 - 10$ CPU hours and 60 GB of memory required per billion particles analyzed (at $z = 0$).

The algorithm works roughly as follows: First the simulation box is divided into 3D FOF groups. These groups are then spread over the available processors. In each group the nearest neighbors are found using the phase-space metric by Gottloeber (1998). The distance between two particles with positions $\mathbf{x}_{1,2}$ and velocities $\mathbf{v}_{1,2}$ is given by:

$$d_{1,2} = \sqrt{\frac{|\mathbf{x}_1 - \mathbf{x}_2|^2}{\sigma_x^2} + \frac{|\mathbf{v}_1 - \mathbf{v}_2|^2}{\sigma_v^2}} \tag{3.38}$$

Consequently, the definition of distance within each subgroup depends on the velocity dispersion σ_v and position dispersion σ_x. The linking length is then chosen so that 70% of all particles in a subgroup are linked together. This results in a high precision of finding substructures. Afterwards the last two steps (namely defining the metric and linking the particles together) are repeated over each new subgroup. Finally, when a minimum number of particles are left in a subgroup, this group is defined as seed of a halo and each particle is defined as part of the closest halo. Eventually, gravitationally unbound particles are removed and halo properties calculated. A more detailed explanation about the Rockstar halo finder can be found in Behroozi et al. (2013).

In our case Rockstar was run with the virial radius being the radius R_{200c}, meaning the boundary of the halo is the threshold of 200 times the critical density today. This number was initially chosen to be able to better compare the results with other papers as often the same criteria is picked. There were, however, tests made with the criteria from Bryan & Norman (1998), which corresponds roughly to 360 times the background density today (Behroozi et al., 2013), that lead to the same results.

The proper treatment of halo finding in the self-screening models considered is, however, not to use a constant like 200, but instead adapt this number depending on the halo mass (see section 4.2). This treatment needs a modification of the halo finding code which has not yet been done (see for a summary of the current state in halo finding Knebe et al. (2013)) and goes beyond the scope of this work. Instead, the results obtained with $R_v = R_{200c}$ from ΛCDM were also compared with $R_v = R_{160c}$ for the most extreme models without finding a big difference.

As Rockstar returns a halo-subhalo tree structure but the gravitational well of a halo is due to the host halo, the next step taken was to flatten the hierarchy, i.e. to attach each particle to its "mother halo". This means all particles inside the radius R_{200c} or are member of a halo which has its center inside this radius are defined to be part of a halo. For each of this newly organized halos the properties like mass are updated. Special attention was in this respect given to the calculation of the energies as these were used to find out whether a halo is in a virialized state or not. This subject is covered in the next section.

Our samples contain each around 120,000 clusters. For the ΛCDM run around 73,000 of them contain more than 100 particles and circa 9200 more than 1000 particles. In Fig. 3.1 the halo mass function, i.e. the number of halos bigger than a given mass, is shown. An in-depth interpretation on the change of the halo mass functions in the symmetron and chameleon model was done by Brax et al. (2012, 2013) and is not subject of this work.

4

Spherical Collapse and Virialization

In order to study halo properties it is crucial not to mix clusters that are dynamically relaxed and those which have not reached such an equilibrium state yet as the two groups have a different distribution of halo properties (Shaw et al., 2006). Using the whole cluster sample and not separating these two groups may therefore lead to a skewed mean and higher noise. Especially when comparing the effect of different gravitational theories below Mpc scale – as done in this work – a combination of the two groups may lead to a false interpretation. This misinterpretation can for example occur since it might not be clear if the change is happening on an actual halo property or if the number of unrelaxed objects change.

Measuring the level of relaxation – or virialization – can be done using the virial theorem, which is derived in the first section of this chapter. This level of relaxation is also important in defining what a halo actually is or where its boundaries are. This question is pursuit in the second section using the tool of spherical collapse which is extended to screened modified gravity models. The last section is dedicated to the implementation of these results, i.e. how the energy quantities are to be calculated using discrete particles like from the output of an N-body simulation.

4.1 Derivation of the virialization equation

The derivation of the virialization equation presented in this section follows roughly Chandrasekhar (1981). Starting point is the collisionless Boltzmann equation already mentioned in Sec. 3.1:

$$\frac{\partial f}{\partial t} + \frac{\partial f}{\partial \mathbf{x}}\dot{\mathbf{x}} + \frac{\partial f}{\partial \dot{\mathbf{x}}}\ddot{\mathbf{x}} = 0 \,. \tag{4.1}$$

By multiplying this equation with $\dot{\mathbf{x}}$ and integrating over velocity space one obtains for the first term

$$\frac{\partial}{\partial t}\int \mathrm{d}^3\mathbf{v} v_j f = \frac{\partial (u_j n)}{\partial t} \,, \tag{4.2}$$

where n is the particle density. This means, the quantity $\mathbf{u}(\mathbf{x},t)$ can be interpreted as the mean speed of the particles inside a volume element $\mathrm{d}V$ centered at $\mathbf{x}$ at time t.

For the second term one obtains

$$\frac{\partial}{\partial x_i}\int \mathrm{d}^3\mathbf{v} v_j v_i = \frac{\partial}{\partial x_i}\int \mathrm{d}^3\mathbf{v}\left[(v_j-u_j)+u_j\right]\left[(v_i-u_i)+u_i\right] \tag{4.3}$$

$$= \frac{\partial}{\partial x_i}\left\{\frac{1}{m}P_{ji}+u_j u_i n\right\} \tag{4.4}$$

where the pressure tensor

$$P_{ji} \equiv \int \mathrm{d}^3\mathbf{v} m(v_j-u_j)(v_i-u_i)f \tag{4.5}$$

has been introduced. In the following, we consider a diagonal pressure tensor with isotropic pressure, $P_{ij}=\delta_{ij}p$.

Applying the same procedure on the third term produces

$$\int \mathrm{d}^3\mathbf{v} v_j \frac{\partial}{\partial v_i}(a_i f) = \int \mathrm{d}^3\mathbf{v}\frac{\partial}{\partial v_i}(v_j a_i f) - \int \mathrm{d}^3\mathbf{v} a_i f \delta_{ij} = -n\langle a_j\rangle \; . \tag{4.6}$$

If the force acting on the particles is independent of the particles' velocities, as it is the case for gravity, then simply $\langle a_j\rangle = a_j$.

Putting the three terms together results in

$$\frac{\partial}{\partial t}(n\mathbf{u}) + \frac{1}{m}\nabla p + \nabla\cdot(\mathbf{u}\mathbf{u}) - \mathbf{a}n = 0 \; . \tag{4.7}$$

Using the conservation of the number of particles

$$\frac{\partial n}{\partial t} + \nabla\cdot(n\mathbf{u}) = 0 \tag{4.8}$$

this identity can be rewritten as

$$\rho\frac{\mathrm{d}\mathbf{u}}{\mathrm{d}t} = -\nabla p + \rho\mathbf{a} \tag{4.9}$$

where

$$\frac{\mathrm{d}}{\mathrm{d}t} = \frac{\partial}{\partial t} + \mathbf{u}\cdot\nabla \tag{4.10}$$

is the total time derivative. This equation is the equation of motion for a fluid with flow velocity $\mathbf{u}$, pressure p and density ρ.

If only gravity acts on the fluid this can be written in the familiar form

$$\rho\frac{\mathrm{d}\mathbf{u}}{\mathrm{d}t} = -\nabla p - \rho\nabla\Phi \tag{4.11}$$

where Φ is the gravitational potential. For reasons that will be clear later on, the general form with the acceleration $\mathbf{a}$ is kept instead.

Moving on by multiplying Eq. (4.9) by $\mathbf{x}$ and integrating over a volume V one obtains on the left hand side

$$\begin{aligned}\int_V \mathrm{d}^3\mathbf{x}\,\rho\mathbf{x}\cdot\frac{\mathrm{d}\mathbf{u}}{\mathrm{d}t} &= \int_V \mathrm{d}^3\mathbf{x}\,\rho\mathbf{x}\cdot\frac{\mathrm{d}^2\mathbf{x}}{\mathrm{d}t^2}\\ &= \int_V \mathrm{d}^3\mathbf{x}\,\rho\left\{\frac{\mathrm{d}}{\mathrm{d}t}\left(\mathbf{x}\cdot\frac{\mathrm{d}\mathbf{x}}{\mathrm{d}t}\right)-\left(\frac{\mathrm{d}\mathbf{x}}{\mathrm{d}t}\right)^2\right\}\\ &= \int_V \mathrm{d}^3\mathbf{x}\,\rho\left\{\frac{\mathrm{d}}{\mathrm{d}t}\left(\mathbf{x}\cdot\frac{\mathrm{d}\mathbf{x}}{\mathrm{d}t}\right)-\mathbf{u}^2\right\} \qquad (4.12)\end{aligned}$$

and on the right hand side

$$\int_V \mathrm{d}^3\mathbf{x}\,\{\rho\mathbf{x}\cdot\mathbf{a}-\mathbf{x}\cdot\nabla p\} = W-\int_V \mathrm{d}^3\mathbf{x}\,\{\nabla\cdot(\mathbf{x}p)-p\nabla\cdot\mathbf{x}\} \qquad (4.13)$$

$$= W-\int_S \mathrm{d}\mathbf{S}\cdot(\mathbf{x}p)+3\int_V \mathrm{d}^3\mathbf{x}\,p \qquad (4.14)$$

respectively.

In (4.13) the relation

$$W=\int_V \mathrm{d}^3\mathbf{x}\,\rho\mathbf{x}\cdot\mathbf{a} \qquad (4.15)$$

was used. The implementation of the virialization criterion will play a big role for the results. Therefore, the equality of W as given in Eq. (4.15) and the maybe more common form of the gravitational potential energy of a massive body with volume V given by

$$\tilde{W}=-\frac{G}{2}\iint_V \mathrm{d}^3\mathbf{x}\,\mathrm{d}^3\mathbf{x}'\,\frac{\rho(\mathbf{x}')\rho(\mathbf{x})}{|\mathbf{x}-\mathbf{x}'|} \qquad (4.16)$$

will be briefly shown here:

$$\begin{aligned}W &= -\int_V \mathrm{d}^3\mathbf{x}\,\rho(\mathbf{x})x_i\frac{\partial\phi}{\partial x_i}\\ &= G\int_V \mathrm{d}^3\mathbf{x}\,\rho(\mathbf{x})x_i\frac{\partial}{\partial x_i}\int_V \mathrm{d}^3\mathbf{x}'\,\frac{\rho(\mathbf{x}')}{|\mathbf{x}-\mathbf{x}'|}\\ &= -G\iint_V \mathrm{d}^3\mathbf{x}\,\mathrm{d}^3\mathbf{x}'\,\rho(\mathbf{x})\rho(\mathbf{x}')\frac{x^i(x_i-x_i')}{|\mathbf{x}-\mathbf{x}'|^3}\\ &= -\frac{G}{2}\iint_V \mathrm{d}^3\mathbf{x}\,\mathrm{d}^3\mathbf{x}'\,\frac{\rho(\mathbf{x})\rho(\mathbf{x}')}{|\mathbf{x}-\mathbf{x}'|^3}\left[x^i(x_i-x_i')+x'^i(x_i'-x_i)\right] \qquad (4.17)\end{aligned}$$

$$= -\frac{G}{2} \iint_V \mathrm{d}^3\mathbf{x}\, \mathrm{d}^3\mathbf{x}' \, \frac{\rho(\mathbf{x})\rho(\mathbf{x}')}{|\mathbf{x}-\mathbf{x}'|^3} \left[(x_i - x_i')(x^i - x'^i)\right]$$
$$= \tilde{W}$$

where in the first line the relation $\mathbf{a} = -\nabla\Phi$ was used and in Eq. (4.17) an identical integral, with the variables of integration $\mathbf{x}$ and $\mathbf{x}'$ swapped, was added.

Considering now a coordinate system moving with the center of mass of the object ($\mathbf{u} = \int \rho\dot{\mathbf{x}} = 0$), the term in Eq. (4.12) often labeled (e.g. in fluid mechanics) as "kinetic energy" (Chandrasekhar, 1981) disappears. Instead the otherwise named "internal energy" plays a crucial role and is named "kinetic energy". Inserting the definition of the pressure tensor above and assuming isotropy, this term can be written as

$$T \equiv \frac{3}{2} \int_V \mathrm{d}^3\mathbf{x}\, p = \frac{1}{2} \int_V \mathrm{d}^3\mathbf{x}\, \rho(\mathbf{v}\,(\mathbf{x}) - \mathbf{u})^2 \ . \tag{4.18}$$

Instead of pressure, one speaks sometimes about the velocity dispersion $\sigma^2 \equiv p$ and in the case of isotropy $\sigma^2/3 = \sigma_x^2 = \sigma_y^2 = \sigma_z^2$.

Going back to the left hand side of Eq. (4.11), the first term of Eq. (4.12) can be rewritten:

$$\int_V \mathrm{d}^3\mathbf{x}\, \rho \frac{\mathrm{d}}{\mathrm{d}t}\left(\mathbf{x}\cdot\frac{\mathrm{d}\mathbf{x}}{\mathrm{d}t}\right) = \frac{1}{2}\int_V \mathrm{d}^3\mathbf{x}\, \rho \frac{\mathrm{d}^2}{\mathrm{d}t^2}\left(\mathbf{x}^2\right) \tag{4.19}$$
$$= \frac{1}{2}\frac{\mathrm{d}^2 I}{\mathrm{d}t^2} \ , \tag{4.20}$$

where the moment of inertia

$$I \equiv \int_V \mathrm{d}^3\mathbf{x}\, \rho\mathbf{x}^2 \tag{4.21}$$

has been introduced.

The remaining term of Eq. (4.14) can be identified with the surface pressure term

$$E_S = \int_S \mathrm{d}\mathbf{S}\cdot(\mathbf{x}p) \tag{4.22}$$

which is zero for a halo positioned in empty space (Shaw et al., 2006).

Collecting all the terms, that is Eqs. (4.15), (4.18), (4.20) and (4.22), gives the well known virial equation

$$\frac{1}{2}\frac{\mathrm{d}^2 I}{\mathrm{d}t^2} = 2T + W - E_S \ . \tag{4.23}$$

A fully virialized object is defined if the left hand side is zero, leaving

$$2T - E_S = -W \ . \tag{4.24}$$

This relationship is know as the virial theorem.

4.2 Spherical collapse in standard models

Now, it is clear what virialized objects are, the next obvious question is how they form. In other words: What initial overdensity is necessary for structure formation to happen? And, what density do these structures have today?

These questions will be addressed in this section through the well-established model of spherical collapse: A spherical overdensity is placed in an expanding space in order to find out how big this overdensity is required to be in order to have a total collapse today, i.e. the radius of the object would be zero at $a = 1$. This model allows to find a rough estimate for the density contrast between the virialized structure and its surrounding.

The spherical collapse model is analytically solvable for an Einstein-de Sitter background, which will be discussed in Sec. 4.2.1. A numerical approach is necessary in order to find the development in a more complex background evolution, which is done here for ΛCDM. The code developed was implemented in Wolfram `Mathematica`®[1] and is presented in Sec. 4.2.2.

4.2.1 Einstein-de Sitter universe

For a first approximation we consider the simplest possible model: A spherical overdensity is placed in an otherwise empty Einstein-de Sitter universe ($\Omega_k = 0, \Omega_m = 1$). This overdensity will expand first – due to the expansion of space – and then collapse under the influence of its own gravity, given the overdensity was big enough. In this simplified model, the sphere will then collapse until the radius reaches zero, resulting in an infinity density of the sphere. For real systems, however, the collapse will cease at virialization (see Eq. (4.19)). This major discrepancy is due to the fact that in real systems matter is not distributed homogeneously in spherical shells and also not all the movement is in radial direction[2]. To overcome this problem, the collapse has to be halted manually when $2T = -W$ is fulfilled.

In order to study the evolution of the sphere, we consider a "sub-universe" with higher density than the surrounding universe $\Omega_m^s > \Omega_m = 1$. In this case, the sub-universe is positively curved ($\Omega_k^s < 0$) and develops according to the Friedmann equations introduced in Sec. 1.1.3 in the following way:

$$a^s(\varphi) = \frac{a_0^s}{2} \frac{\Omega_{m,0}^s}{\Omega_{m,0}^s - 1} (1 - \cos\varphi) \tag{4.25}$$

$$t^s(\varphi) = \frac{\Omega_{m,0}^s}{2H_0} \left(\Omega_{m,0}^s - 1\right)^{-3/2} (\varphi - \sin\varphi) \ . \tag{4.26}$$

The superscript ^{s} denotes the quantities related to the sub-universe, e.g. the radius of the overdensity a^s. The parameter φ goes from 0 to 2π and, hence, the radius has a maximum of

1 `www.wolfram.com/mathematica`

2 Engineer et al. (2000) introduced additional shear and angular momenta terms in the spherical collapse equations which lead to natural ceasing of the collapse.

$a^s(\pi) = a^s_{max}$ at t_{max}. At this point all the energy of the system is potential energy (W_{max}). So in general we can write

$$T = W_{max} - W \tag{4.27}$$

$$= \frac{3}{5} GM^2 \left(\frac{1}{a^s} - \frac{1}{a^s_{max}} \right) . \tag{4.28}$$

At time of virialization – denoted by t_{vir} and φ_{vir} – the condition $2T = -W$ is fulfilled leaving us with

$$a^s_{vir} = \frac{1}{2} a^s_{max} . \tag{4.29}$$

This relation is fulfilled twice in Eq. (4.25), at $\varphi = \pi/2$ and $\varphi = 3/2\pi$. A solution after the begin of collapse (at $\varphi_{ta} = \pi$) is wanted and thus $\varphi_{vir} = 3/2\pi$.

This solution can now be used to find the density relation between the density of the sphere at time of virialization and the background density:

$$\left. \frac{\rho^s}{\rho} \right|_{\varphi_{vir}} = \left. \frac{\Omega^s_{m,0} (a^s)^{-3}}{(3/2 H_0 t^s)^2} \right|_{\varphi_{vir}} = \frac{9}{8} (2 + 3\pi)^2 \approx 147 \tag{4.30}$$

Hereby, the solution of the scale factor $a(t) = a_0 (3/2 H_0 t)^{2/3}$ derived in Sec. 1.1.3 has been used.

Another number often found in literature is 178. This results can be found if the ratio $\rho^s(\varphi_{vir})/\rho^s(2\pi)$ is taken instead:

$$\Delta_c = \frac{\rho^s(\varphi_{vir})}{\rho(2\pi)} = 18\pi^2 \approx 178 \tag{4.31}$$

Both results mean the same: Structures with a density $100 - 200$ times the background density fulfill the virial theorem and are therefore gravitationally bound objects.

4.2.2 ΛCDM model

For the case including a cosmological constant Λ, the solution cannot be found analytically anymore. Therefore, the considerations in this section are geared towards finding a numerical solution. The reason for this section to be included in full length, is that the equations derived here can be used for the modified gravity cases with only slight modifications.

The equation governing a collapse of a sphere with radius R in an expanding space is (Gunn & Gott, 1972)

$$\frac{\ddot{R}}{R} = -\frac{4}{3} G \sum_i \left(\rho_i (1 + 3w_i) \right) , \tag{4.32}$$

which is basically the second Friedmann equation Eq. (1.28) without curvature.

Assuming only dark energy in a form of a cosmological constant and ordinary matter, the equation can be rewritten as

$$\begin{aligned}\frac{\ddot{R}}{R} &= -\frac{4}{3}G\left(-2\rho_\Lambda + \rho\right) \\ &= -2H_0^2\left(-2\Omega_{\Lambda,0} + \Omega_{m,0}\left(\frac{R_i}{Ra_i}\right)^3(1+\delta_i)\right) .\end{aligned} \tag{4.33}$$

In the last line the matter density in the sphere ρ has been expressed in terms of the initial overdensity δ_i and the initial radius of the sphere R_i at time $a(t) = a_i$ via

$$\rho_m = \left(\frac{R_i}{R}\right)^3(1+\delta_i)\rho_{m,0}a_i^{-3} = \left(\frac{R_i}{R}\right)^3(1+\delta_i)\rho_{c,0}\Omega_{m,0}a_i^{-3} . \tag{4.34}$$

Using the dimensionless variable $\tilde{R} \equiv Ra_i/R_i$ with the initial radius R_i at scale factor a_i Eq. (4.33) becomes

$$\frac{\ddot{\tilde{R}}}{\tilde{R}} = -\frac{H_0^2}{2}\left(-2\Omega_{\Lambda,0} + \tilde{R}^{-3}\gamma\Omega_{m,0}(1+\delta_i)\right) . \tag{4.35}$$

It is convenient for numerical calculations to use $x \equiv \ln(a)$ as time variable. Then, the equation becomes

$$H^2\frac{\mathrm{d}^2\tilde{R}}{\mathrm{d}x^2} + \left(\frac{\ddot{a}}{a} - H^2\right)\frac{\mathrm{d}\tilde{R}}{\mathrm{d}x} = -\frac{H_0}{2}\tilde{R}\left(-2\Omega_{\phi,0} + \tilde{R}^{-3}\Omega_{m,0}(1+\delta_i)\right) , \tag{4.36}$$

which is the differential equation as implemented in the `Mathematica`® code.

The boundary conditions to solve this equations are:

1. $R\big|_{a_i} = R_i$. Therefore, $\tilde{R}\Big|_{a_i} = a_i$
2. $\dot{R}\big|_{a_i} = H\big|_{a_i}R_i$. Consequently, $\frac{\mathrm{d}\tilde{R}}{\mathrm{d}x}\big|_{a_i} = \frac{\dot{\tilde{R}}}{H}\Big|_{a_i} = a_i$.

Note that the solution is not dependent on the initial radius R_i, which means that the evolution of the collapse does not depend on the size of the halo. The value of the initial overdensity is chosen in such a way that the collapse would happen today, at $a(t) = 1$. It is found via simple iteration through various values of δ_i.

As in the case of the simple model before, the sphere would not fully collapse, but stop the collapse when the sphere is virialized, i.e. fulfills the virial equation (4.24). A common way of finding when the sphere is virialized is by integrating the Tolman-Bondi equation (Bondi, 1947; Tolman, 1934). This was done for example by Lahav et al. (1991). The approach chosen here is focusing on the acceleration, so that the virialization criterion does not have to be altered for other forms of dark energy, that is when an additional force is acting on the sphere besides gravity.

The kinetic energy is simply given by

$$T = \int \mathrm{d}^3\mathbf{x}\frac{\rho}{2}\dot{\mathbf{x}}^2 = \frac{3}{10}M\dot{R}^2 \,. \tag{4.37}$$

Expressed in the numerical variables defined above this becomes

$$T = \frac{3}{10}\left(H\frac{a_i}{R_i}\frac{\mathrm{d}\tilde{R}}{\mathrm{d}x}\right)^2 \,. \tag{4.38}$$

The total potential energy is given by Eq. (4.15) which becomes in this application

$$W = 4\pi\int_0^R \mathrm{d}r\rho r\ddot{r} = \frac{3}{5}M\ddot{R} \,. \tag{4.39}$$

Here the assumption is made that the shells of the sphere expand in a way so that there is no shell crossing and as a result the density stays uniform. Assuming no dark energy contribution, the Newtonian gravitational potential energy or $W_N = -3/5GM^2/R$ can be recovered using $\ddot{R} = -GM/R$. With dark energy in form of a cosmological constant, however, there is an additional contribution to the Newtonian gravitational potential energy given by

$$W_\Lambda = \frac{1}{5}\Lambda R^2 \,, \tag{4.40}$$

which was – as mentioned above – used by Lahav et al. (1991)[1].

In code units Eq. (4.39) becomes:

$$W = \frac{3}{5}M\left(\frac{R_i}{a_i}\right)^2\left[\frac{\mathrm{d}\tilde{R}}{\mathrm{d}x^2} + \left(\frac{\ddot{a}}{\ddot{a}} - H^2\right)\frac{\mathrm{d}\tilde{R}}{\mathrm{d}x}\right] \,. \tag{4.41}$$

Finally, the density contrast is defined as in (4.31):

$$\Delta_c = \frac{\rho_{vir}}{\rho_{c,0}\Omega_{m,0}} = (1+\delta_i)\tilde{R}_{vir}^{-3} \tag{4.42}$$

with the density of the sphere at virialization ρ_{vir} and the critical density today $\rho_{c,0}$.

The code was tested, by replicating the results from the Einstein-de Sitter model: For an initial overdensity of $\delta_i \approx 3.316 \cdot 10^{-4}$, $\Delta_c = 177.659$ was obtained. The numerical uncertainties can explain the small discrepancy to the analytical value (4.31). Note that for this and further runs we set $a_i = 10^{-4}$ and $H_0 = 71.9\,\mathrm{kms}^{-1}\mathrm{Mpc}^{-1} \approx 1.53 \cdot 10^{-42}\,\mathrm{GeV}^{-1}$.

1 Strictly speaking the result from the integration of the Tolman-Bondi-equation differs by a factor 1/2. However, this is compensated by the relation of the kinetic to the potential energy of $W \propto R^m$ with $T = n/2W$ used in this context. See Lahav et al. (1991) and Maor & Lahav (2005) for details.

In the ΛCDM case ($\Omega_{m,0} = 0.25$, $\Omega_{\Lambda,0} = 0.75$) the result is

$$\delta_i \approx 4.250 \cdot 10^{-4} \tag{4.43}$$

$$\Delta_c \approx 380.765\ . \tag{4.44}$$

Since the universe expands faster compared to the previous case, the initial overdensity needed for a collapse is expected to be bigger. Also, the additional potential energy means that the velocities have to be higher in order for the system to be in equilibrium. Therefore, the shells have to fall further inwards to acquire the velocity and Δ_c is larger.

In order to test our method, the virialization condition

$$2T + W_N + W_\Lambda = 0 \tag{4.45}$$

used by Lahav et al. (1991) was also implemented giving the same results.

4.3 Spherical collapse in screened modified gravity

In this section the spherical collapse model is studied in the symmetron and Hu-Sawicky $f(R)$-gravity case. This simplified model can help to understand the acting of the fifth force inside clusters of galaxies without employing resource-intensive N-body simulations. Naturally, the simplification is crude since important factors as the environment of the halo or inhomogeneous density distributions are neglected. After all, this model can help testing if the definition of a halo as used in ΛCDM can be directly transferred to screened modified gravity models. Thus, the aim of this section is to analyze the density contrast value Δ_c in these models and to understand the process behind eventual deviations from the standard model.

In order to do this the code introduced in the last section was modified. That is, the Newtonian gravitational constant was replaced by an effective gravitational constant taking screening effect into account. The virialization condition does not have to be modified as the acceleration is a sum of the Newtonian acceleration and the additional acceleration due to the scalar field. Therefore, the energy of the scalar field is automatically included.

In the case of screened modified gravity models, the gravitational constant in Eq. (4.32) needs to be replaced by effective ones. Several effective constants can be introduced as there might be a different force acting on distinct matter species. In the example here, the assumption is made that the additional force only acts on ordinary matter. Consequently, equation (4.33) turns into

$$\frac{\ddot{R}}{R} = -2H_0^2 \left(-2\Omega_{\Lambda,0} + \gamma \Omega_{m,0} \left(\frac{R_i}{R a_i} \right)^3 (1 + \delta_i) \right) \tag{4.46}$$

with $\gamma = G_{eff}/G$. Note that, the value of this effective gravitational constant G_{eff} depends on the environment and hence G_{eff} is not a constant at all. Furthermore, the assumption

has been made that there is an effective cosmological constant present as it is in most chameleon-like models.

In code units, the equation of motion then reads

$$H^2 \frac{\mathrm{d}^2\tilde{R}}{\mathrm{d}x^2} + \left(\frac{\ddot{a}}{a} - H^2\right)\frac{\mathrm{d}\tilde{R}}{\mathrm{d}x} = -\frac{H_0}{2}\tilde{R}\left(-2\Omega_{\phi,0} + \gamma\tilde{R}^{-3}\Omega_{m,0}(1+\delta_i)\right) . \tag{4.47}$$

As stated in the spherical solution sections of Chapter 2, objects can be in any state between fully screened to unscreened. The difference of the effective gravitational constants of these two extreme cases is equal to $3\Delta R/R$. Therefore, we approximate γ to be of the form

$$\gamma = 1 + 2\beta^2\mathcal{T} \text{ with } \mathcal{T} \equiv \min\left(1, \frac{3\Delta R}{R}\right) . \tag{4.48}$$

Here, the same variable transformation as in Sec. 3.2.2 has been performed for the symmetron model in order to replace the model parameters (μ, M, λ) by (β, a_{ssb}, L). Notice that the same set of equations can be found in Brax et al. (2010b) where the spherical collapse in the chameleon model has been analyzed with a slightly different definition of γ.

The thin shell factor was stated in Eq. (2.27), that is

$$\frac{\Delta R}{R} = \frac{|\phi_\infty - \phi_c|}{6\beta M_{\mathrm{Pl}}\Phi} , \tag{4.49}$$

where ϕ_∞ and ϕ_c are the values of the scalar field far away and at the center of the object, respectively. The Newtonian potential of the sphere Φ in code units is simply given by

$$\Phi = \frac{R^2\rho}{6M_{\mathrm{Pl}}^2} = \frac{G a_i M_c}{\tilde{R} R_i} . \tag{4.50}$$

This introduces a dependency on the mass of the object, i.e. Δ_c and the virial radius will depend on the mass of the cluster.

In scalar-tensor theories the virialization condition has to take the energy of the scalar field into account as well. Very elegant solutions are discussed in Maor & Lahav (2005) and Mota & Bruck (2004). Instead, in this implementation the particles' acceleration is used (see Eq. (4.39)) and the scalar field is considered in the equation of motion, the virialization condition used for ΛCDM needs not to be altered.

In the following the two implementations – the $f(R)$ Hu-Sawicky model and the symmetron model – are presented, which differ in the value of $|\phi_\infty - \phi_c|$. A similar implementation for a chameleon model was done by Brax et al. (2010b) and in time of writing Lombriser et al. (2013) published a work for the same $f(R)$ model including excursion sets. The spherical collapse has not been applied to the symmetron model before.

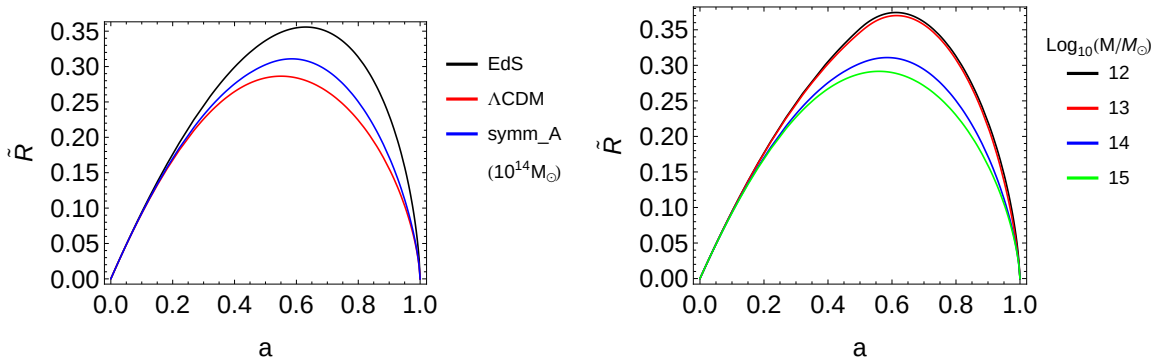

Figure 4.1: Evolution of the spherical collapse. *Left panel:* Collapse in the Einstein-de-Sitter (black line) and ΛCDM (red line) model compared to the evolution of a sphere with mass $M = 10^{14}\,M_\odot$ in the *symm_A* model. *Right panel:* Collapse in the symmetron model using the *symm_A* parameters for different masses.

4.3.1 Symmetron implementation

In the symmetron model the effective potential is unbroken far away from the sphere before the time of symmetry breaking a_{ssb}. Afterwards, the scalar field in the background settles at

$$\phi_\infty = \pm \frac{2L^2\beta\rho_{c0}\Omega_{c0}\sqrt{1-\left(\frac{a_{ssb}}{a}\right)^3}}{a^3_{ssb}M_{\rm Pl}}\,. \tag{4.51}$$

Naturally, inside the sphere the potential is also unbroken for $a < a_{ssb}$ since the density is always higher there. Also afterwards, for $a > a_{ssb}$, this unbroken state inside the sphere is expected to persist for most parameters and sphere masses, meaning $\phi_c = 0$. If, however, the density inside the sphere drops due to the expansion of space below the threshold value of $\rho_{ssb} = \Omega_{m0}\rho_{c0}a^{-3}_{ssb}$, then the effective potential inside the sphere can brake.

Hence, the scalar field value inside the sphere is given by

$$\phi_c = \begin{cases} 0 & \text{if } \rho > \rho_{ssb} \\ \pm\dfrac{2L^2\beta\sqrt{\rho_{c0}\Omega_{m0}(\rho_{c0}\Omega_{m0}-a^3_{ssb}\rho)}}{a^3_{ssb}M_{\rm Pl}} & \text{otherwise.} \end{cases} \tag{4.52}$$

Note, that ϕ_c as well as ϕ_∞ both possess two solutions after symmetry breaking. This is because for a local density $\rho > \rho_{ssb}$ there is a potential minimum in the positive and negative ϕ-region (see Fig. 2.2 in Sec. 2.2). As shown by Llinares & Mota (2013a) although it is indeed possible for the scalar field to settle in both minima, only the solution with the same sign as the background is stable. If, for example, ϕ_∞ takes a positive value after a_{ssb}, only the positive solution of ϕ_c is stable. Therefore, we decided to force $\phi_c \geq 0$ and $\phi_\infty \geq 0$ for all the solution discussed at first. In the last part of this section, we also discuss briefly the possibility when $\phi_\infty \geq 0$ and $\phi_c \leq 0$.

In the first, the stable, case the thin shell factor given by Eq. (4.49) is zero for $a < a_{ssb}$ and can afterwards take a maximum value of

$$\frac{\Delta R}{R} = \frac{8L^2\pi R\rho_{c0}\Omega_{m0}\sqrt{1-\left(\frac{a_{ssb}}{a}\right)^3}}{3a_{ssb}^3 M_c} \,, \tag{4.53}$$

if $\phi_c = 0$ and $a > a_{ssb}$.

Fig. 4.1 shows the development of the spherical collapse for the Einstein-de-Sitter, ΛCDM and symmetron models, including different masses in the latter. As expected, the collapse in the symmetron case is mass-dependent and thus the resulting quantity Δ_c should be, too. The next step is to analyze the behavior of Δ_c with the help of the development of the virialization time a_{vir}, the initial overdensity δ_i, the evolution of the kinetic and potential energy and – maybe most importantly – the fifth force which is responsible for the deviation from ΛCDM.

To quantify the fifth force, the formerly introduced $\mathcal{T}$ is used. $\mathcal{T}$ takes values from 0 to 1 and can be understood as the normalized γ parameter. Fig. 4.2 shows $\mathcal{T}$ as a function of the expansion factor for the parameter sets *symm_A*–*D*[1]. Since *symm_C* is the only parameter set where β takes a value of 2 instead of 1, the gravitational force in this model can be amplified by a factor of 9 instead of only three. Visually, the four panels of Fig. 4.2 can be split into two categories: The first column with *symm_A*, *C* and the second column with *symm_B*, *D*. In the first column, for the smaller masses $\mathcal{T}$ rises to its maximum right after the time of symmetry breaking a_{ssb} to then – at some point – decline monotonically. Note that the evolution of the fifth force after a_{ssb} depends also on the mass of the sphere: For the smallest spheres the fifth force is acting with full strength on the system for (nearly) the whole collapse (the virialization times are marked with a round dot on each curve in Fig. 4.2). Consequently, the collapse evolution for very small spheres is identical to a ΛCDM collapse with an effective gravitational constant of $G_{eff} = (1+\beta^2)G$. For the bigger spheres, $\mathcal{T}$ and, hence, also $\gamma \equiv G_{eff}/G$, might not reach its theoretical maximum at all as the density of the sphere at a_{ssb} is already at a point where the self-screening mechanism works. Hence, we expect the standard ΛCDM collapse to be a limit for very high masses. The second column of Fig. 4.2 – which contains the evolution of $\mathcal{T}$ for *symm_B* and *symm_D* – shows an entirely different behavior: After the time of symmetry breaking ($a_{ssb} = 1/3, 1/4$ for *symm_B* and *symm_D*, respectively) γ reaches for all masses its possible maximum, followed shortly after by a rapid decline of the fifth force. Afterwards, for the *symm_D* model, the value of $\mathcal{T}$ rises again, in some cases as high as its maximal possible value, to then decline in the same fashion as can be observed in the *symm_A* and *symm_C* case. In the *symm_B* case no second incline of the fifth force happens. Instead, $\mathcal{T}$ declines monotonically.

These two categories of the various sphere evolutions are due to the two possible regimes of ϕ_c stated in Eq. (4.52): Either the density ρ is always greater than ρ_{ssb} resulting in a constant $\phi_c = 0$ or the effective potential inside the sphere is also broken resulting in a smaller thin shell factor. These two regimes can be observed in Fig. 4.3, where the matter density inside

1 See Table 3.1 in Sec. 3.3 for a summary of the model parameters.

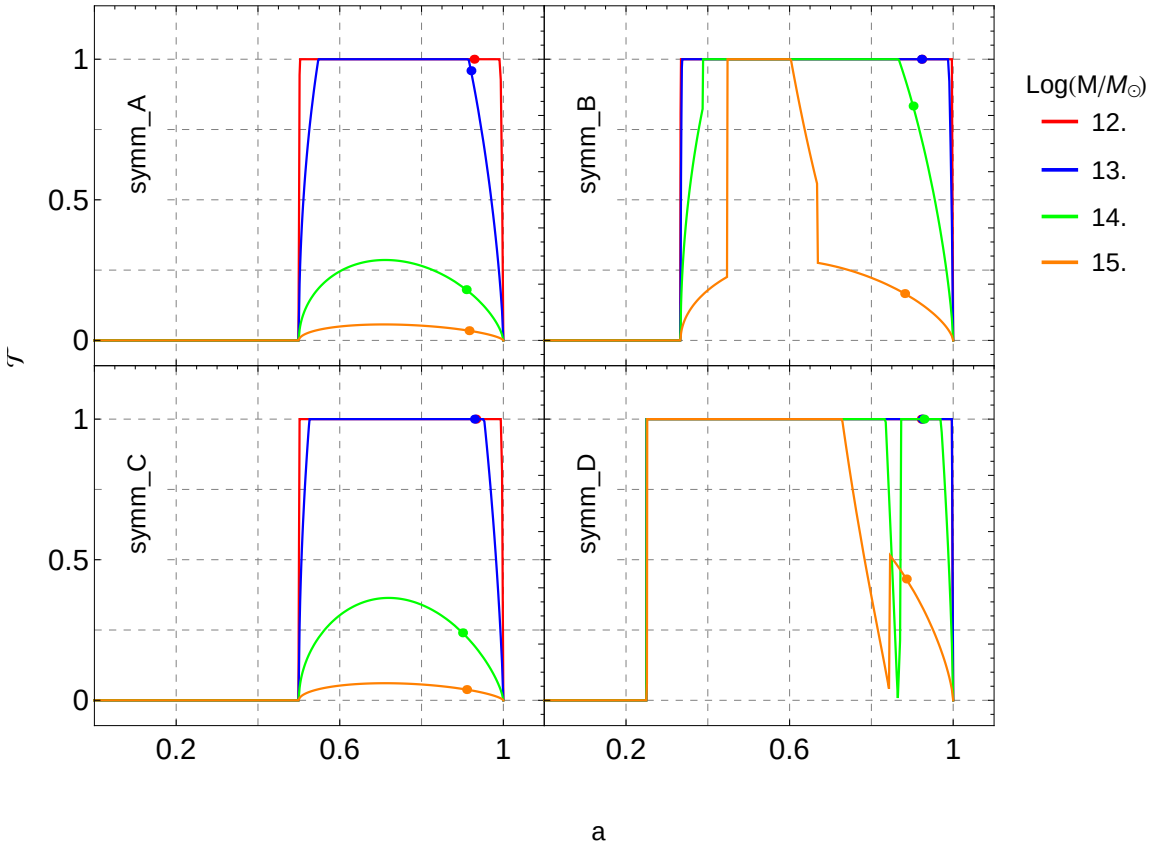

Figure 4.2: $\mathcal{T}$, which is defined in Eq. (4.48) and measures the strength of the effective gravitational constant G_{eff}, as a function of scale factor. As an example, four masses for each symmetron model are shown. The points mark the time of virialization for each mass. The different values for $a_{ssb} = (1/2, 1/3, 1/2, 1/4)$ for *symm_A–D* explains the different positions of the sharp rise of the fifth force.

the sphere is plotted against time. In the *symm_A* and *symm_C*case (left column) $\rho \gtrsim \rho_{ssb}$ for all shown masses, meaning all solutions are member of the first category. In the *symm_D* case, on the other hand, the situation is quite the opposite as for all the solutions exist a time where $\rho < \rho_{ssb}$. For the other parameter sets – *symm_B* – the affiliation depends on the mass of the sphere. These two categories have to be remembered when interpreting the following results.

Fig. 4.4 shows the initial overdensity needed for a collapse today, δ_i, the density contrast as defined in Eq. (4.42), Δ_c, the deviation of the virial radius and the time of virialization as a function of the mass. For bigger masses, when the self-screening works more effectively, the values approach the ΛCDM result as expected. Also, not surprising is for smaller masses, when the self-screening is not yet active, the earlier the symmetry breaking happens, the

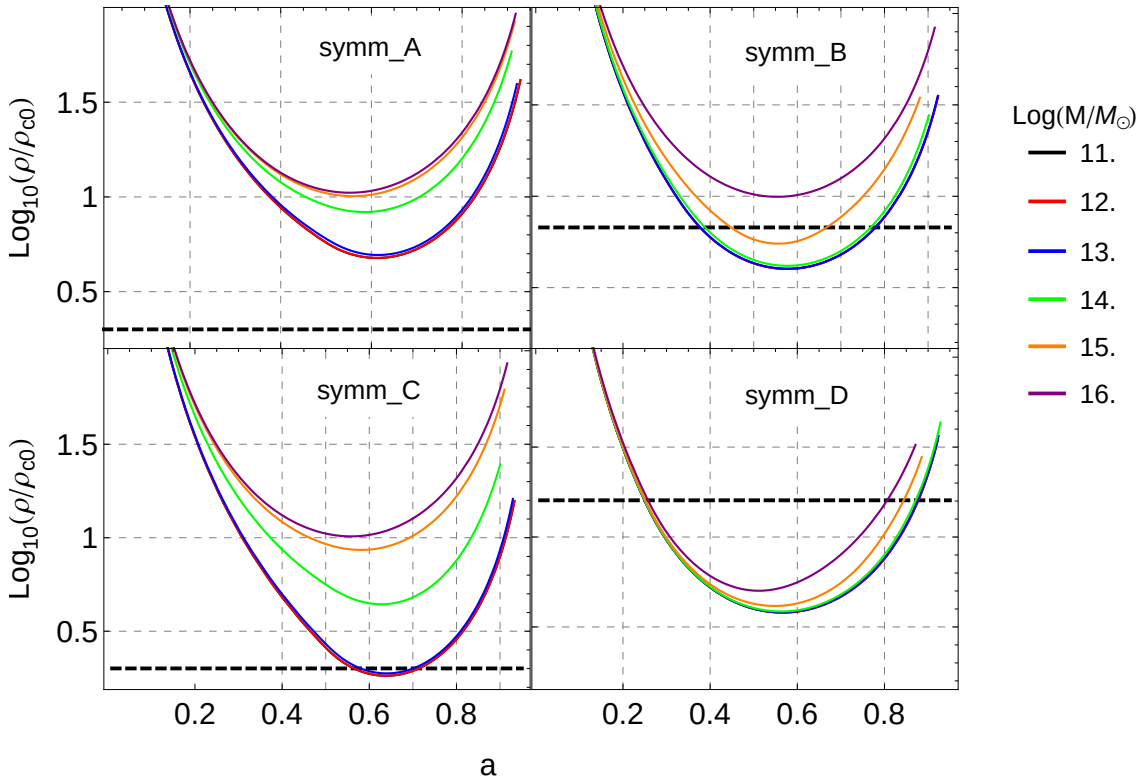

Figure 4.3: Evolution of the matter density inside the sphere for the parameter sets *symm_A–D*. In each panel the solution is shown for spheres with masses $\log(M/M_\odot) = (11,12,13,14,15,16)$ (black, red, blue, green, orange, purple) until the virialization time a_{vir}. In addition, the ρ_{ssb} threshold is marked for each model with a black dashed line.

bigger is the resulting deviation of δ_i from Λ since the fifth force has more or less time to act on the object. The results suggests the existence of a mass threshold below which the measured quantity stays constant. This can be explained via the phenomenon mentioned before: Too small masses will never reach the density to be screened and hence the collapse is independent of the initial radius. In addition, the increase of the coupling parameter β seems have an enormous impact. Comparing the *symm_C* results with the ones for *symm_A*, it can be seen that the deviation from the ΛCDM value is roughly doubled. Not shown are the results with an increased L. For them the curve seems to be shifted to higher masses, which is reasonable since the impact of the fifth force is strongest at length scales $\sim L$.

Between the two mass regimes mentioned where the values are constant or approaching a constant value, two features in the Δ_c versus mass plot are striking: Firstly, a local maximum for which is especially present in the *symm_D* case and, secondly, a local minimum that

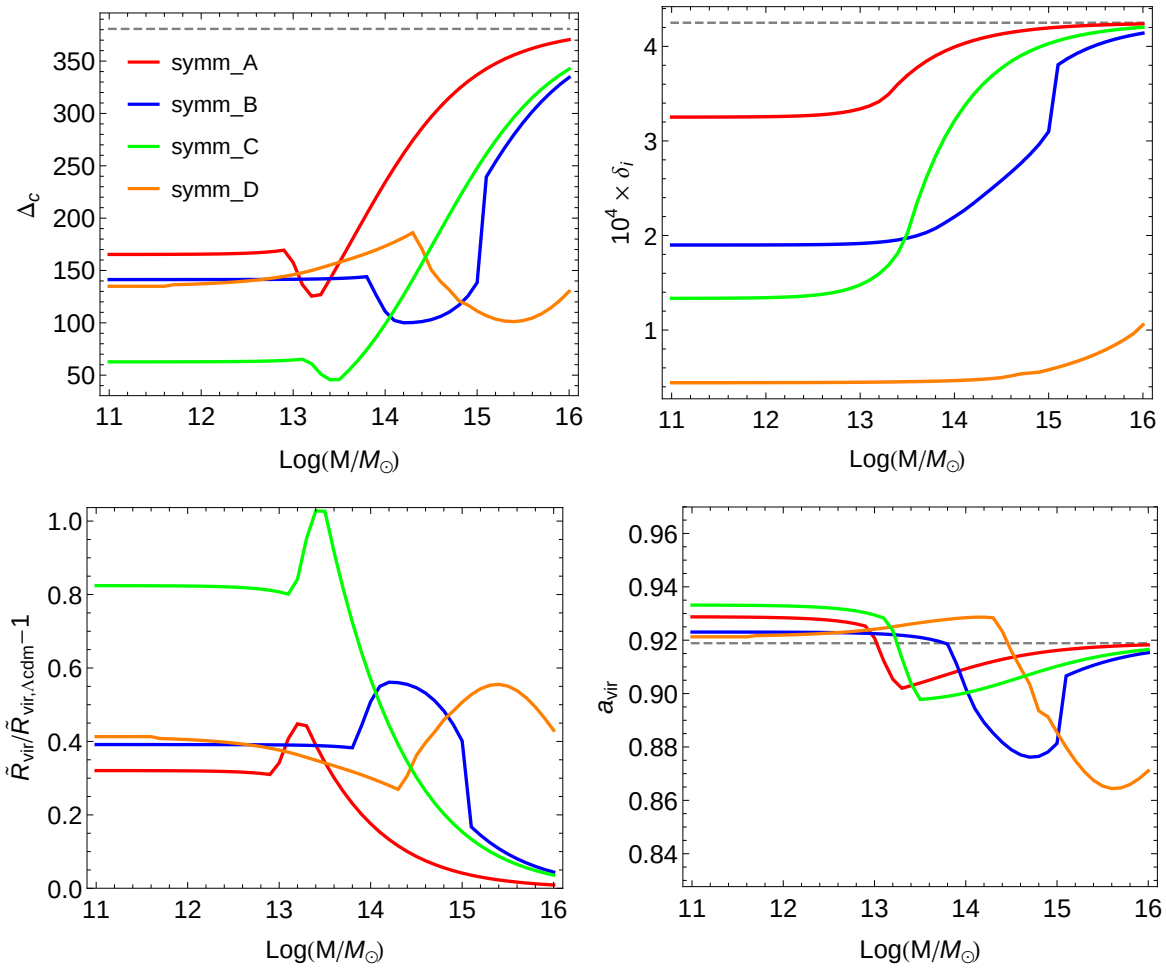

Figure 4.4: Δ_c (*top left*), δ_i (*top right*), the relative deviation of the virial radius compared to ΛCDM (*bottom left*) and the time of virialization a_{vir} (*bottom right*) are shown for the symmetron model. The *symm_A,B,C,D* are shown in red, blue, green and orange, respectively. The gray dotted line shows the ΛCDM value as a comparison.

marks the point of maximum deviation from ΛCDM. The existence for these two features is explained in the following in detail. The knowledge obtained from the simplified spherical collapse model about the evolution of a sphere can later on be used for the analysis and interpretation of the N-body results.

The reason for the characteristic mass range with the most deviation from the ΛCDM virial radius and therefore also Δ_c, i.e. between the low mass and the high mass regime mentioned, can be seen by studying the time of virialization a_{vir}. This point in time seems to be always relatively close to the ΛCDM value (with the constant shift for small masses), except in a certain mass range where the virialization occurs earlier. Consequently, the sphere has not reached the density of the ΛCDM case yet and Δ_c differs the most.

The dependency of the virialization time on the model parameters is more complicated, as

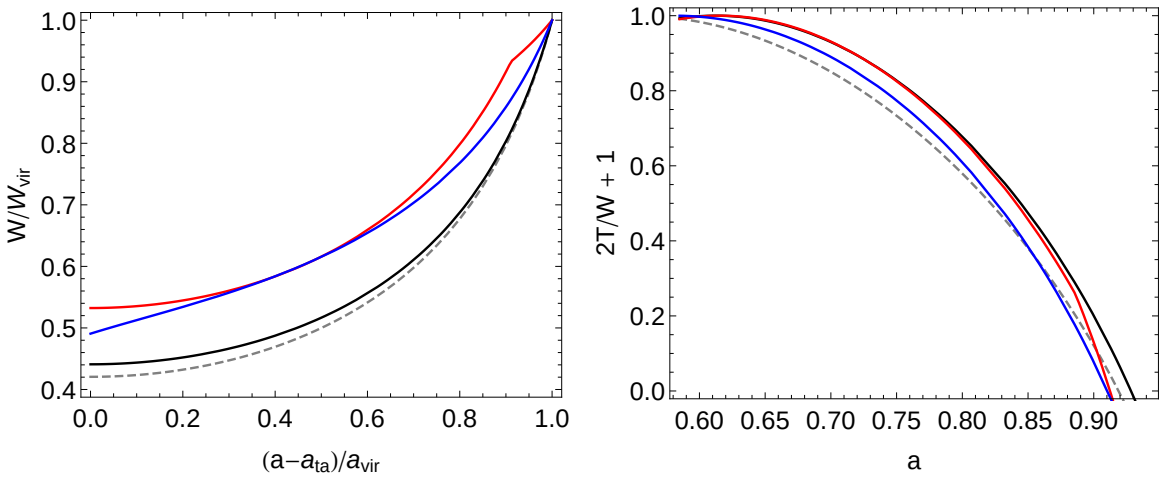

Figure 4.5: Evolution of the energy quantities in the *symm_A* model. The color codes are indicate the mass of the spheres, with $\log(M/M_\odot) = (12.1, 13.1, 14.1)$ (black, red and blue line, respectively). *Left panel:* Potential energy relative to its value at virialization W_{vir} between the turnaround a_{ta} and virialization point a_{vir}. *Right panel:* $2T/W + 1$ – which[1] is zero at virialization – versus a.

many dependencies have to be considered. It is clear, however, that from the turn around point the kinetic energy T is a positive function and steady increasing from zero whereas the potential energy W is a negative function with a behavior that influences the outcome of a_{vir}. In order to understand why the time of virialization has this characteristic minimum, we analyze the evolution of three distinct sphere masses in the *symm_A* case. The masses of the spheres has been chosen in way that one mass is in the point of maximum deviation ($M = 10^{13.1} M_\odot$), while the other two are smaller ($M = 10^{12.1} M_\odot$) and bigger ($M = 10^{14.1} M_\odot$). The analysis is carried out for the parameter set *symm_A* as in this case $\rho > \rho_{ssb}$ for all considered masses. Hence, in this case $\phi_c = 0$ for the whole collapse and matters are simplified.

The evolution of the kinetic and potential energies of the spheres is shown in Fig. 4.5. In the left panel, the potential energy is displayed in the time span of interest – between the turn around point a_{ta} and the point of virialization a_{vir}. In the fully screened ($G_{eff} \approx G$, gray dotted curve) or totally unscreened ($G_{eff} \approx (1+\beta^2)G$, blue curve) cases, W is a steady decreasing function of the scale factor. In opposition, for a changing fifth force over time the energy of the scalar field is increasing (red and blue curve). The crucial difference between the solutions for $M_c = 10^{13.1}\, M_\odot$ and $M_c = 10^{14.1}\, M_\odot$ (red and blue curve in Fig. 4.5, respectively) is clear by comparing the evolution of the fifth force in both cases in Fig. 4.2 (top left panel): For the heavier sphere γ is a smooth function between a_{ta} and a_{vir} but for the lighter a break between the decreasing and fully unscreened regime exists additionally. The transition between the two regimes leads to flattening of the $W(a)$ curve in the time shortly before a_{vir}. The "delay" means T reaches faster the threshold of virialization, which

is best seen in terms of $2T/W + 1$[1], a quantity that is zero for virialized objects. The right panel of Fig. 4.5 shows $2T/W + 1$ against a and the decrease proceeds in a similar way for all displayed masses but $M_c = 10^{13.1}\,M_\odot$ where instead a double slope behavior is observable. Due to the steep tail the lower value of a_{vir} occurs and therefore the characteristic extremum in Δ_c arises.

The other feature in the Δ_c versus mass plot (Fig. 4.4, top left panel) concerns the local maximum for masses slightly smaller than the just discussed ones. It only exists if the potential is broken also inside the sphere, i.e. if ϕ_c is different from 0 at some stage of the collapse. As discussed before, this results in a smaller thin shell factor and, consequently, in a weaker additional force and in less deviation from ΛCDM. So is the maximum most clearly present for *symm_D*, where the densities are also much lower than ρ_{ssb} (compare with Fig. 4.3). For *symm_A* and *symm_C* the feature is non-existent as $\rho \gtrsim \rho_{ssb}$ for all times. Located between these cases is *symm_B* since here $\rho \gtrsim \rho_{ssb}$ some masses existent valid.

The second solution for the thin shell factor was already mentioned in the beginning of this section and will be briefly discussed here. The scalar field inside the sphere can settle at the other minimum than the outside solution, resulting in opposite signs of ϕ_c and ϕ_∞. This leads to a overall bigger thin-shell factor and therefore to a higher additional force. The existence of these two different values of the scalar fields in N-body simulations has been shown by Llinares & Mota (2013a) by including time derivatives of the field, that is, not assuming the quasi-static approximation. There are still a lot of open questions about the behavior of the scalar field

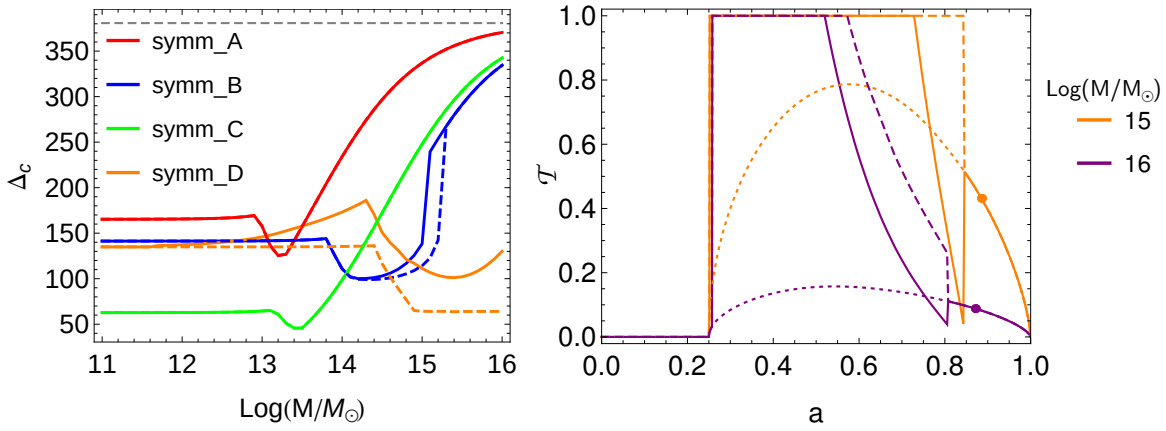

Figure 4.6: Comparison between the solution with a the interior (ϕ_c) and the background solution (ϕ_∞) having opposite signs (dashed lines), and the solution showed previously (solid lines). *Left panel:* Δ_c versus mass of sphere. *Right panel:* $\mathcal{T}$ as a function of time using the *symm_D* solution for two different masses parameters shown previously in Fig. 4.2. In this panel is in addition to the dashed curves unnatural solutions with a forced $\phi_c = 0$ added with dotted curves.

1 $\beta_{vir} \equiv (2T - E_s)/W + 1$ is the virialization parameter and is properly introduced in Sec. 4.4.

value. Thus, this second solution is merely shown here as a mathematical possibility in order to help understanding better the symmetron breaking process. Fig. 4.6 shows the results obtained through the second possible solution – that is ϕ_∞ and ϕ_c possessing different signs – with dashed lines. As expected, this solution shows greater deviation from ΛCDM for the sphere evolution where $\rho < \rho_{assb}$ occurs. The simple explanation for that behavior is the even greater thin-shell factor than in the unbroken interior potential. For bigger spheres a sudden restoring of the symmetry can happen, which leads to a sudden decrease (as opposed to a sudden increase for the previously discussed solution) in $\mathcal{T}$. For illustrative purpose a solution with a forced $\phi_c = 0$ was added to the right panel of Fig. 4.6. When the three lines meet, the symmetry inside the sphere is restored, that is $\rho > \rho_{ssb}$.

4.3.2 $f(R)$ implementation

The spherical collapse implementation and results in $f(R)$-gravity is very similar to the one discussed in the symmetron model and will therefore be only presented in brief.

The thin shell factor depends on the value of the scalar field inside and far away from the sphere. Therefore, Eq. (2.72) is simply applied for $\Delta_\rho = \Omega_{m,0} a^{-3}$ in order to obtain ϕ_∞ and $\Delta_\rho = \rho/\rho_{c,0} = 3M_c/4\rho_{c,0}\pi R_c^3$ for the center of the halo. This leaves the thin shell factor as

$$\begin{aligned}\frac{\Delta R}{R} =& \frac{|\phi_\infty - \phi_c|}{6\beta M_{\mathrm{Pl}}\Phi} \\ =& \frac{|1 - f_{R0}|}{12\beta^2\Phi}\left[\frac{\Omega_{m,0} + 4\Omega_{\Lambda,0}}{\rho/\rho_{c,0} - \Omega_{m,0}a^{-3}}\right]^{n+1} .\end{aligned} \tag{4.54}$$

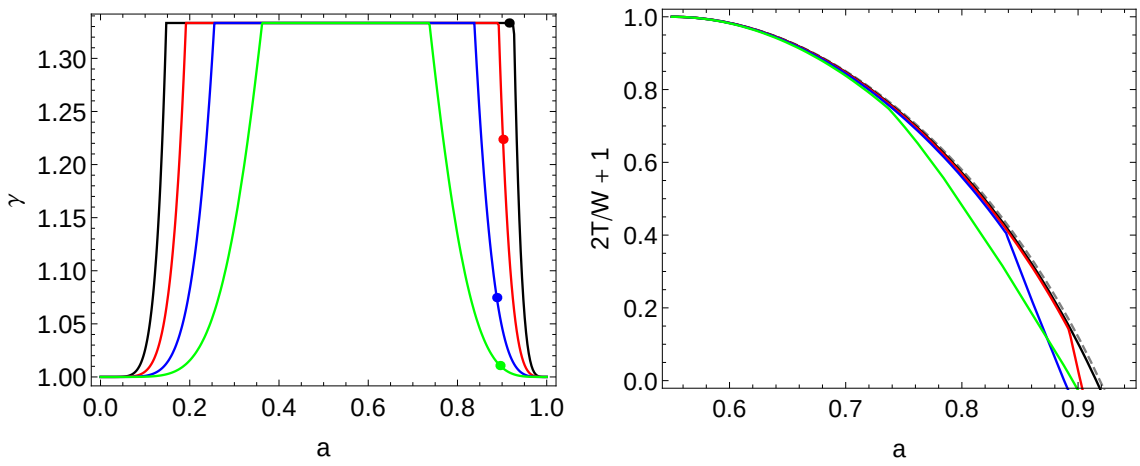

Figure 4.7: γ (*left*) and $\beta_{vir} = 2T/W + 1$ (*right*) for the $f(R)$ model with $n = 1$, $|f_{R0} - 1| = 10^{-4}$ (*fofr4*). The black, red, blue and green curve denote the mass of the sphere as 10^{12}, 10^{13}, 10^{14} and $10^{15} M_\odot$, respectively. A value of $\beta_{vir} = 0$ defines the time of virialization a_{vir} and is marked with a dot on the corresponding curve in the left panel.

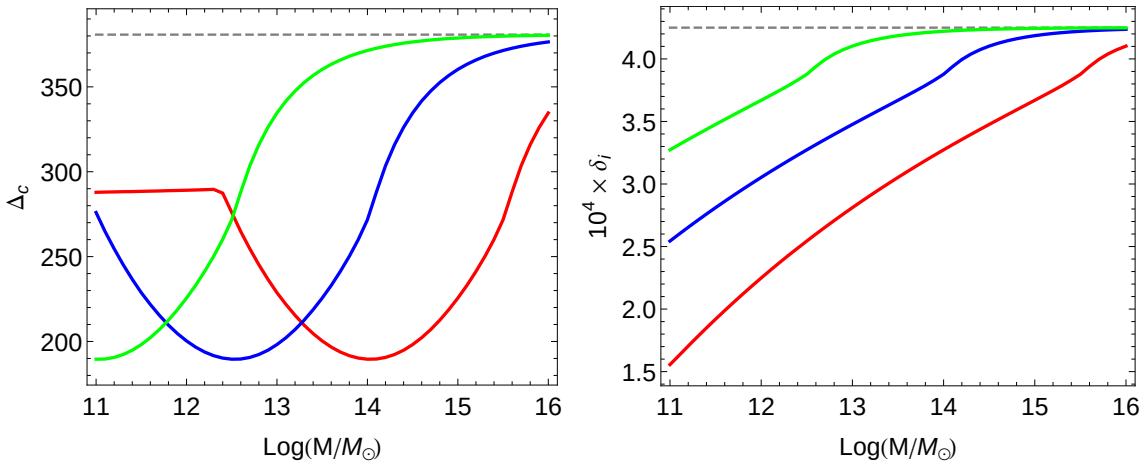

Figure 4.8: Δ_c (*left*) and δ_i (*right*) for the $f(R)$ model. For all curves $n = 1$, but $|f_{R0} - 1| = (10^{-4}, 10^{-5}, 10^{-6})$ (*fofr4*, *fofr5*, *fofr6*) are shown in red, blue and green, respectively. The gray dashed line shows the ΛCDM value as a comparison.

Again, $\Phi = R^2\rho/6M_{\rm Pl}^2$ is the Newtonian potential of the sphere.

The results, in the form of Δ_c and δ_i plotted against the halo mass, are shown in Fig. 4.8 and the evolution of a sample collapse in form of β_{vir} and γ are shown in Fig. 4.7. The same features as in the symmetron case can be spotted and will not be discussed again in detail: *(i)* Approach of the ΛCDM value with increasing mass as the screening has a bigger effect, *(ii)* constant value for smaller halos and *(iii)* the characteristic minima in Δ_c in the intermediate regime. However, the local maximum that was present for *symm_B–D* does not exist as the field value in the interior of the sphere stays small and does not change dramatically as it is possible in the symmetron mechanism. Consequently, the $f(R)$ solutions resemble more the solutions obtained for the symmetron model without a symmetry breaking inside the sphere as in the *symm_A* case. Also, the feature *(ii)* is not exactly the same but altered in two ways: First, the constant level in Δ_c is closer to the ΛCDM level as β has a lower value and secondly the constant limit does not exist for δ_i at all. This is due to the fact that there is no sudden switching on of the fifth force but instead a more continuous evolution.

4.3.3 Conclusions of the spherical collapse model

In this section the spherical collapse model was studied numerically for the symmetron and the Hu-Sawicky $f(R)$ model. The computer code produced for this purpose was tested reproducing the analytical results derived for a flat Einstein-de-Sitter universe and obtaining the ΛCDM values for two different virialization criteria. The main resulting quantity of interest is the overdensity parameter Δ_c as it is important for calculating halo properties and therefore relevant if these are compared using different theories. In addition, the simple model allows an understanding of the screening mechanism and its effect on halos. This qualitative behavior was found to be in agreement with Brax et al. (2010b) and Wintergerst &

Pettorino (2010) where the spherical collapse model has been analyzed for similar underlying models.

The results show a possible major deviation from the ΛCDM Δ_c value which may cause various definitions of where the boundaries of a halo lies. To correct for this effect a proper treatment is needed in finding halo attributes, which would be possible to implement e.g. in the halo finding code. Although the problem is known, until now, no such code exist (Knebe et al., 2013). When interpreting these results, it is, however, important to keep in mind that major simplifications have been made:

(i) No shell crossing: As there is no shell crossing allowed, the matter density inside the sphere stays constant per definition. This is certainly not the case in a dynamical model as pointed out by Brax et al. (2010b) because of the smooth scalar field solution and the arising effects in the shell region. Engineer et al. (2000) and Shaw & Mota (2008) constructed semi-analytical extensions to the spherical collapse model which take the effects of shell-crossing into account and would be worth including.

(ii) Homogeneous initial density and no pressure: A realistic model would result in a power-law density profile as known from simulations and observations (Ludlow et al., 2013; Okabe et al., 2013). This will have various implications on the fifth force, e.g. lead to a screened and unscreened region (Lombriser et al., 2012). A consequence of this is that there is no tangential motions and not local perturbations in the sphere.

(iii) No environmental screening: The neglection of the environmental screening, i.e. the vanishing of the fifth force due to the location of the halo in a denser surrounding, e.g. inside a filament, is maybe a very crude approximation especially for the smaller masses, as the environment can have a major effect on a halo (Winther et al., 2011). A more detailed analysis using an excursion set approach was done by Li & Efstathiou (2012) and Lombriser et al. (2013).

Therefore, the results obtained in this section give a good guideline for further analysis and allow to understand the process of halo formation in screened modified gravity cases in a qualitative way but should not be over-interpreted. Also, worth noticing is that a change of Δ_c does not lead to an equally strong change in the halo mass since the density of real dark matter halos falls off with $\propto r^{-3}$ in the outskirts. Hence, we expect only second order corrections to the halo properties and leave a detailed study for future work.

4.4 Virialization state in N-body simulations

In the first section of this Chapter, the virial theorem was derived. It was applied to the spherical collapse model where the matter density is given by a simple function. In this section, the question about how to define an object as virialized in N-body simulations, that is when dealing with discrete particles, is studied.

First, let us recall what a virialized object is mathematically: As was shown in Sec. 4.1, a virialized object fulfills the condition

$$2T - E_S = -W \ . \tag{4.55}$$

Therefore, the potential energy W, the surface term E_S and the kinetic energy T have to be calculated for each halo of the simulation output.

In order to measure the degree of virialization, the virialization parameter β_{vir} can be introduced similarly to Shaw et al. (2006):

$$\beta_{vir} \equiv \frac{2T - E_s}{W} + 1 \ . \tag{4.56}$$

This means, one can define a halo being sufficiently relaxed or virialized if $|\beta_{vir}|$ is smaller than a certain threshold.

The question now is how to implement the expressions for the energy quantities. Clearly, the terms derived in Sec. 4.1 cannot be used directly as it was done for the spherical collapse model in Sec. 4.2 since N-body simulations constist out of discrete particles. Therefore, the next three subsections are devoted to the answer of that question starting with the kinetic energy, then the potential energy and last the surface term.

The kinetic energy

The kinetic energy is the most straightforward one, as it is given by

$$T = \frac{1}{2} \sum_{i \in \mathcal{H}} m_i |\mathbf{v_i} - \mathbf{v}_\mathcal{H}|^2 \tag{4.57}$$

with the velocity of particle i, $\mathbf{v_i}$, taken relative to the halo velocity $\mathbf{v}_\mathcal{H}$. This equation is the discretization (4.18) with the halo velocity

$$\mathbf{v}_\mathcal{H} = \frac{1}{M_\mathcal{H} N_\mathcal{H}} \sum_{i \in \mathcal{H}} m_i \mathbf{v_i} \ . \tag{4.58}$$

In the case of particles with equal masses this relation becomes simply

$$\mathbf{v}_\mathcal{H} = \frac{1}{N_\mathcal{H}} \sum_{i \in \mathcal{H}} \mathbf{v_i} \tag{4.59}$$

where $N_\mathcal{H}$ is the number of particles in the halo.

For completeness it is repeated, that the quantity of velocity dispersion σ may be introduced[1] in this context with

$$\sigma^2_\mathcal{H} = \frac{1}{N_\mathcal{H}} \sum_{i \in \mathcal{H}} |\mathbf{v_i} - \mathbf{v}_\mathcal{H}|^2 \ . \tag{4.60}$$

1 Note that this definition differs from the one made in Sec. 4.1, as this one is the velocity dispersion of the halo $\mathcal{H}$ and the previous one the three-dimensional velocity dispersion of a volume element $\mathrm{d}V$.

The potential energy

The potential energy W can be calculated in two different ways, given by (4.15) and (4.16):

$$W = \int_V \mathrm{d}^3\mathbf{x}\, \rho\mathbf{x} \cdot \mathbf{a}$$
$$\tilde{W} = -\frac{G}{2} \iint_V \mathrm{d}^3\mathbf{x}\, \mathrm{d}^3\mathbf{x}'\, \frac{\rho(\mathbf{x}'\rho(x))}{|\mathbf{x} - \mathbf{x}'|}\ .$$

This leaves in general three possibilities of calculating the potential energy of a halo $\mathcal{H}$ using discrete particles:

1. Using a simple direct summation approach:

$$W_{DS} = -\frac{G}{2} \sum_{\substack{i,j \in \mathcal{H} \\ i \neq j}} \frac{m_i m_j}{\sqrt{|\mathbf{x_i} - \mathbf{x_j}|^2 + \varepsilon^2}} = \frac{1}{2} \sum_{i \in \mathcal{H}} m_i \Phi_{DS,i} \tag{4.61}$$

2. Summing over the gravitational potential at each particle position $\phi_i = \phi(\mathbf{x_i})$:

$$W_P = \sum_{i \in \mathcal{H}} \frac{m_i}{2} \Phi_i \tag{4.62}$$

   The gravitational potential at each particle's position $\Phi_i = \Phi(x)$ was obtained from the gravitational potential used by the N-body code through interpolation.

3. Utilizing the particles' acceleration instead:

$$W_a = \sum_{i \in \mathcal{H}} \frac{m_i}{2} (\mathbf{x_i} - \mathbf{x}_\mathcal{H}) \cdot \ddot{\mathbf{x}}_\mathbf{i} \tag{4.63}$$

   Here the position of the halo $\mathbf{x}_\mathcal{H}$ is inserted because of the comoving reference system.

The first possibility is very computational expensive and does not result in exactly the same value as the second one because the gravitational potential is obtained via summation of the whole box and not just the other members of the halo. Although the difference is small – especially near the center of the bigger halos, where most of the contribution comes from the other members of the halo – there is another problem, namely the normalization of the gravitational potential. This problem can be overcome by assuming that the central particle is only affected by the members of the halo and shifting the values of Φ_i by $\Delta\Phi = \Phi_{DS,0} - \Phi_0$, i.e. the difference between the gravitational potential at the central particles' position $\Phi_0 \equiv \Phi(\mathbf{x}_\mathcal{H})$ obtained directly from the N-body simulation and the value calculated through direct summation over the members of the halo.

This normalization technique, which can potentially avoid the computationally expensive task of obtaining the gravitational through direct summation for each particle, is shown in Fig. 4.9 in the form of Φ_i, $\Phi_{DS,i}$ and $\Phi_i + \Delta\Phi$. One can clearly see that although $\Phi_{DS,i}$ and $\Phi_i + \Delta\Phi$ are normalized in the center of the halo, they do not agree on the outskirts. This

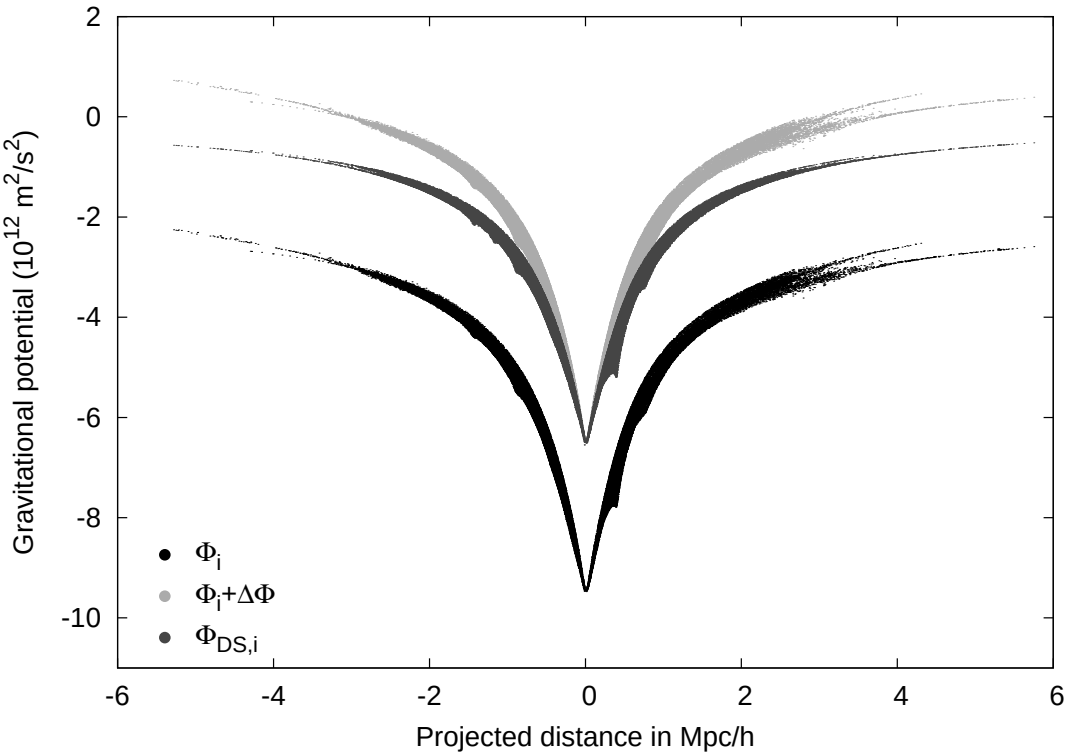

Figure 4.9: Comparison between the methods obtaining the gravitational potential for the energy calculation. In black the values obtained from the N-body simulation as an interpolation from the grid cells to the particles' position are shown (lowest curve). The same data points shifted by $\Delta\Phi$ are plotted in light gray. As a comparison are is the gravitational potential obtained through direct summation, $\Phi_{DS,i}$, shown dark gray. On the x-axis the quantity $\Delta r \cdot \mathrm{sgn}(\Delta x)$ is used as projected distance.

is due to nearby halos and unbound objects, which can be inside or close by the halo, that all have an gravitational effect on the halos' particles.

The third possibility – using the scalar product between the acceleration and the position of the particle – has two main advantages: Firstly, it is computationally much less expensive as not even $\Delta\Phi$ has to be computed directly. Secondly, in section 4.1 it was shown that $W = \tilde{W}$, but only if gravity is the *only* force acting on the body. In the case of the modified gravity models, there is an additional force acting on the particles. This can be also rephrased in terms of energy: The scalar field which is part of these models, contains energy, too.

In Fig. 4.10, it can be seen that the three methods differ more than expected. It is also noticeable that without the renormalization of $\Delta W_P = \Delta\Phi M_{\mathcal{H}}/2$, the energies obtained through summation of the gravitational potentials (rightmost panel) differs greatly from the other two methods. However, with the renormalization the mean, first and third quantile of the distributions are very similar: $(0.06, -0.54, -0.30)\,\mathrm{TJ\,kg^{-1}}$ for the distribution of $W_a/M_{\mathcal{H}}$ (third panel), $(-0.37, -0.42, -0.26)\,\mathrm{TJ\,kg^{-1}}$ for the direct summation method (second panel) and $(-0.35, -0.43, -0.27)\,\mathrm{TJ\,kg^{-1}}$ for $(W_P + \Delta W_P)/M_{\mathcal{H}}$ (first panel from

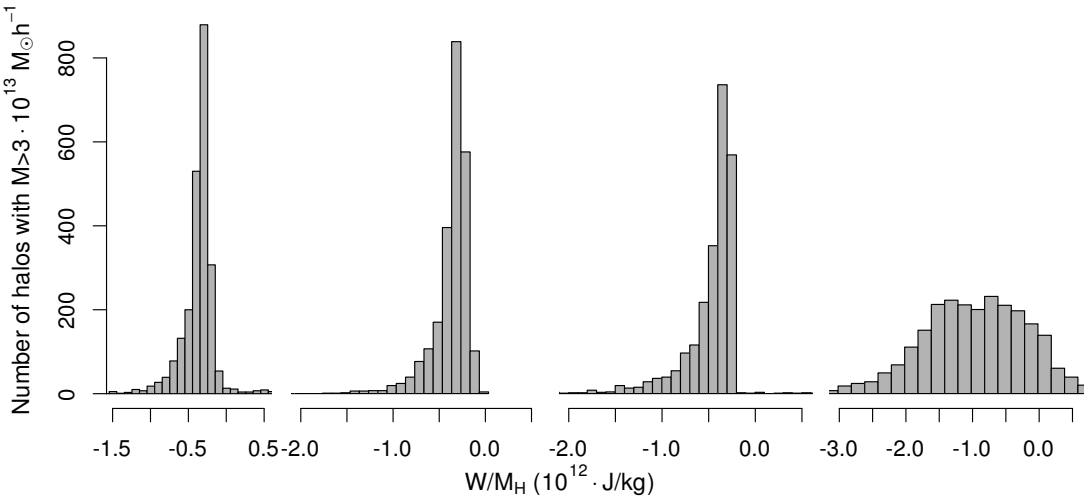

Figure 4.10: The four ways of calculating the potential energy: Histograms with the potential energy per halo mass for halos bigger than 3×10^{13} on the x axis. From left to right it is shown: *(i)* The normalized W_P, that is $W_P + \Delta\Phi M_{\mathcal{H}}/2$, *(ii)* W_{DS}, *(iii)* W_a, *(iv)* W_P. Note that the binsize is doubled in the last panel. All data used is from the ΛCDM run.

the left). The shift in the mean of $W_a/M_{\mathcal{H}}$ is due to ~ 10 outliers with values as high as $185 M_{\mathcal{H}}\,\mathrm{TJ\,kg^{-1}}$.

From these techniques the one which is best suited in order to calculate β_{vir} can be seen by comparing the distribution of virialization parameters shown in Fig. 4.11. While the β_{vir}-distribution obtained from the direct summation and the particles' acceleration agree well, using $W_P + \Delta W_P$ leads to more spread out β_{vir} values. This is due to the crude approximation of ΔW_P: As it was shown in Fig. 4.9, $\Phi_{DS,i}$ and $\Phi_i + \Delta\Phi$ do not agree well on the halo boundary and consequently W_{DS} and $W_P + \Delta W_P$ can differ substantially.

The surface pressure term

The third quantity, the surface pressure at the boundary E_S, is often not stated because for a system in total isolation this term vanishes. For a halo where a rather arbitrary cut has been made at R_{vir} to define the members of a halo this is obviously not true: Particles which are not member of a given halo but nevertheless gravitationally bound add a contribution to the overall energy. Consequently, the term stated in Eq. (4.22) cannot be neglected.

Throughout the calculations presented in this thesis, the E_S term was calculated following Shaw et al. (2006) who use an approximation that is motivated by the ideal gas law. In this the pressure p and the kinetic energy T are connected by

$$pV = \frac{2}{3}T\,. \tag{4.64}$$

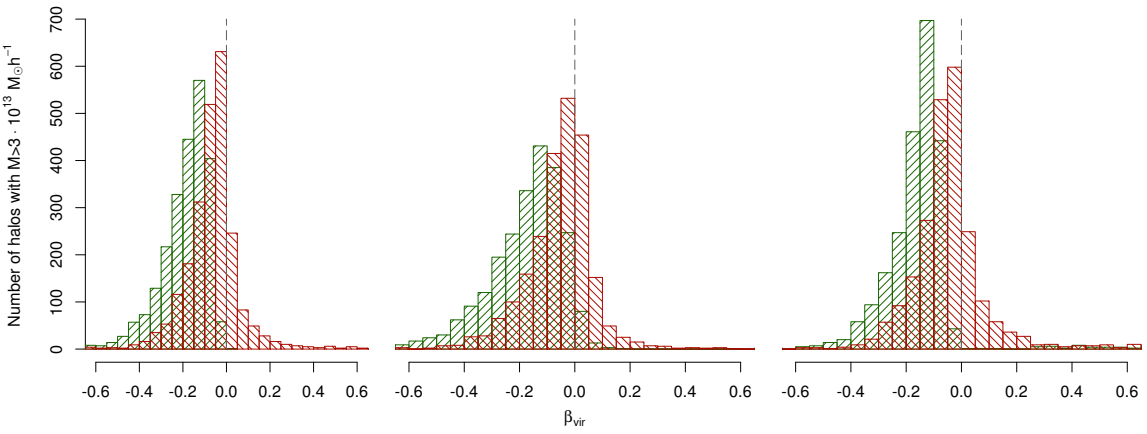

Figure 4.11: Distribution of the virialization parameter with (red color, downwards hatching) and without (green, upwards hatching) the surface pressure term E_s. From left to right for the gravitational potential energy W_{DS}, $W_P + \Delta W_P$ and W_a was used in order to calculate β_{vir}. The data shown is from the ΛCDM data set.

Using as volume the outermost 20% of the halos particle distribution, the surface pressure can be approximated by

$$p_S = \frac{1}{3}\frac{\sum_i m_i(\mathbf{v_i} - \mathbf{v}_\mathcal{H})^2}{4/3\pi(R^3_{1.0} - R^3_{0.8})} \; . \tag{4.65}$$

Here the notation R_x is used to describe the x-percent quantile of the particle distribution. Therefore, the surface pressure term can be calculated using

$$E_s \approx 4\pi R^3_{0.9} p_S \; . \tag{4.66}$$

The effect of the surface pressure term are similar to the ones described by Shaw et al. (2006), i.e. shifting the distribution of β_{vir} towards smaller values as it can be seen in Fig. 4.11, in which β_{vir} is shown using the data of the N-body simulation.

4.4.1 Virialization parameter in scalar-tensor theories

In the case of scalar-tensor theories, the energy of the scalar field has to be included in the considerations, as well. This is done automatically in W_a, if the total acceleration is considered, i.e. $\ddot{\mathbf{x}}_\mathbf{i} = \ddot{\mathbf{x}}_{N,i} + \ddot{\mathbf{x}}_{\mathrm{Fifth},i}$. That this additional contribution cannot be neglected can be seen in Fig. 4.12, where $\beta_{DS,a} = (2T - E_S)/W_{DS,a}$ have been compared: For ΛCDM, the *fofr6* or the *symm_A* model, the deviation is not significant, but in the more extreme models (*fofr4*, *symm_D*) the direct summation method is clearly not sufficient. Therefore, in this work β_a was used as already done in the spherical collapse model.

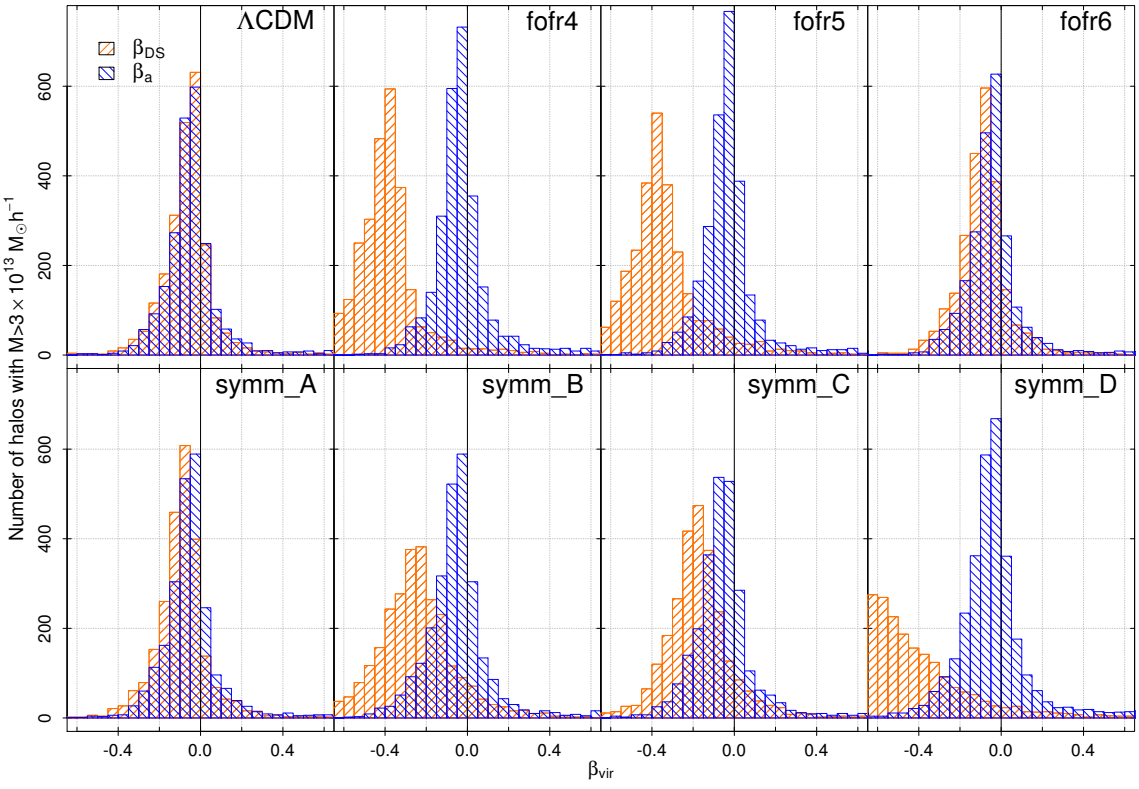

Figure 4.12: Distribution of the virialization parameter β_{vir} for halos with mass $M > 3 \times 10^{13} M_\odot h^{-1}$. β_{DS} (using the potential energy W_{DS} obtained through direct summation) is shown in orange with upward hatching and β_a (using W_a) is shown in blue with downward hatching.

5

Gravitational Redshift in Screened Modified Gravity

In the following chapter, the main results obtained in this thesis are presented. First, the extraction of the data is explained and applied to the ΛCDM run as an example. Secondly, the comparison of the quantities obtained in the $f(R)$ and symmetron runs are compared to the ΛCDM data and discussed. In order to understand the deviation in gravitational redshift also the density profiles, the fifth force and the velocity dispersion profiles are analyzed. In addition, the deviation in the matter power spectra and halo mass functions are shown for completeness. In the last part, possible sources of error and a brief comparison with observational data is laid out.

5.1 Obtaining the gravitational redshift

In order to obtain the gravitational redshift, first the gravitational potential at each particle's position is needed. To achieve this, an additional modification of the N-body code was made: If a flag was set the code interpolated the properties (density, gravitational potential, ...) to the particles' position via inverse-CIC as done before; but instead of moving them and continuing with the next time step these properties were written in a file. This allowed us to use the efficient potential calculation method of RAMSES and to output the following properties: Position of the particle $\mathbf{x_i}$, velocity of the particle $\mathbf{v_i}$ (both used for the halo finding process), Newtonian gravitational potential Φ_N, Newtonian force per unit mass $\ddot{\mathbf{x}}_N \equiv \mathbf{F}_N/m$, fifth force per unit mass $\ddot{\mathbf{x}}_{\mathrm{Fifth}} \equiv \mathbf{F}_{\mathrm{Fifth}}/m$ and the matter density ρ. Special attention was made to output the Newtonian gravitational acceleration separately from the scalar field as only the former influences photons as explained in Sec. 2.4.

The measured gravitational redshift was then defined as in Kim & Croft (2004) and Wojtak et al. (2011):

$$v_g = \frac{\Delta\Phi}{c} = \frac{\Phi_c - \Phi}{c} \,, \tag{5.1}$$

where Φ_c is the gravitational potential at the center of the cluster which is – following the definition of the center of the cluster done in Sec. 3.4 – the minimal gravitational potential found in the halo. Therefore, v_g is always negative and can be interpreted as the gravitational blueshift of light seen by an observer located at the center of the halo.

Instead of defining a single point as the center of the cluster and calculating the gravitational redshift with respect to that point, it is also possible to model the central galaxy as being spread out and take an average over gravitational potentials of the most central particles as the reference point. This procedure is used by Kim & Croft (2004) and leads to a flattening of the profile. However, they found out that the effect is rather small for dark-matter-only simulations. Due to this finding and also the fact that our results are consistent with the NFW predictions, we do not adopt the alternative procedure. In order to find the deviation in the gravitational redshift of modified gravity models with respect to ΛCDM – which is the goal of this work – the choice of technique is not crucial. If, however, the focus is on comparing the results with observational data, the measure of gravitational redshift is highly important to maximize the signal-to-noise ratio. Conclusively, for future work the measure of gravitational redshift might have to be modified.

5.2 The NFW profile

Navarro, Frenk & White (1995; 1996; 1997) found a fitting function to dark matter halos given by

$$\rho(r) = \rho_{c,0} \frac{\delta_{char}}{c_v \frac{r}{r_v}(1 + c_v \frac{r}{r_v})^2} \, . \tag{5.2}$$

Here r_v is the virial radius, c_v the concentration value and δ_{char} the characteristic overdensity given by

$$\delta_{char} = \frac{1}{3} v g(c_v) c_v^3 \, , \tag{5.3}$$

where

$$g(c_v) = \frac{1}{\log(1 + c_v) c_v / (1 + c_v)} \, . \tag{5.4}$$

The virial radius is defined by the parameter v as the border where the halo density drops below v times the critical density today. In Sec. 4.2 it was shown that this value is 178 for an Einstein-de Sitter universe 380 in the ΛCDM spherical infall model. As discussed in section 3.4, the results presented in this work are obtained with the value $v = 200$.

This leaves only one free parameter, c_v, for halos of a given size. In spite of its simplicity, the NFW-profile is still comparable with high resolution simulations (e.g. Ludlow et al. (2013)).

The gravitational potential of a density profile given by Eq. (5.2) with a total mass of M_v inside the virial radius is (Cole & Lacey, 1996)

$$\Phi(r) = -M_v G \frac{g(c_v)}{r} \log(1 + c_v \frac{r}{r_v}) \tag{5.5}$$

and hence

$$\Delta\Phi(r) = \Phi_c - \Phi(r) = -c_v g(c_v) \frac{GM_v}{r_v} \left(1 + \frac{r_v}{r} \log(1 + c_v r/r_v)\right) \tag{5.6}$$

because $\Phi_c \equiv \lim_{r\to 0} \Phi(r)$ is finite although Eq. (5.2) is not.

For the projected potential at a distance $r_p = \sqrt{r^2 - \Delta x^2}$ from the center, we follow Lokas & Mamon (2001) and define the 2D mass distribution function:

$$f(r,r_p) = \frac{\rho(r)}{\rho_\Sigma(r_p)} \tag{5.7}$$

where $\rho_\Sigma(r_p)$ is the average density along the line of sight, i.e.

$$\rho_\Sigma(r_p) = 2 \int_{r_p}^{\infty} \frac{r\rho(r)}{\sqrt{r^2 - r_p^2}} \mathrm{d}r \tag{5.8}$$

$$= \frac{M_v}{2\pi} \frac{g(c)}{r_p^2 - (r_v/c)^2} \left(1 - \frac{\arccos\left(\frac{r_v}{cr_p}\right)}{\sqrt{(cr_p/r_v)^2 - 1}}\right) \ . \tag{5.9}$$

Note that in the last term $\arccos(1/x)/\sqrt{x^2-1}$ the nominator as well as the denominator become purely complex for $x = cr_p/r_v < 1$, resulting nevertheless in a real result.

So the projected potential difference is

$$\Delta\Phi_p(r_p) = \frac{2}{\rho_\Sigma(r_p)} \int_{r_p}^{\infty} \frac{r\rho(r)}{\sqrt{r^2 - r_p^2}} \Delta\Phi(r) \, \mathrm{d}r \ . \tag{5.10}$$

These equations can be used to fit the data. The resulting concentration values found can be compared to observational data.

5.3 Uncertainty estimation

The question we want to address is: How different is a prediction for an observable given one theory compared to the same observable in another underlying model? In order to answer this question, the measure of interest is the ratio of these two quantities. This means concretely for the observable O and the model i the relative deviation is given by the

observable in the modified gravity model divided by the same observable obtained in the ΛCDM run (minus one), i.e.

$$\mathcal{R}^{(i)} = \Delta O/O_{\Lambda CDM} = O_i/O_{\Lambda CDM} - 1 \; . \tag{5.11}$$

The easiest and most straightforward procedure to obtain an uncertainty estimate for the relative deviation would be to run the simulation several times. Out of the resulting means, and their standard deviations it is possible to obtain an overall ratio and error (Lee & Forthofer, 2006, Chap. 4). This method was chosen by Brax et al. (2012, 2013) for the matter power spectra and halo mass functions. The aim of this work is instead to emphasize on the halo structure, which requires a higher dynamical range than the one used by Brax et al. Hence, the computational power is not available for this procedure and this precision.

Please note, that simply taking the variance of the observed values *inside* a single simulation run would not be sufficient because the point of interest is not the confidence interval of an observable but of its mean. The crude estimation of the individual samples (i.e. the halos) being independent would lead to the standard error of the mean.

A method that is commonly used to avoid running a large number of computationally expensive simulations is to create new "fake" data points. The intention is that they are being drawn from the same (or a very similar) distribution function as the underlying distribution. One possibility used for projected quantities is to change the projection angle as done for instance in Forero-Romero et al. (2010). Another possibility would be to divide the simulation box in several sub-samples and obtaining multiple values instead of just one from a single simulation run, which is the procedure we follow here. The box was split in $n = 8$ equal sub-boxes, each giving a relative deviation $\mathcal{R}_i$, which results in an overall $\bar{\mathcal{R}}$ mean and error of this mean is given by (Everitt & Skrondal, 2002)

$$SE_{\bar{\mathcal{R}}} = \frac{s}{\sqrt{n}} = \left(\frac{\sum_{i=1}^{n} (\mathcal{R}_i - \bar{\mathcal{R}})^2}{n(n-1)} \right)^{1/2} \; . \tag{5.12}$$

The error estimation obtained from this method is not as good as for a sample of independent runs. This is the case especially for larger halos as the long modes are not independent in each sub-box. Nevertheless, this procedure is sufficient for our purpose.

Another important point in the uncertainty estimation is the consideration of systematical errors due to the resolution of the N-body simulation. As mentioned in Sec. 3.3, the simulation box had a side-length of $256\mathrm{Mpc\,h^{-1}}$ which contained 512^3 particles. The maximum refinement level was chosen to be 16, which is the maximum number of times the box can be split in a high-density region. Thus, in the highest level of refinement the simulation box has 2^{16} nodes per dimension, resulting in a minimum cell size of $\sim 4\,\mathrm{kpc}\,h^{-1}$. We estimated the resolution to be twice that minimum cell size, which is $\sim 8\,\mathrm{kpc}\,h^{-1}$. In order to show the capabilities and limits of the available simulation sets, we preferred sometimes to show data points located below this resolution limit as well.

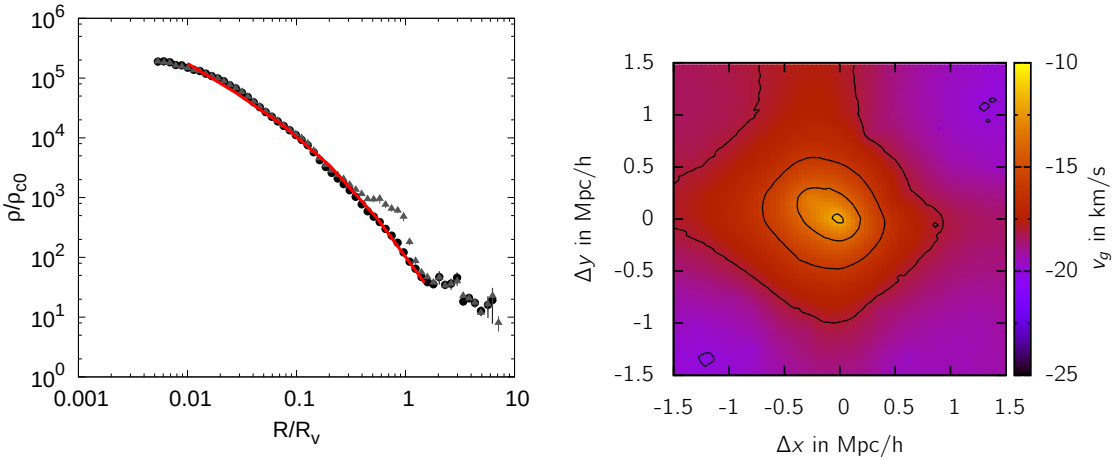

Figure 5.1: *Left panel:* Average density at the particle positions for halos with masses $10^{14} M_\odot/h < M < 10^{14.5} M_\odot/h$. For the black round points only the particles of the host halo are included, the gray triangles include the subhalos and the red line is a NFW fit to the data. *Right panel*: Projection of a halo. The coloring and the contour lines correspond to the difference in gravitational potential.

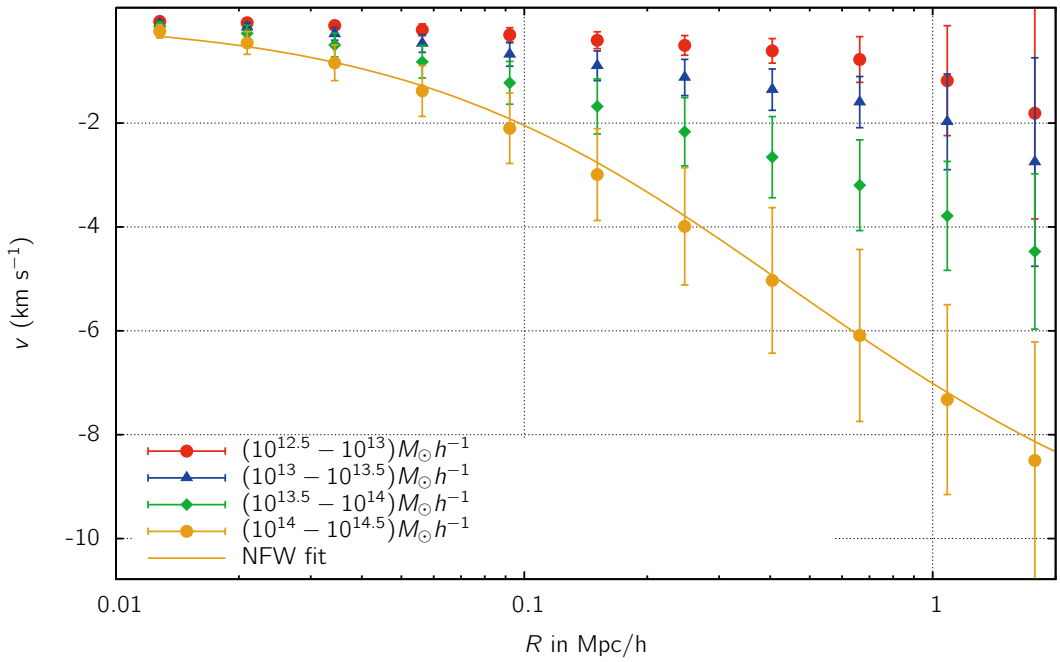

Figure 5.2: Difference in gravitational redshift of the ΛCDM simulation between the central galaxy and the individual halos binned in radius and halo mass. The error bars show the standard deviation of all halos and are therefore not the same as the model comparison. The NFW fit uses the mean values of the high mass bin.

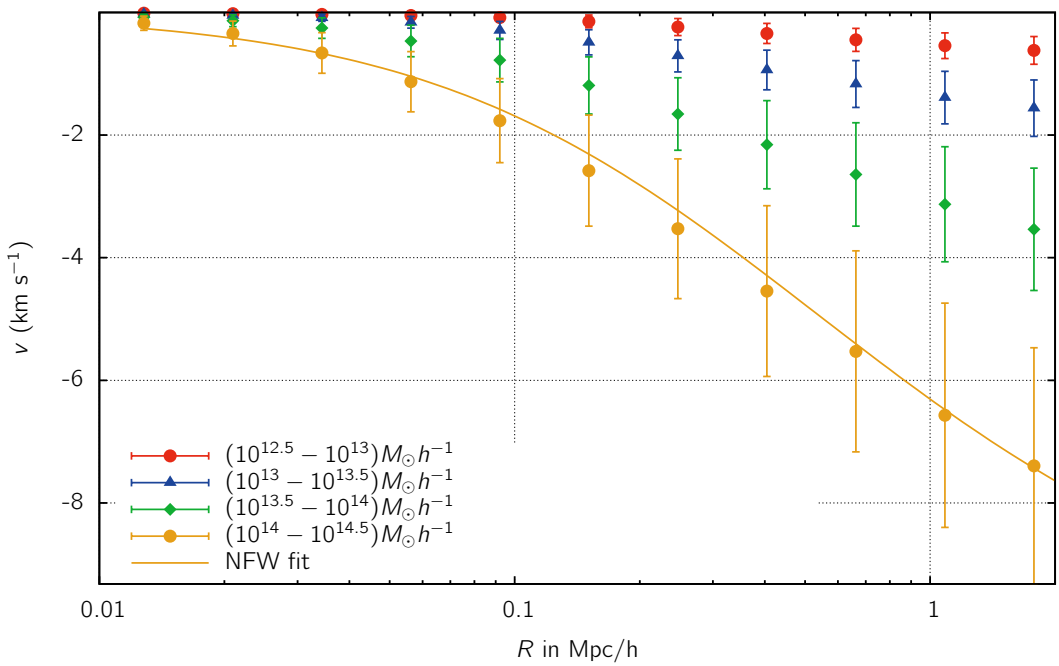

Figure 5.3: Difference in gravitational redshift of the ΛCDM simulation between the central galaxy and the individual halos binned in radius and halo mass. This time only the virialized ($|\beta| < 0.2$) halos have been included and the radii have been virialized. The NFW fit uses the mean values of the $10^{14} - 10^{14.5} M_\odot\, h^{-1}$ mass bin.

5.4 Cluster profiles in the ΛCDM model

The right panel of Fig. 5.1 shows the projection of a single halo. The color coding corresponds to the average gravitational redshift associated to the particles in the area. It is possible to that close to the center of the halo (at $\Delta x = \Delta y = 0$) the gravitational redshift reaches its minimum. It does, however, not reach zero since a projection of the halo is shown. In the left panel of Fig. 5.1, the mass density for halos with mass $10^{14} M_\odot\, h^{-1} < M < 10^{14.5} M_\odot\, h^{-1}$ is plotted against the normalized radius. Subhalos are included in the data points represented by gray triangles and a bump around $R \approx R_v$ due to them is clearly visible. The NFW fit provided follows nicely the density points without subhalos (black dots).

In order to obtain the halo redshift profiles we take the difference in gravitational potential between the central particle and each member of the halo. The result for the complete sample – binned in radial bins and halo mass bins – is presented in Fig. 5.2. As expected the profile is steeper for more massive halos and is consistent with the NFW profile calculated in Sec. 5.2. This is also consistent with the theoretical predictions from Cappi (1995).

Please note, as consequence of the used binning, each data point is not represented by the same number of particles or halos: Especially for larger radii only the more massive halos are contributing. As the lighter halos shown in Fig. 5.2 with halo mass of $12.5 < \log(Mh/M_\odot) <$

13, have a typical virial radius of $0.26\,\mathrm{Mpc}\,h^{-1}$, only a few particles were taken into account for larger radii. This and the fact that some of these particles on the far edge are unbound or part of elliptical halos lead to a wide spread of data far away from the center.

To overcome this problem and to avoid contaminating the sample with major mergers for which the gravitational redshift is ill defined, we subtract halos with a virialization parameter $|\beta_{vir}| < 0.2$, where β_{vir} was calculated as described in Sec. 4.4. In other words, the distribution of the virialization parameter shown in Fig. 4.12 is cut off at $\beta_{vir} = \pm 0.2$.

This removes around half of all the halos from each data sample. Mainly smaller halos are removed: For the ΛCDM data, the four halo mass bins adopted, i.e. $\log(Mh/M_\odot) \in ((12.5, 13), (13, 13.5), (13.5, 14), (14, 14.5))$, loose (28, 19, 13, 17) percent of the halos, which leaves (13118, 5060, 1544, 315) halos. The three halos in the data set with masses larger than $10^{14.5} M_\odot\, h^{-1}$ are also unvirialized according to our definition. In addition, we normalize the radii with the virial radius of each halo in order to make a fair comparison between halos in each mass bin. The normalization allows us also to compare deviations in fixed radial bins between different mass bins. As Fig. 5.3 shows, these measure decrease the variance of the data points, especially for the smaller halo mass bins. Now, the trend of blueshifting is visible for halos with masses $12.5 < \log(Mh/M_\odot) < 13$, too.

5.5 The $f(R)$ models

As we are interested in how the introduction of a fifth force changes the halo profile, we will investigate the relative deviation of the quantities v_G and $\Delta\rho$, that is $n_i/n_{\Lambda CDM} - 1$ where n_i and $n_{\Lambda CDM}$ are the quantity in the modified gravity data set i and in the ΛCDM data set, respectively. As discussed in Sec. 5.3, the error was estimated by dividing the simulation box into 8 sub-boxes and using the variance of the relative deviation calculated in each subset to fix the error of the mean. The data sample was binned in two ways: First, the same way as in Fig. 5.2–5.3 with the variation of the normalized radius in the four previously adopted halo mass bins between $10^{12.5} M_\odot\, h^{-1}$ and $10^{14.5} M_\odot\, h^{-1}$. In addition, the deviation at a fixed distance as a function of the halo mass was analyzed. For the comparison between the models only the virialized halos (with $|\beta_{vir}| < 0.2$) were used. In all the Figures in this section, the color coding is consistent and corresponds to the three $f(R)$ parameter sets summarized in Table 3.1.

5.5.1 Matter power spectra and halo mass functions

The relative deviation in the matter power spectrum $\Delta P/P_{\Lambda CDM}$ and in the halo mass function $\Delta N(>M)/N(>M)_{\Lambda CDM}$ shown in Fig. 5.4 is merely provided for completeness and overview of the models.

The matter power spectrum for each model was calculated using the publicly available `powmes` code (Colombi et al., 2009). The halo mass function $N(>M)$ is defined by the number of halos whose masses are bigger than a mass M. The impact on the change of the

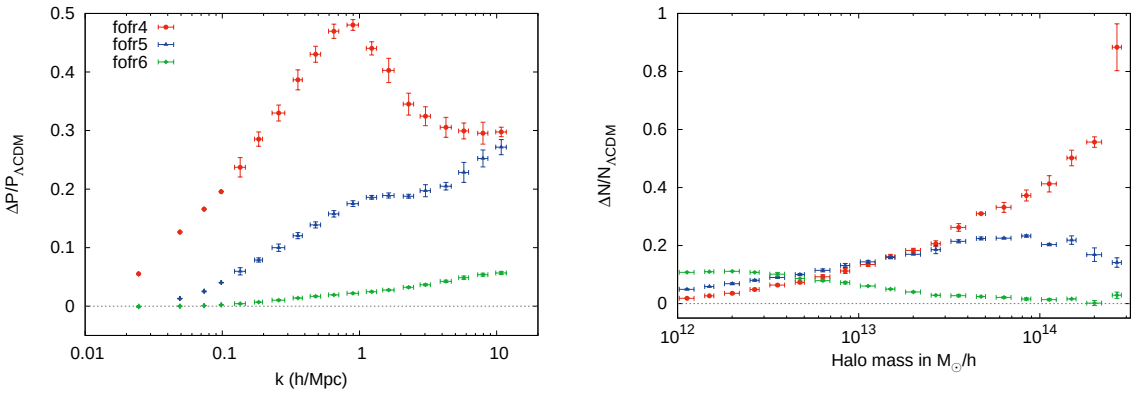

Figure 5.4: Relative deviation in the matter power spectra (*left panel*) and the halo mass function (*right panel*) The error bars indicate the spread of values in a given bin.

halo mass functions as well as the linear matter power spectra in the generalized chameleon and the $f(R)$ model was already done by Brax et al. (2013) and Li et al. (2012) and is not subject of this work. Please note, that the error bars provided show only the standard deviation for one bin, not the deviation between several samples as done in the further analysis. It can be observed that *(i)* the higher the $|f_{R0} - 1|$ value, the higher the deviation from ΛCDM and *(ii)* that each of the models has a certain halo mass range of impact. These features can be seen clearer in the upcoming sections and will be discussed there. The third point to note is the very high deviation in the *fofr4* model not only for small scales, but also for low values of k which suggest the need of renormalizing σ_8. See Sec. 5.8 for a discussion about this and other systematic effects.

The variation in the halo mass functions agrees very well with the results from Li & Hu (2011) who covered the same $f(R)$ parameters in their considerations. They predict a further growth in the deviation in the $|f_{R0} - 1| = 10^{-4}$ case for halos up to $M = 10^{15} M_\odot\, h^{-1}$, but no deviation in this mass range if $|f_{R0} - 1| = 10^{-5}$.

5.5.2 Chameleons in the wild: The fifth force unbound

In Fig. 5.5 the absolute value of the directly obtained additional acceleration $|\ddot{\mathbf{x}}_{\mathrm{Fifth}}|$ is shown as a function of halo mass for fixed radial bins (upper panels) and as a function of normalized radius for fixed halo masses (lower panels).

In the upper row of Fig. 5.5, we can see that for every radial bin, each set of parameters results in a certain characteristic halo mass range beyond which the fifth force is screened at the higher end and the scalar field less affected at the lower end. In the *fofr5*-model, for example, the fifth force around $0.1R_v$ is the strongest for halo with masses $12.5 \lesssim \log(Mh/M_\odot) \lesssim 14$ (see upper right panel). In the *fofr6* model this range can be seen in the radial bin around the virial radius R_v: For $M \gtrsim 10^{14}\, M_\odot h^{-1}$, the fifth force is completely screened. In this radial bin, the *fofr5*-peak moved to higher masses ($\sim 10^{14}\, M_\odot h^{-1}$) since the screening mechanism depends on the local matter density which declines with increasing radius. A

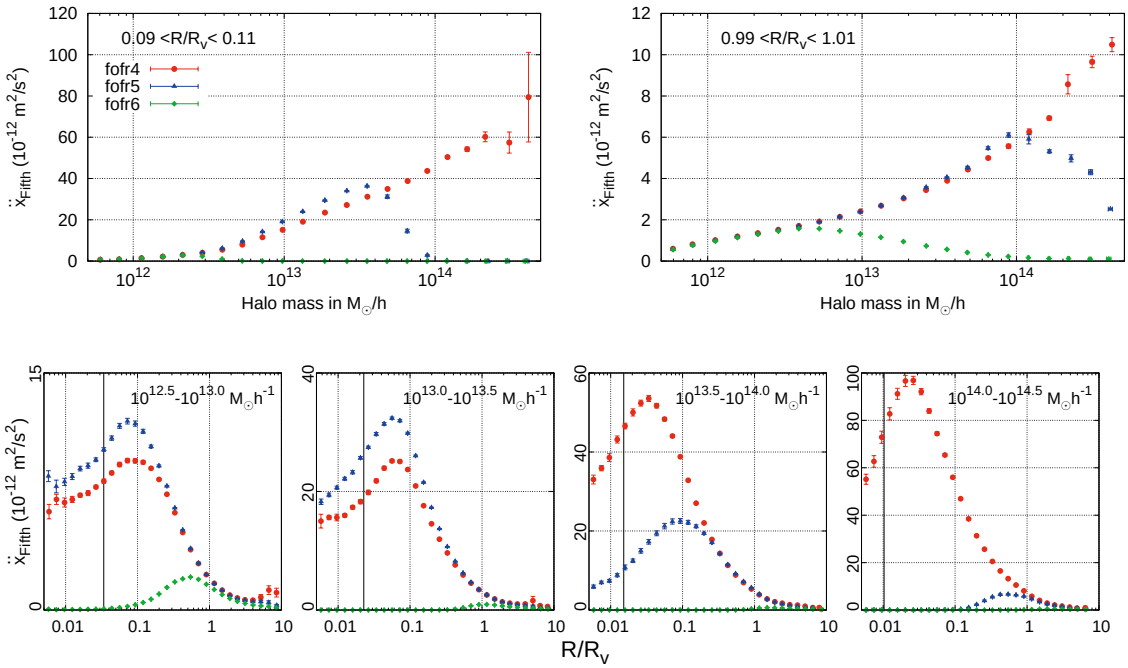

Figure 5.5: Additional acceleration $\ddot{\mathbf{x}}_{\mathrm{Fifth}}$ due to the presence of a scalar field in the $f(R)$ model. *Upper panel:* $|\ddot{\mathbf{x}}_{\mathrm{Fifth}}|$ as a function of halo mass for in the radial bin $R/R_v \approx 0.1$ (left) and $R/R_v \approx 1$ (right). *Lower panel:* $|\ddot{\mathbf{x}}_{\mathrm{Fifth}}|$ as a function of normalized radius for the halo mass ranges $(\log(M_{lower}h/M_\odot),\ \log(M_{upper}h/M_\odot)) = (12.5,13)$, $(13.13.5)$, $(13.5,14)$ and $(14,14.5)$ (from left to right). In all the graphs the red circles mark the *fofr4*, the blue triangles the *fofr5* and the green diamonds the *fofr6* run. In addition, the black horizontal line corresponds approximately to two grid cells in the finest refinement level.

similar screening of the fifth force for the *fofr4* model is expected for even greater densities. This means, we expect the *fofr4* curves in the upper panels of Fig. 5.5 to possess a maximum as higher halo masses than available in the data set.

The lower panels of Fig. 5.5 show the radial dependency of the fifth force. In each panel, a horizontal black line marks the approximate[1] size of two grid cells in the finest refinement level, which is roughly the resolution limit. A feature of all curves – with the exception of the *fofr6* results for high masses – is their characteristic maximum. Also, the decline of the fifth force for increasing R seems to be identical for the outer radii. This independence of the shape from the f_{R0} value can especially be seen for the *fofr4* and *fofr5* curves since $\ddot{\mathbf{x}}_{Fifth}$ is much weaker in the *fofr6* case. However, the position of the characteristic maxima is highly dependent on the f_{R0} parameter: In the two lower-mass panels the *fofr4* and *fofr5* curve have their characteristic maximum around $R \approx 0.1R_v$, while the *fofr6* data points suggest a maximum around $0.5R_v$ and R_v for the mass ranges $10^{12.5} - 10^{13}\,M_\odot h^{-1}$ and $10^{13} - 10^{13.5}\,M_\odot h^{-1}$, respectively. Also the magnitude of the additional acceleration depends

1 For each mass bin the mean virial radius of the ΛCDM run was used to calculate the approximate grid cell size.

on f_{R0}. The simple relationship – the closer f_{R0} to unity, the stronger the additional force – holds mostly. It is not necessarily true, however, in the "preferred mass range" which was identified in the upper panels of Fig. 5.5. So is, for example, the fifth force stronger with $|f_{R0} - 1| = 10^{-5}$ (*fofr5*) compared to $|f_{R0} - 1| = 10^{-4}$ (*fofr4*) for halos with masses between $10^{12.5}\, M_\odot h^{-1}$ and $10^{13.5}\, M_\odot h^{-1}$.

In order to understand the features of Fig. 5.5 it is important to recall how the chameleon screening works and how a fifth force arises in this context. As previously discussed in Chapter 2, a fifth force arises if the value of the scalar field ϕ changes in space. This change in ϕ happens, because the scalar field settles in the minimum of the effective potential ϕ_{min} whose position depends on the local matter density ρ. The screening nature of this mechanism is due to the fact that ϕ_{min} changes only minimally for high density regions. That is, the fifth force is effectively zero if ρ is greater than a certain density threshold. The value of this threshold depends on the model parameter $|f_{R0} - 1|$. Consequently, there is two possibilities for a vanishing fifth force: *(i)* The local matter density ρ does not change or *(ii)* ρ is greater than the screening threshold.

Since the halo density decreases with increasing R, the vanishing fifth force for large radii is due to reason *(i)*. This means, fifth force declines at larger R because the matter density does not change as strongly as in the regions around the characteristic peak in $\ddot{\mathbf{x}}_{\mathrm{Fifth}}$. The decline of the additional acceleration left of the maximum can be due to *(i)* or *(ii)*: *(i)* considering the density in the inner radii might be greater than the screening threshold mentioned above or *(ii)* since the matter density profile flattens in the central region as a result of the simulation resolution. Hence, the difference between the resolution limit (marked with a vertical black line in Fig. 5.5) and the position of the characteristic peak plays an important role. If the peak is very close to the resolution limit, then the decline for smaller radii is due to reason *(ii)*. Another criterion for *(ii)* can be established by including the mass dependency features of $\ddot{\mathbf{x}}_{\mathrm{Fifth}}$ shown in the upper row of Fig. 5.5: If for the smaller radial bin (left upper panel) the curve is rising – that is the fifth force is larger for more massive halos and, thus, higher local densities – the screening in that mass range cannot be active. Hence, the radial decline of the fifth force is due to *(i)* if the $\ddot{\mathbf{x}}_{\mathrm{Fifth}}$ versus M curve is falling for a given halo mass range. In addition, the characteristic peak in the $\ddot{\mathbf{x}}_{\mathrm{Fifth}}$ versus R data should not be too close to the resolution limit.

Applying these criteria to the data shown in the lower row of Fig. 5.5, we can state:

- The *fofr4* result show the inner falling of the fifth force is due to reason *(ii)* for all shown mass ranges. Here, the characteristic peak is always very close to the resolution limit.

- For the *fofr5* results *(ii)* is only the case for masses between $10^{12.5}$ and $10^{13.5}\, M_\odot h^{-1}$ (two leftmost panels). For the two bigger mass ranges, the decline can be accounted for *(i)*, that is the screening in the central regions. It is noteworthy that the characteristic peak for the mass range $10^{13.5} - 10^{14} M_\odot h^{-1}$ is at $\sim 0.1 R_v$ and for $10^{14} - 10^{14.5} M_\odot h^{-1}$ around $0.4 R_v$.

- The characteristic peak in the *fofr6* data is always far away from the resolution limit. Hence, the decline of the fifth force in the central regions of the halos is due to screening, i.e. reason *(ii)*.

These findings are in agreement with the expectations: The lower $|f_{R0} - 1|$, the lower is the density threshold above which the chameleon screening is effective.

5.5.3 Gravitational redshift profiles

Since the measurable signal of the gravitational redshift is proportional to the difference in gravitational potential, the quantity v_g is a direct measurement of the shape of the gravitational potential well. Hence, the relative deviation of this quantity, i.e. $\Delta v_g/v_{g,\Lambda CDM}$, which is shown in Fig. 5.6–5.7, describes the change in this shape with respect to ΛCDM. This means, if the potential well is deeper in the center and/or shallower for larger R, $\Delta v_g/v_{g,\Lambda CDM}$ is positive. With a fifth force acting on the particles, we expect additional clustering to happen and, consequently, this is the expected case to happen. If, on the other hand, the potential well is not as deep in the center and/or deeper in the outskirts than in the ΛCDM model, the observable $\Delta v_g/v_{g,\Lambda CDM}$ will be negative.

In Fig. 5.6 the relative deviation of the gravitational redshift v_g with respect to ΛCDM is shown. We see, the smaller f_{R0}, the smaller is the deviation from ΛCDM, as expected. Especially for the $|f_{R0}-1| = 10^{-6}$ case, the result is basically indistinguishable from ΛCDM, except a small bump for the smallest halos around $R \approx R_{vir}$. On the other hand, for the more extreme cases of $|f_{R0} - 1| = 10^{-4}$ and $|f_{R0} - 1| = 10^{-5}$ the relative deviation is much larger, especially for small radii. In most of the parameters the results show a stronger gravitational redshift, which is the result of the increased clustering in the center of the halo due to the fifth force: Stronger clustering in the center means a deeper gravitational potential well and, hence, a larger gravitational redshift.

The strength of this effect changes with the cluster mass, e.g. for the *fofr5* data set the enhancement at $R/R_{vir} = 0.1$ is around 18% for the smallest halo mass range (top left panel of Fig. 5.6), then increases to 45% for bigger halo masses (top right panel in the same figure) just to drop then dramatically for even bigger halos. For the model with $|f_{R0} - 1| = 10^{-4}$ we observe a converse feature at the same radius: For the biggest halos there is a strong enhancement of the gravitational redshift whereas for the smaller halos the redshift observed is even smaller than in the ΛCDM case. These trends can be best seen in Fig. 5.7 where for a fixed radial the relative deviation of the gravitational redshift is shown. In these slices, the bump of deviation for the *fofr6* model is much clearer. Due to its position between $10^{12}\,M_\odot h^{-1}$ and $10^{13}\,M_\odot h^{-1}$, it did not appear as clearly in the mass bins of Fig. 5.6. One very interesting feature of Fig. 5.7 is the characteristic position of the maximum deviation from ΛCDM depending on the f_{R0} value: In the *fofr6* data the maximum deviation is for halos with masses around $2 \times 10^{12} M_\odot h^{-1}$, for $|f_{R0} - 1| = 10^{-5}$ it is around $3 \times 10^{13} M_\odot h^{-1}$ whereas $|f_{R0} - 1| = 10^{-4}$ results in a change of the biggest halos in the data set. This maximum is consistent throughout all mass bins, but as seen in Fig. 5.6 it varies in strength.

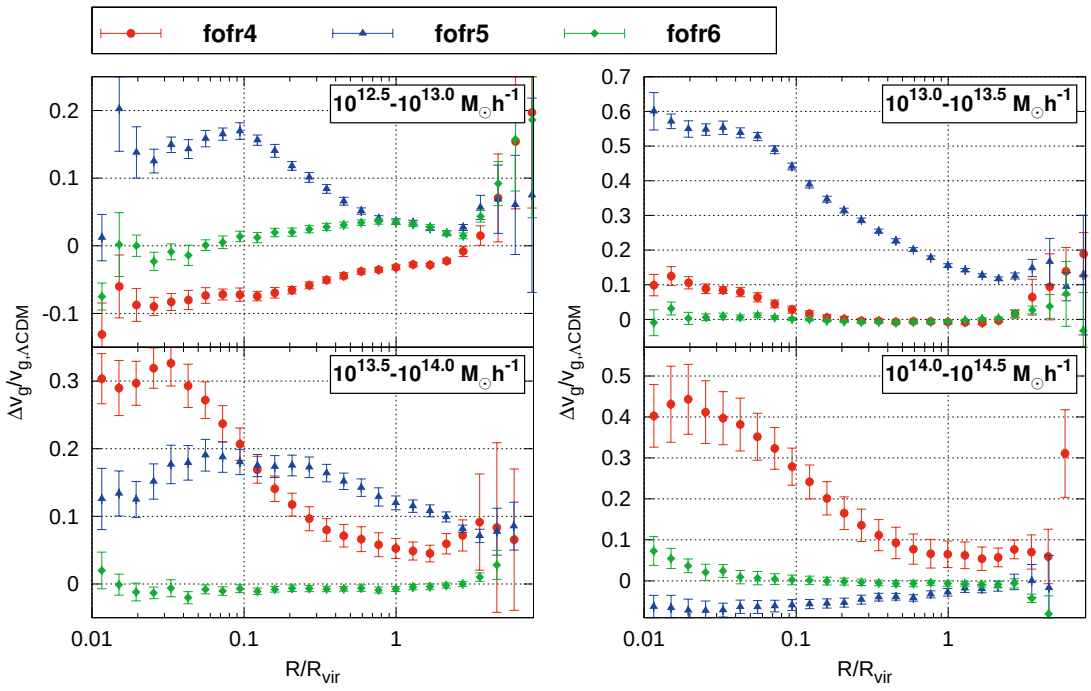

Figure 5.6: Relative deviation in gravitational redshift between the $f(R)$ runs and the ΛCDM run. Here the red circles mark the *fofr4*, the blue triangles the *fofr5* and the green diamonds the *fofr6* run. The four panels show the result obtained for different halo masses ranging from $10^{12.5}$-$10^{13} M_\odot h^{-1}$ (upper left) to 10^{14}-$10^{14.5} M_\odot h^{-1}$ (lower right panel).

As discussed in the previous section, the reason for the existence of such a characteristic range of halo sizes lies in the nature of the screening mechanism: Halos heavier than a certain threshold have a big enough density to activate the screening mechanism to kick in. Hence, the value of the scalar field is very small, there is no fifth force and therefore no additional clustering in the center. Only halos within this mass range have an altered structure and as a result, we obtain the characteristic bumps in Fig. 5.7. The position of the maxima supports the explanation given: The closer the f_{R0} value to unity, the smaller are the affected halos. Naturally, these mass ranges correspond to the ones mentioned in the last section (compare to the upper panels of Fig. 5.5).

The position and magnitude of the characteristic peak in the $\ddot{\mathbf{x}}_{\text{Fifth}}$ versus R plots (lower panels of Fig. 5.5) plays also an important role when interpreting the gravitational redshift results. If the position of the peak is close to the center of the halo, the fifth force will lead to a deeper potential well and an enhanced gravitational redshift. The stronger the fifth force is in this regions, the bigger the enhancement. Comparing the findings of the last section with the gravitational redshift results, we find:

- In the *fofr4* case, the relative deviation is biggest for the most massive halos considered. This agrees with the strong additional force found in the central regions of these clusters. Also for halos with mass $10^{13.5} - 10^{14}\, M_\odot h^{-1}$ the deviation is overall greater

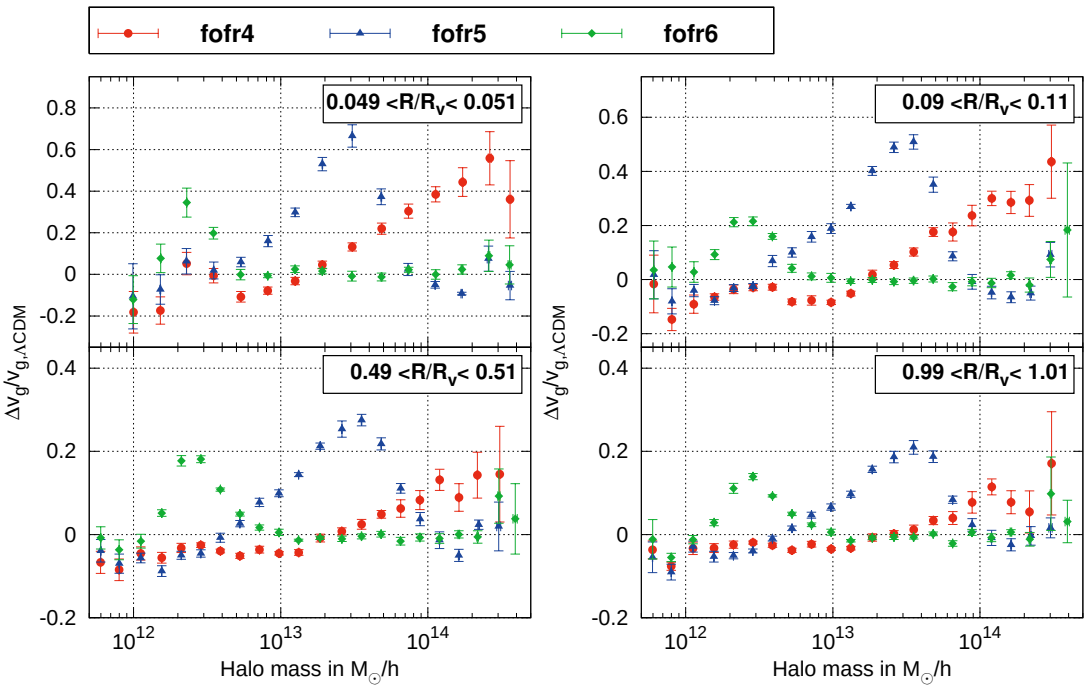

Figure 5.7: Relative deviation in gravitational redshift of the $f(R)$ models with respect to ΛCDM plotted against the halo mass for fixed radial bins ($R/R_v \approx (0.05, 0.1, 0.5, 1)$ from left top to right bottom). Here the red circles mark the *fofr4*, the blue triangles the *fofr5* and the green diamonds the *fofr6* run.

than in the other cases, just as the fifth force was strongest. A strange feature is the negative deviation found for the smallest masses. This is most probable and an artifact due to the resolution limit but could also be accounted on the fact that the strongly increased clustering leads to more small halos being located closer to bigger halos and therefore in higher density regions.

- The *fofr5* data shows also the most deviation when the fifth force was most active, i.e. for the $10^{13.5} - 10^{14}\, M_\odot h^{-1}$ mass range. The fact that for the biggest halos the screening mechanism suppresses the fifth force in the central regions and, consequently, the additional clustering takes place around the virial radius, results in a negative deviation of v_g. Although we account the decline of the fifth force in the central regions of the halos with mass $10^{13} - 10^{13.5}\, M_\odot h^{-1}$ also on screening, the position of the characteristic peak in the $\ddot{\mathbf{x}}_{\rm Fifth}$ versus R plot around $0.1R_v$ is here much closer to the center. Thus, the deviation in v_g for these halos is positive.

- Since $\ddot{\mathbf{x}}_{\rm Fifth}$ takes very small values for $|f_{R0} - 1| = 10^{-6}$ (*fofr6*), the results in gravitational redshift for masses $\gtrsim 10^{12.5}\, M_\odot h^{-1}$ are basically indistinguishable from ΛCDM. The characteristic mass range for the *fofr6* model is around $\sim 10^{12.2} M_\odot h^{-1}$ (see

Fig. 5.7). This is limiting the simulation's resolution limit. Therefore, we cannot analyze the radial dependency of the redshift deviation in detail.

5.5.4 The halo density profiles

Because the underlying cause for the change of gravitational redshift in the models considered is the change of the halo density profiles, we have measured these directly in two ways: Firstly, the matter density ρ obtained at a particle's position through an inverse cloud-in-cell algorithm similarly to the gravitational potential studied in the last section. The ratio of $\Delta\rho/\rho_{\Lambda CDM}$ is presented in Fig. 5.8. And secondly, the mean number of particles per halo in a given radial range from the center of its halo. The comparison of this quantity is shown in Fig. 5.9. Again, both quantities were binned in normalized radii and halo masses and compared to the ΛCDM values in the same way as used for the gravitational redshift before.

Both comparisons show the same features as seen previously in the gravitational redshift (Fig. 5.6). One important difference is, however, the quicker fading away of a deviation: E.g., the deviation in redshift for halos with masses $10^{13} - 10^{13.5}\,M_\odot h^{-1}$ in the *fofr5*-model is clearly visible even for radii $R \gtrsim R_{vir}$ (see Fig. 5.6), whereas the deviation in N is already below 10% at $R \approx 0.02$ (see Fig. 5.9). We can conclude, that the effect of gravitational redshift is highly dependent on the cluster density at the center of the halo. This leaves a

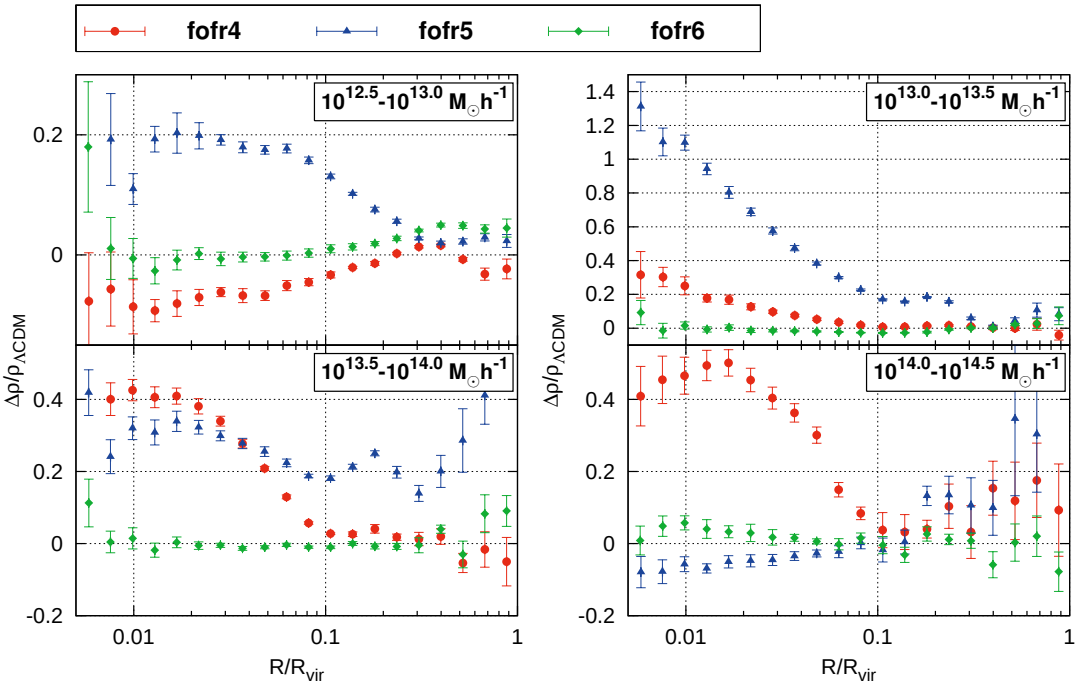

Figure 5.8: Relative deviation in the matter density ρ plotted against the normalized radius for the same mass bins as in Fig. 5.6.

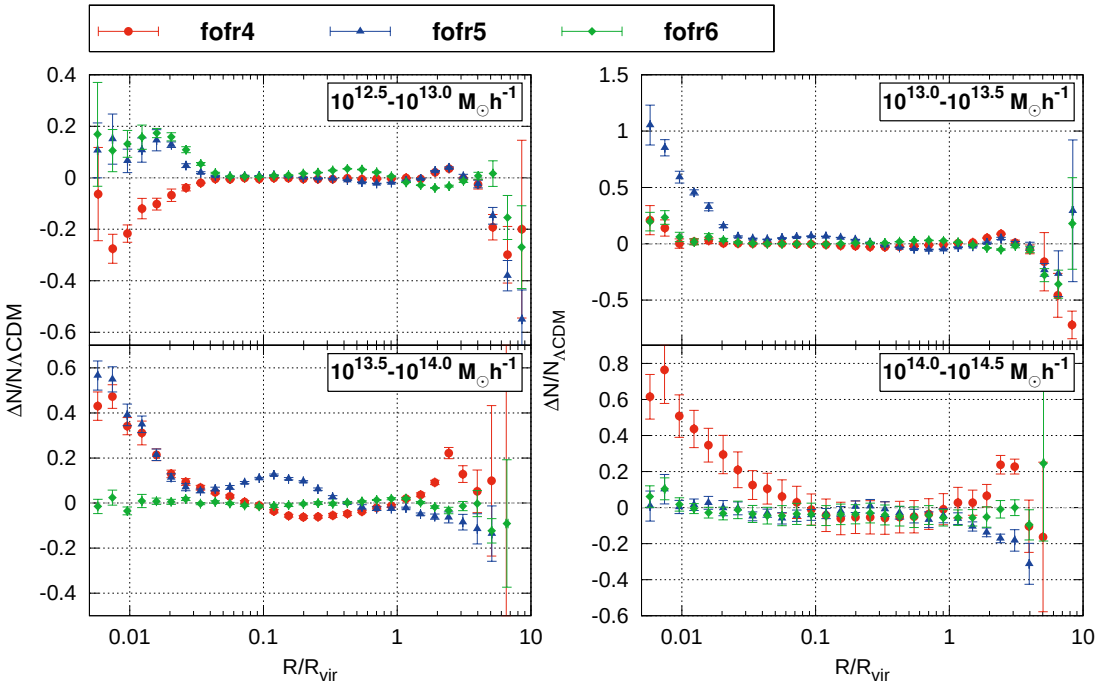

Figure 5.9: Relative difference between the mean number of particles found per halo in a given distance from the center of the halo. The results are presented in the same halo mass ranges as before, ranging from $10^{12.5} M_\odot h^{-1}$ in the upper-left panel to $10^{14.5} M_\odot h^{-1}$ in the lower-right one.

variety of possible implications, such as a different location of the densest region, which will be discusses in Sec. 5.8.

5.5.5 Velocity profiles

An important reason for analyzing the velocity dispersion of halos is to test if the increased matter density is not due to slower particles at that point. However, since there is an additional force accelerating the particles, that finding would be very unexpected.

The velocity dispersion as defined in Eq. (4.60) and its deviation from the ΛCDM values is shown in Fig. 5.10. As expected the dependency of the additional particle speed with the fifth force (Fig. 5.5) is clearly visible: The *fofr6* data only shows for the smallest halo mass bin some deviation in the region $\sim R_v$, where there is also the bump in the fifth acceleration. The particles are faster in the *fofr5* than in the *fofr4* data for halo masses $\lesssim 10^{13.5} M_\odot h^{-1}$, just as the fifth force is higher for the latter. If there is no additional force at a specific radius, σ^2 goes towards the ΛCDM value rather quick. So does the *fofr5* data set for radii $R \lesssim 0.1 R_v$. These results show that the increased particle density is not due to slower particles but due to additional cluster, as expected.

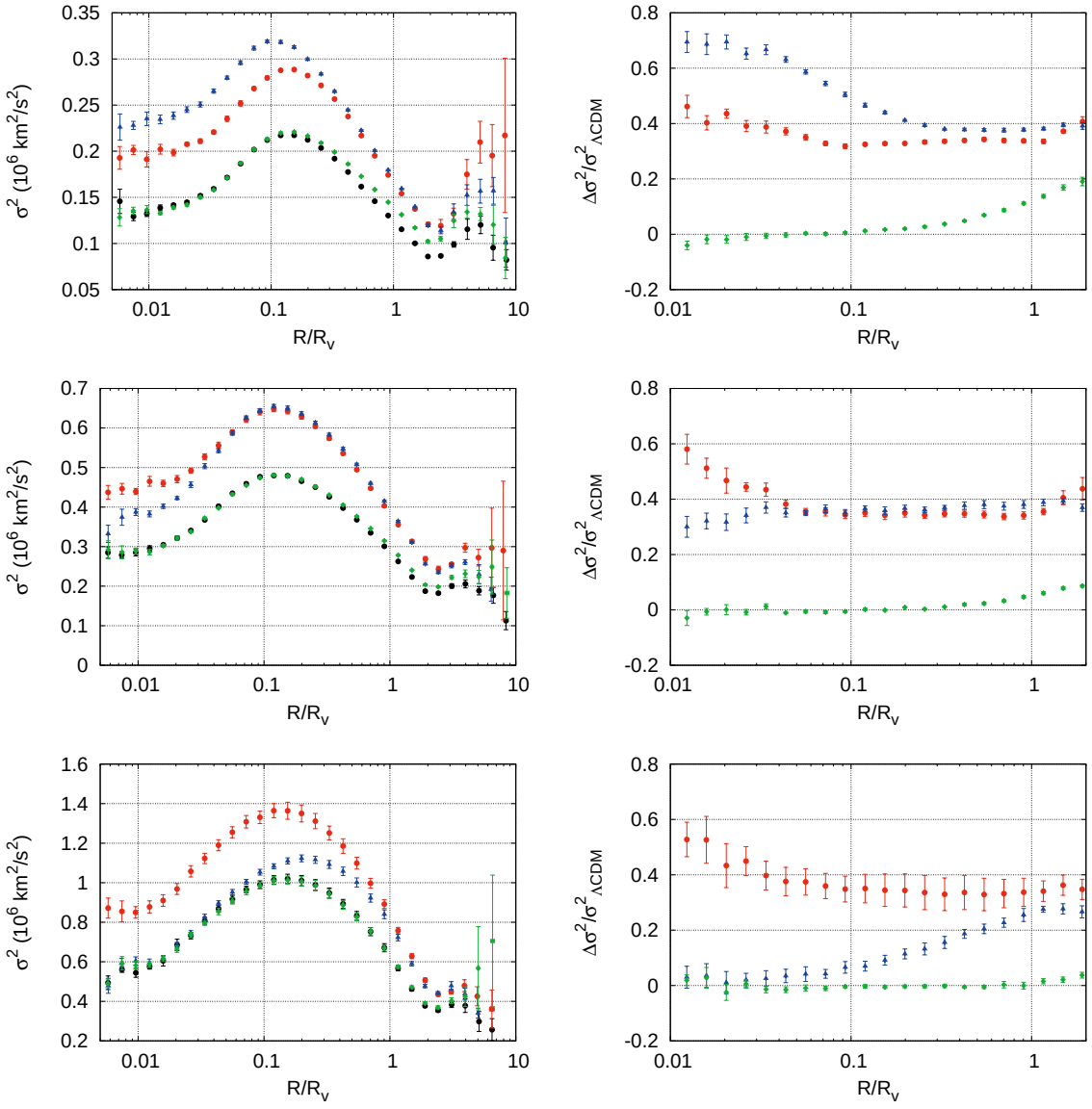

Figure 5.10: Velocity dispersion profiles (left) and relative deviation of velocity dispersion (right). Three halos mass bins are shown $13 < \log(Mh/M_\odot) < 13.5$ (top), $13.5 < \log(Mh/M_\odot) < 14$ (top) and $14 < \log(Mh/M_\odot) < 14.5$ (bottom). The color code is the same as for the other $f(R)$ plots, i.e. *fofr4* in red, *fofr5* in blue and *fofr6* in green with the additional data points of ΛCDM in black.

5.6 The symmetron models

For the analysis of the symmetron results, we follow the same structure as in the last section: First, the matter power spectra, halo mass functions and fifth force data are shown. Then, the gravitational redshift results are presented. And lastly, the quantities that can help explaining these results, that is the matter density and the velocity dispersion are given. Also here, the radii were normalized with the virial radius $R_v = R_{200}$ and only halos with $|\beta_{vir}| < 0.2$ were considered

5.6.1 Matter power spectra and halo mass functions

The same way as in the $f(R)$ section, the deviation in the matter power spectra and the halo mass function shown in Fig. 5.11 is given here merely out of completeness. However, the key points made in Brax et al. (2012) can be confirmed: Decreasing the symmetry breaking time a_{ssb} (*symm_A* versus *symm_B* versus *symm_D*) leaves the fifth force more time to be active and hence increases the effect on the matter power spectra and halo mass function. A similar effect is achieved by increasing the coupling constant β (*symm_A* versus *symm_C*) which controls the strength of the fifth force directly.

One striking difference between the *symm_D* results and the other models is the much higher number of medium and big halos (see right panel of Fig. 5.11). This increase cannot be explained in merely the slight mass increase of also in the ΛCDM data set existing halos. Instead, the creation of fully new, big halos mainly through clustering of many small or medium sized halos takes place. This phenomenon is also described by Li & Hu (2011) for their no-chameleon model.

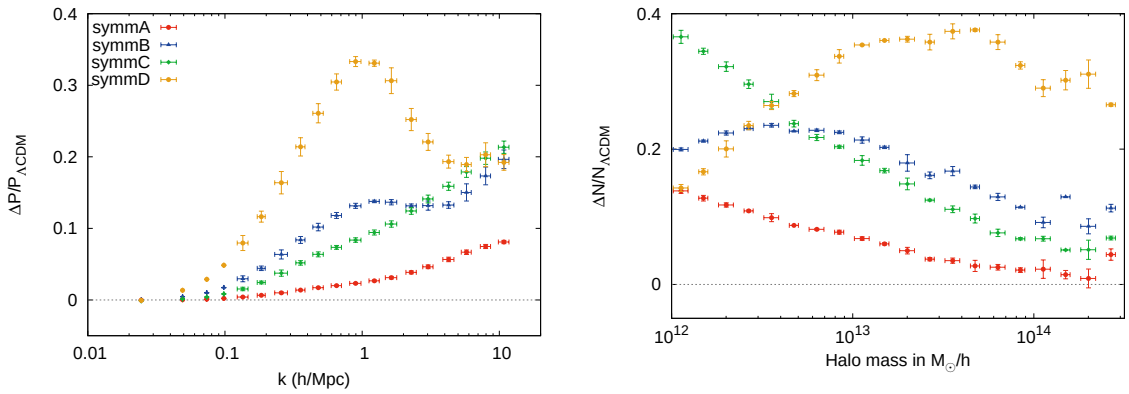

Figure 5.11: Relative deviation in the matter power spectra (*left panel*) and the halo mass function (*right panel*). The error bars indicate the spread of values in each bin.

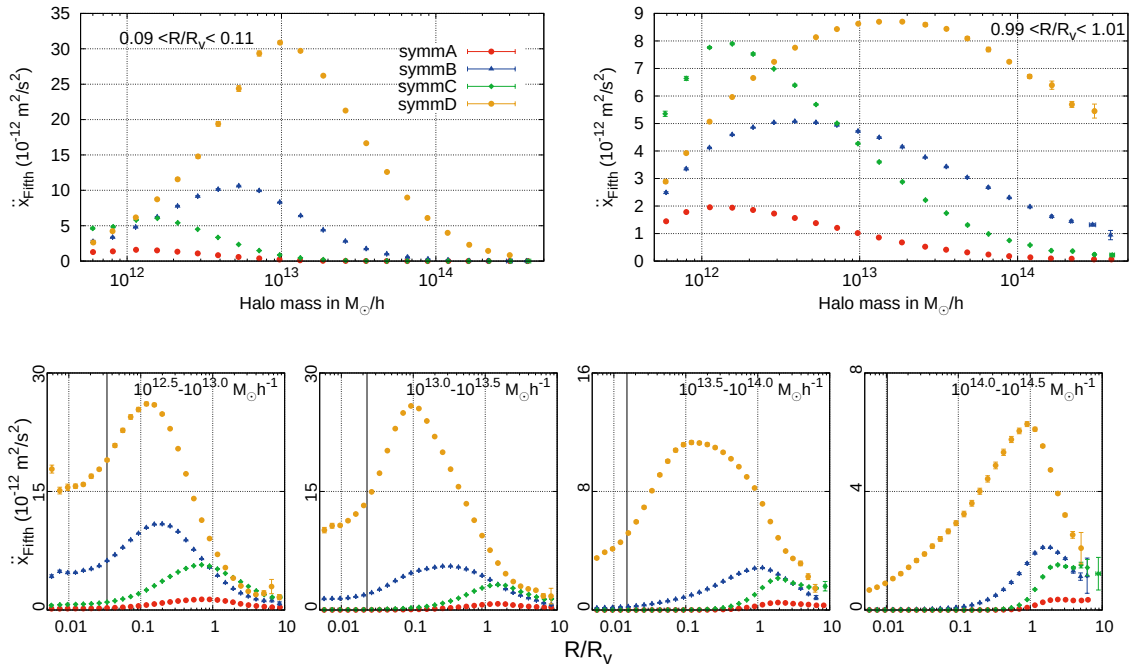

Figure 5.12: Additional acceleration $\ddot{\mathbf{x}}_{\rm Fifth}$ due to the presence of a scalar field in the symmetron model. *Lower panel:* $|\ddot{\mathbf{x}}_{\rm Fifth}|$ as a function of normalized radius for the halo mass ranges $(\log(M_{lower}h/M_\odot),\ \log(M_{upper}h/M_\odot)) = (12.5, 13), (13, 13.5), (13.5, 14)$ and $(14, 14.5)$ (from left to right). *Upper panel:* $|\ddot{\mathbf{x}}_{\rm Fifth}|$ as a function of halo mass for in the radial bins $R \approx 0.1R_v$ (left) and $R \approx R_v$ (right). In all the graphs the red circles mark the *symm_A*, the blue triangles the *symm_B*, the green diamonds the *symm_C* and the orange circles the *symm_D* run. The black horizontal lines correspond approximately to two grid cells in the finest refinement level.

5.6.2 Symmetron additional force

Fig. 5.12 shows the additional acceleration $\ddot{\mathbf{x}}_{\rm Fifth}$ versus the halo mass (upper row) and the normalized halo radius (lower row). The overall finding is that the *symm_D* parameter set results in the strongest fifth force, followed by *symm_C* and *symm_B*. The *symm_A* curve shows the least amount of additional acceleration. This confirms the expected relationships: *(i)* The earlier the symmetry breaking, the stronger the fifth force and *(ii)* an increase of the coupling constant also leads to an increased fifth force.

The upper row of Fig. 5.12 shows that in addition to the magnitude of $\ddot{\mathbf{x}}_{\rm Fifth}$ the model parameters alter also the mass range of the affected halos. So has the *symm_D* the strongest impact for halos $\sim 10^{13} M_\odot h^{-1}$ and is only fully screened in the center of halos with masses $\gtrsim 10^{14.3}\, M_\odot h^{-1}$ (upper left panel). The later the symmetry breaking time, the smaller are these two characteristic factors; e.g., the mentioned peak is for *symm_B* already around $10^{12.5} M_\odot h^{-1}$ and the fifth force in the central region becomes neglectable at masses $\gtrsim 10^{13.3} M_\odot h^{-1}$. In the *symm_A* case these values are even more shifted to lower masses.

In order to study the effect of an increased coupling parameter on the affected halo masses,

the *symm_A* data ($\beta = 1$) has to be compared with the *symm_C* results ($\beta = 2$). Here, it can be seen that the increase of β does not shift the mass range. So is the mentioned maximum of the force for both data sets slightly bigger than $10^{12} M_\odot h^{-1}$ at $R = R_v$ (top right panel). However, as mentioned above, increasing β increased the magnitude of the fifth force. This leads to the feature that around R_v and for halo masses $\sim 10^{12} M_\odot h^{-1}$ *symm_C* results in even a greater fifth force than *symm_D*.

The lower row of Fig. 5.12 can be analyzed in a similar way to the radial dependency of the fifth force Sec. 5.5.2. This means, the decline of the additional acceleration for bigger radii is due to the less changing matter density in the outskirts. Towards the central region, however, the decline can be also a result of the screening mechanism. This happens if the density there is above a certain effective threshold density, which for the symmetron model is equal to ρ_{ssb}, the average matter density at a_{ssb}. The criteria established in Sec. 5.5.2 for the differentiation between these two possibilities were *(a)* the proximity between the radius of maximal fifth acceleration and the resolution limit and *(b)* if $\ddot{\mathbf{x}}_{\mathrm{Fifth}}$ is greater for more massive halos in the central region.

For the symmetron model, we came to the following conclusions about the presence of the screening mechanism:

- *symm_D*: The fifth force in the central region is strongest for halos with mass $\sim 10^{13} M_\odot h^{-1}$ (see top left panel of Fig. 5.12). Hence, the smallest mass range analyzed is the only one where the screening mechanism is not active. This finding is supported by the fact that for this mass range the radial peak is very close to the resolution limit. However, for the next bigger halos, this peak is still very close to the central region ($\sim 0.1 R_v$). For even bigger halos, this radius of maximal fifth force moves further out until it reaches $\sim R_v$ for the biggest halos considered.

- *symm_A* and *symm_C*: $\ddot{\mathbf{x}}_{\mathrm{Fifth}}$ takes much smaller values than in the *symm_D* case. With the halo mass of the maximal affected central regions being $\sim 10^{12} M_\odot h^{-1}$, the screening mechanism is active for all the four halo mass ranges.

- *symm_B*: Since the described peak is around $\sim 10^{12.8} M_\odot h^{-1}$, for the last three halo ranges the screening is active in the central region. Also here it is noteworthy that the magnitude of the additional acceleration is very weak.

Conclusively, this means, while the overall behavior is similar to the chameleon mechanism, i.e. no fifth force in the center, a force maximum at intermediate radii and a downfall of the fifth force in outer radii, there are significant differences: In both models, there is a certain "threshold mass" for each radial bin above that the force is fully screened, as mentioned before. The results are indicating, while this threshold is very abrupt for the chosen $f(R)$ parameters, it is more gradiently in the symmetron model. This said, however, only a small area of the parameter space was probed and the symmetron model can have a similar behavior implying the right choice of parameters.

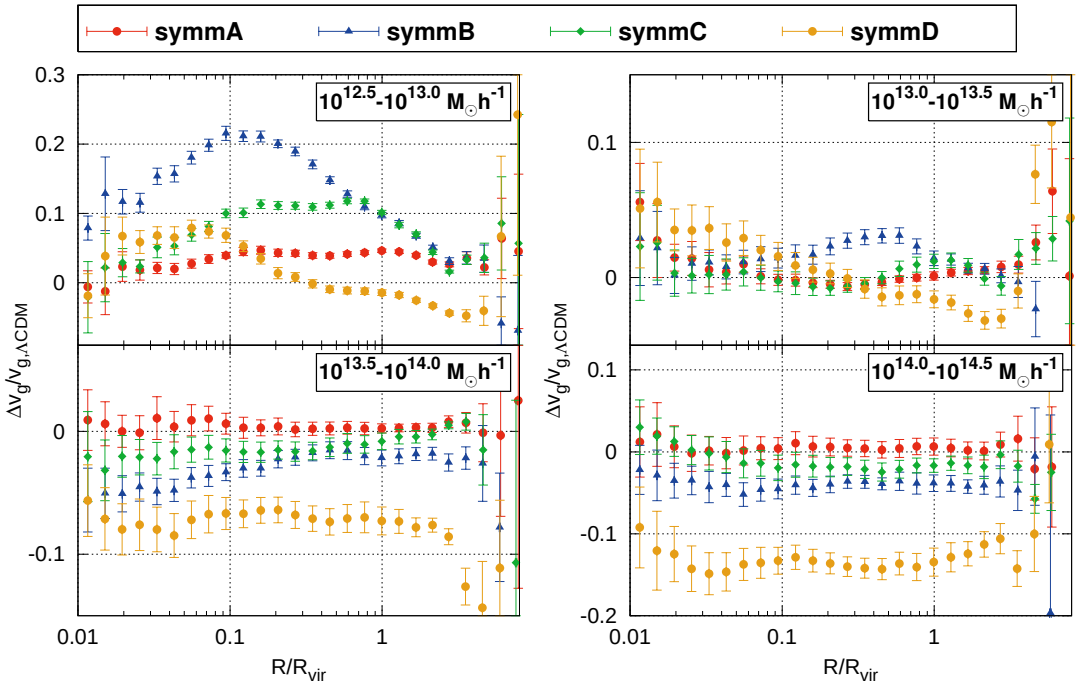

Figure 5.13: Relative deviation between the symmetron runs and the ΛCDM run. The red circles mark the *symm_A* and the blue triangles the *symm_B* run. Please note the change in scale compared to Fig. 5.6

5.6.3 Gravitational redshift profiles

Fig. 5.13 and Fig. 5.14 show the deviation in gravitational redshift with respect to ΛCDM versus the radius and the halo mass, respectively. Given the overall weaker additional forces discussed in the last section, it is not surprising the imprint in the variation of the gravitational redshift profiles is not as strong as it was the case for the $f(R)$ results. The maximal deviation is around 20% for the *symm_B* model for halos with masses between $10^{12.5}$ and $10^{13}\,M_\odot h^{-1}$ (top left panel in Fig. 5.13). As expected, especially the *symm_A* model with a very late symmetry breaking time is basically indistinguishable from ΛCDM.

One prominent feature that did not occur the same way in the $f(R)$ case is the negative deviation obtained for high ($\gtrsim 3\times10^{13}\,M_\odot h^{-1}$) and low ($\lesssim 3\times10^{12}\,M_\odot h^{-1}$) masses in the *symm_D* model. A similar but fainter imprint can be seen for the *symm_B* run with the difference that for intermediate masses ($\sim 8\times10^{12} M_\odot h^{-1}$) the positive deviation is much stronger than in the *symm_D* case. This fact paired with the very small radial dependency of the deviation for the bigger *symm_D*-halos denotes a less deep but wider gravitational well, i.e. less matter in the central parts and more in the outskirts of the clusters. This weaker gravitational redshift with respect to ΛCDM is an unexpected result since the additional force should lead to an enhanced clustering and, thus, a stronger gravitational redshift. This maybe unexpected feature can be explained with the radial position of the additional clustering as discussed in the last section. If the central region is screened and the fifth force

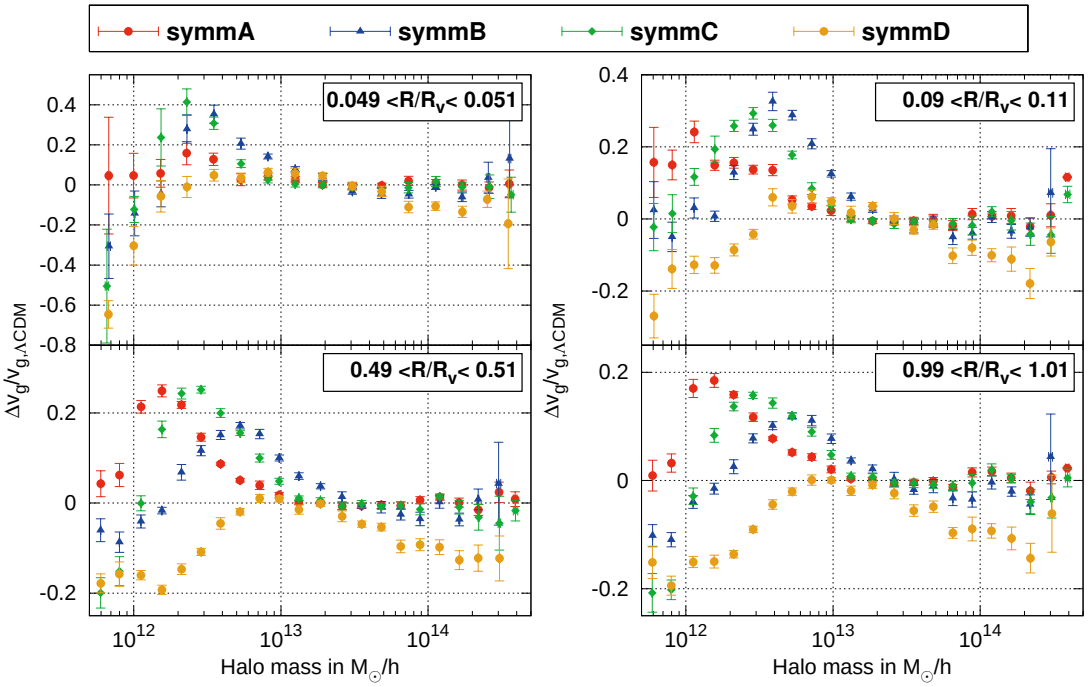

Figure 5.14: Relative deviation in gravitational redshift of the symmetron models against ΛCDM plotted against the halo mass for a fixed radial bin. Here, the red circles mark the *symm_A*, the blue triangles the *symm_B*, the green diamonds the *symm_C* and the orange circles the *symm_D* run.

is strongest for larger radii, the additional clustering takes place in the outskirts of the halo leading to a less deep and wider potential well. Such a shape of the potential well results in a negative deviation in v_g.

5.6.4 Halo density profiles

In Fig. 5.15 the deviation in matter density ρ for the symmetron model is shown. The trends seen in the gravitational redshift profiles can be rediscovered in this plot: Hardly any deviation from ΛCDM for *symm_A*, then more for model "B" followed by "C", just as the strength of the fifth force seen in Fig. 5.12.

The presumption for the reason of the constant lower redshift for the bigger halos of the *symm_D* model can be confirmed: While the matter density is lower at smaller radii than in the ΛCDM sample, with bigger radius this value increases by up to twenty percentage points. Just the opposite case happens for the smaller halos: The deviation in the matter density seems to be constantly increased around $15-20\%$ leaving the characteristic drop in the gravitational redshift seen in the upper panels of Fig. 5.13.

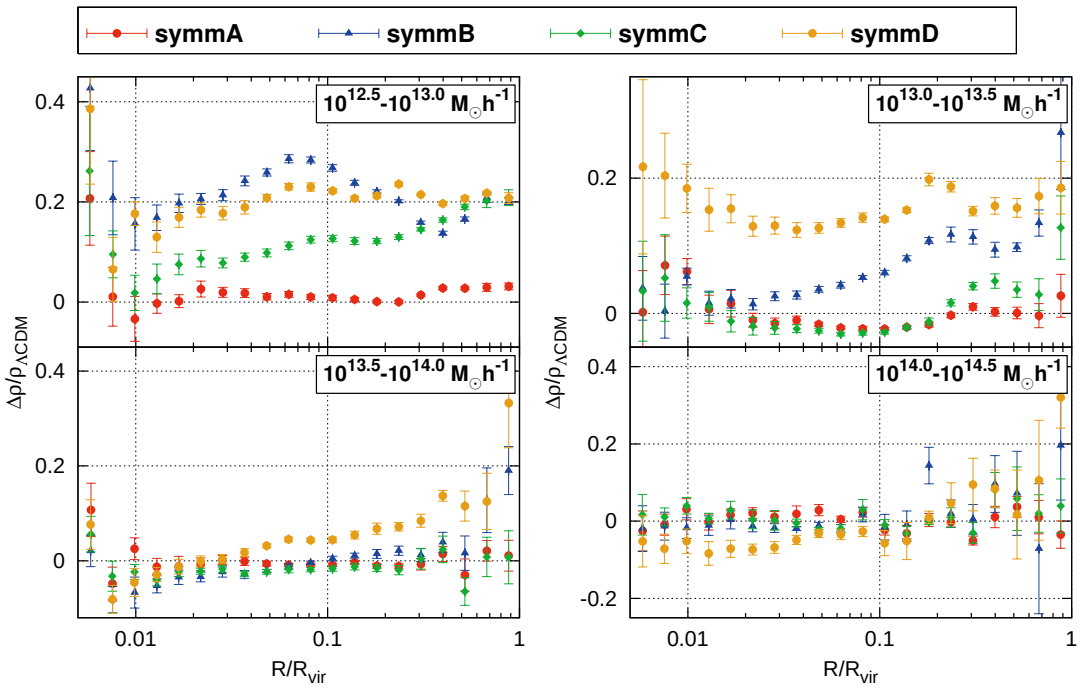

Figure 5.15: Relative deviation in the matter density ρ between the symmetron and the ΛCDM models. The results are presented in the same halo mass bins as before, ranging from $10^{12.5} M_\odot h^{-1}$ in the upper-left panel to $10^{14.5} M_\odot h^{-1}$ in the lower-right one.

5.6.5 Velocity profiles

In Fig. 5.16 the velocity dispersion profiles and their deviation from ΛCDM for the symmetron runs is shown. As expected, the extra speed of the particles is highly dependent on the strength of the fifth force in that region (compare with Fig. 5.12): The fastest particles are to be found in the "D" model, slowest in *symm_A*. In all plots, the deviation curve consists of a nearly constant part up to $\sim 0.1\, R_v$ and then a linear increase. The value of the constant part depends on the value of the additional acceleration for small radii: E.g., the fifth force was already fully screened in the *symm_B* case for masses between 10^{13} and $10^{13.5}\, M_\odot h^{-1}$ around $0.1 \times R_v$ while in the *symm_C* case it was not. This results in a different constant value of the $\Delta\sigma^2/\sigma^2_{\Lambda CDM}$ curve.

An important point to note is, that the negative deviation in mass density in the *symm_D* model is not due to a higher particle velocity since for the biggest masses all the velocities below $0.1\, R_v$ are comparable.

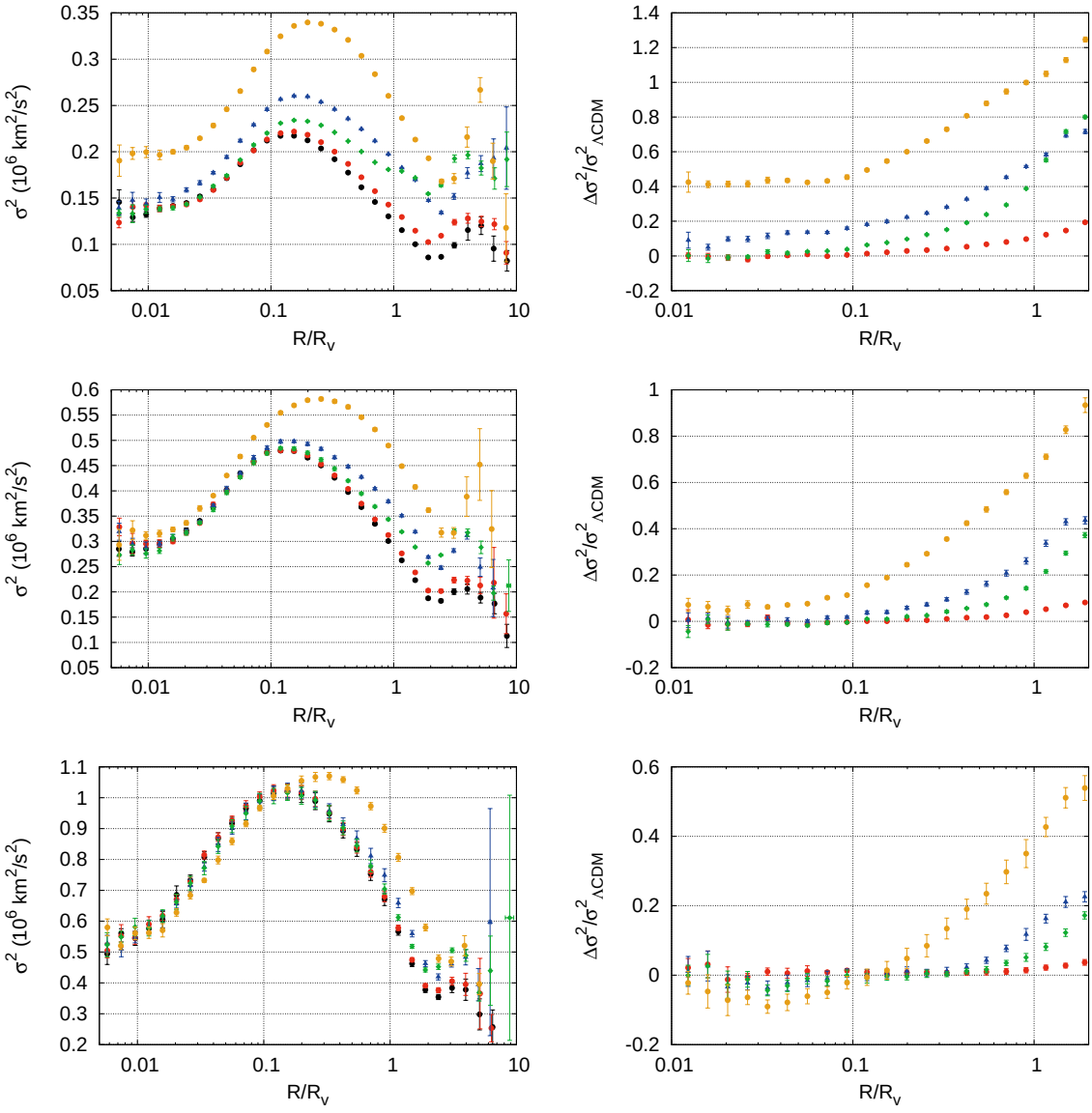

Figure 5.16: Velocity dispersion profiles (left) and relative deviation of velocity dispersion (right). Three halos mass bins are shown $13 < \log(Mh/M_\odot) < 13.5$ (top), $13.5 < \log(Mh/M_\odot) < 14$ (center) and $14 < \log(Mh/M_\odot) < 14.5$ (bottom). The red circles mark the *symm_A*, the blue triangles the *symm_B*, the green diamonds the *symm_C*, the orange circles the *symm_D* and the black points the ΛCDM run.

5.7 Connection to observational data

Measuring the gravitational redshift directly is very hard as it is only possible to measure the total redshift of an object. The main contributions of this total redshift z_{tot} of an galaxy which is d_{los} away from the observer are given by three components:

$$cz_{\mathrm{tot}} = H(z)d_{los} + v_{\mathrm{pec}} + v_g \ . \tag{5.13}$$

In this equation the gravitational redshift v_g is about two orders of magnitude smaller than the Doppler shift due to the peculiar motions of the galaxies in the halo v_{pec}. Nevertheless, the two components can be separated because the mean of the gravitational redshift has a radial dependency while the other one has not.

The first detection of gravitational redshift in clusters was done by Wojtak et al. (2011) using 7800 clusters from the SDSS data set. Several corrections to their predictions have been made later on: Zhao et al. (2012) pointed out that due to the relative motion of the galaxies, an additional component because of time-dilation exists. This term is called transverse Doppler effect and has opposite sign as v_g. This and other effects, e.g., a changed redshift as a result of relativistic beaming, have been analyzed by Kaiser (2013), all of them should be considered when doing a proper analysis of observational data. As the scope of this work is, however, the deviation of v_g in screened modified gravity models with respect to ΛCDM, these additional effects have not been studied and have not been included in Fig. 5.17 where our predictions are compared with the data points from Wojtak et al. (2011). The

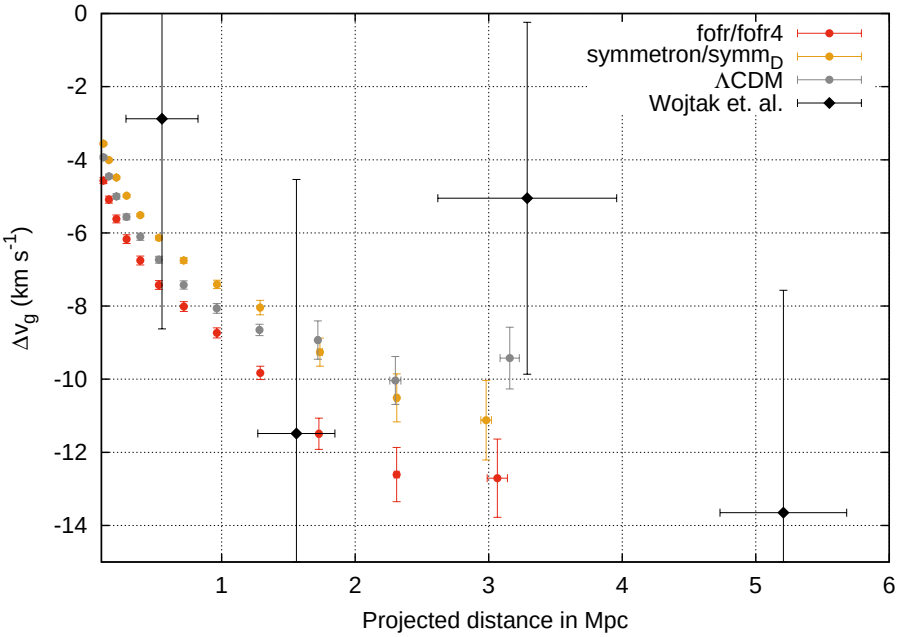

Figure 5.17: Comparison with the data points from Wojtak et al. (2011) of *fofr4* and *symm_D*.

	Number of galaxies			
Name	LRGs	ELGs	Time span	Reference
SDSS/BOSS	1.5×10^6	–	$2000 - 2014$	Aihara et al. (2011)
BigBOSS	3.5×10^6	15.5×10^6	$2017 - 2022$	Schlegel et al. (2009)
Euclid	–	50×10^6	$2020 - 2027$	Laureijs et al. (2011)

Table 5.1: Listing of the expected number of spectroscopically measuredluminous red galaxies (LRGs) and emission line galaxies (ELGs) in the full SDSS/BOSS, BigBOSS and Euclid surveys.

main point of this comparison (where even the most extreme models are compatible with the data), is to illustrate by how much the error bars have to be reduced in order to give viable constraints on screened modified gravity models. Croft (2013) shows error predictions for the full SDSS/BOSS (Aihara et al., 2011), BigBOSS (Schlegel et al., 2009) and Euclid (Laureijs et al., 2011) data sets (see Table 5.2). Accordingly, BigBOSS and Euclid should be able to map out the amplitude of the v_g curve with 6.5% and 4% precision, respectively. These values were obtained using a different technique than our approach, that is instead of taking the difference between the gravitational redshift of the central galaxy (BCG) and each particle in a cluster, the data was compared pairwise. Hence, they cannot be transferred directly. In addition, the binning of data in halo mass, which is necessary to detect signatures due to screened gravity, will naturally increase the error. Nevertheless, the planned new sky surveys will allow a restriction of the parameter space of some modified gravity models.

For the $f(R)$ Hu-Sawicky model the parameter space is already constrained beyond the parameters used in this work (see Table 5.2, left) and stronger limits obtained through gravitational redshift data are questionable. However, as the dark energy mystery is far from solved, it is important to test general relativity on kpc to Mpc scales. Gravitational redshift in combination with the upcoming sky surveys like Euclid are a potent tool to do that. For example, the symmetron model, which was also studied in this work, is hardly constrained yet (see Table 5.2, right) since it has a more efficient screening mechanism. Consequently, in order to constrain the parameter space of the symmetron model, the probing of cosmological scales is necessary.

Method	$\lvert f_{R0} - 1\rvert \lesssim$	Reference
Solar system	2×10^{-6}	Hu et. al (2007)
Strong lensing	2.5×10^{-6}	Smith (2009)
Cepheids	5×10^{-7}	Jain et al. (2012)

Parameter	Citation
$La_{assb}^{-3/2} \lesssim 10^{-3} H_0$	Hinterbichler et al. (2010)
$L \gg 1\,\mathrm{mm}$	Upadhye (2013)
$\beta \lesssim 1$	-[1]

Table 5.2: *Left:* Strongest existing constraints on the $f(R)$ Hu-Sawicky model. Shown are the upper bounds for $|f_{R0} - 1|$ with $n = 1$. *Right:* Order of magnitude "constraints" for the symmetron model.

1 A coupling varying greatly from unity will lead to no detectable effects at the lower end or too strong imprints in the mass power spectrum at the higher end.

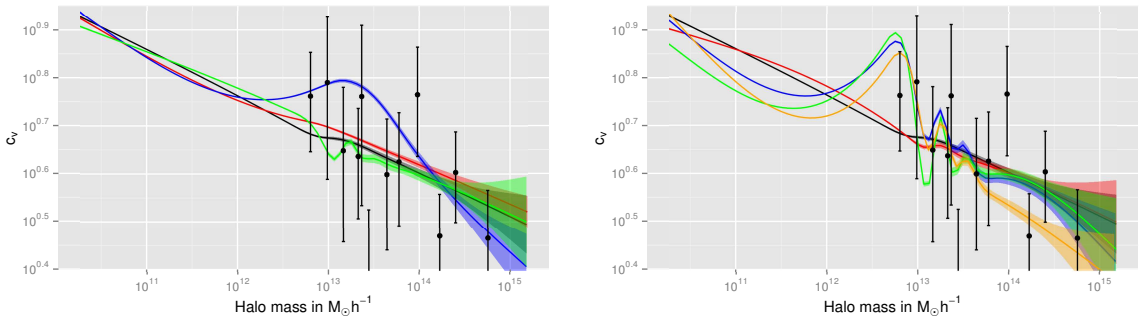

Figure 5.18: Mean of concentration value c_v versus halo mass with data points from Johnston & Sheldon (2007) (black points). In both plots, the shaded region shows the standard deviation and the black line the ΛCDM value. *Left panel: fofr4–6* (red, blue and green lines). *Right panel: symm_A–D* (red, blue, green and orange lines).

Of course, there are also other cluster properties that can be observed and used for testing modified gravity models. Llinares & Mota (2013b) used for example the ellipticity of clusters to constrain the symmetron and chameleon parameter space. With this observable they managed to exclude high β regions. Another commonly measured value is the concentration value of halos c_v which describes the breaking point of the radial density profile. In Fig. 5.18 this concentration value obtained by the `Rockstar` halo finder (Behroozi et al., 2013) through a NFW-fit on the density is compared against the data points from Johnston & Sheldon (2007) who used combined SDSS data of 130000 groups and clusters for the density fits. Also here, more precise measurements are necessary to be able to differ between the considered models or put additional constraints on the parameter space. A more detailed analysis of the change in concentration value in screened modified gravity models is left for future studies.

5.8 Systematic effects

The cluster density and redshift profiles obtained through simulations are affected by the following systematic effects:

(i) *Baryons:* Including baryonic effects inside clusters can lead to a flattening of the cluster density profile near the center. This is due to the movement of gas from the center to larger radii through active galactic nucleus feedback (Martizzi et al., 2011; Teyssier et al., 2010).

(ii) *Halo definition:* The definition of halo made in Sec. 3.4 was mainly aimed in getting the difference in gravitational potential between the brightest cluster galaxy (BCG) and the rest of the cluster and so imitating an observational standpoint. This is also why nearby subhalos where included in the definition of a halo. This can, however, be a problem as the minimum of the gravitational potential is not necessarily the densest central region. In order to verify the findings, the results were also reproduced by

taking the halo definition from the `Rockstar` halo finder and only minor deviations inside the virial radius were found.

(iii) *Halo finding process:* As discussed in Sec. 3.4 and Sec. 4.2, the definition of the virial radius depends on the mass of the halo in screened modified gravity. Therefore, the ΛCDM R_{200} results were compared against the R_{160} results of the most extreme (*fofr4*, *symm_D*) runs. The results were only slightly affected.

(iv) *Renormalization of the mass power spectra:* In order to be in agreement with other constraints the deviation from the ΛCDM mass power spectrum should only be on small scales. This was given for the set of parameters used in this work but for further exploration of the given parameter space the rescaling of σ_8 has to be taken into account.

(v) *Simulation systematics:* Llinares & Mota (2013a) showed that not taking the quasi-static approximation can result in different scalar field values and consequently also in different additional forces. The impact of this approximation is part of future studies. Against numerical problems, the implementation of the `ISIS` code was tested thoroughly in Llinares et al. (2013).

The analysis was performed assuming that these systematic effects are neglectable or beyond the scope of this work. A more detailed analysis would have to take these effects into account.

5.9 Summary of results

We performed a set of 8 high resolution simulation runs with 512^3 particles and a boxlength of $256\,\mathrm{Mpc\,h^{-1}}$ each. The data was used to analyze the density and gravitational redshift profiles of virialized clusters. For this purpose, first, the virialization parameter was computed for each halo with the inclusion of the scalar field energy. Furthermore, we calculated the gravitational redshift of all particles the following way: The value of the gravitational potential at the particle's position was subtracted from the halo's minimal gravitational potential. Ultimately, the modified gravity results could be compared to the ΛCDM values. These steps were not only undertaken for the gravitational redshift but also for the matter density, particle density, fifth force and velocity dispersion. These quantities allowed us to analyze and reason the gravitational redshift results. The overall finding from the numerical results is that in both analyzed models the deviation from ΛCDM can vary enormously depending on the choice of parameters and the analyzed halo size.

$f(R)$ results

The $f(R)$ results confirmed that lowering $|f_{R0}-1|$ reduces the deviation from ΛCDM. In the data sets we found an enhanced clustering mainly in the central regions of the halos. This causes an increase in gravitational redshift with respect to the ΛCDM results. The intensity

of this additional clustering – and, thus, the deviation in gravitational redshift – was shown to be highly dependent on the halo mass. In addition, a relationship between the size of the maximal affected clusters and the f_{R0} parameter could be established: The lower the value of $|f_{R0} - 1|$, the smaller are the affected halos. This is due to the chameleon nature of the fifth force: Very small halos are deep inside the "thick shell regime" and, therefore, the minimum of the effective potential is hardly varied. Hence, only a small fifth force arises. On the other hand, very big halos possess a "thin shell", that is the fifth force is fully self-screened within the halo. The characteristic halo mass range is between these two regimes and marks when the fifth force is strongest.

Symmetron results

In three of the four symmetron runs made a_{ssb} was changed. This parameter controls the time of symmetry breaking and the strength of the fifth force. In one run the coupling constant β was varied instead.

As expected a lower value of a_{ssb} or a higher value of β results in a generally greater deviation from the ΛCDM cluster profiles. The effect was in some cases contrary to the expectation: Instead of stronger clustering in the center of the halo, we found effective negative clustering leading to a negative deviation in gravitational redshift. This shifted clustering can be understood by analyzing the dependency of the fifth force versus the halo mass and the distance from the center of the cluster by keeping in mind that the analysis is made withing a certain cluster mass bin. The simple explanation attempt made is based on the idea that through the possible screening of the fifth force in the central regions a de-facto preferred mass density exists. This means, once the mass density inside the center is higher the clustering takes place in the outer regions.

There are indications of the same effect in other data sets analyzed during this work. However, this would have to be further investigated using a wider parameter range and simulation snapshots at higher redshifts allowing the analysis of the cluster formation process.

Highlights and comparison

All of the analyzed models show an increased clustering rate which can most easily be observed in the matter power spectra (Fig. 5.4 and Fig. 5.11). This effect due to the additional force is not surprising and was shown already using N-body simulations in previous work (Brax et al., 2012, 2013; Li et al., 2012).

The most common expectation about the change of the gravitational redshift through this additional clustering is to observe an enhanced signal. This idea is motivated by the fact that additional clustering should lead to deeper potential wells and, hence, to a stronger gravitational redshift signal. This is the major imprint observed in the $f(R)$ models studied and the same behavior was expected in the symmetron models. However, depending on the halo mass and model parameters, the matter density can be enhanced in the outskirts of the halo. In such a way altered halo density profiles in modified gravity N-body simulations

were already observed by Baldi (2011). For some parameters they obtained an increased clustering in the center of the halo, while for others this additional clustering took place at larger radii. Keeping in mind the halo mass is effectively fixed in one mass bin, this result is not surprising as missing mass in one region has to be compensated by additional mass in another region. Such an altered halo density profile means the potential well becomes shallower in the central regions and a deeper in the outskirts. Consequently, the resulting deviation in gravitational redshift is negative.

However, this connection between clustering in the central regions and stronger gravitational redshift or clustering in the outer regions and a negative deviation does not explain the contrary imprint obtained for various parameter sets. Therefore, the question we tried to answer is, what mechanism controls if the clustering happens in the central region or not?

The explanation provided is based on the nature of the screening mechanism: If the fifth force is screened in the central regions of a halo but not in the outskirts, then this is where the additional clustering will take place. Another way of phrasing it is that each set of model parameters results in a "preferred density", that is a matter density for which the fifth force is just screened. This reasoning can most easily be tested by observing the dependency of the fifth force (see Fig. 5.12) and the deviation of the gravitational redshift (Fig. 5.13) for the *symm_D* model since the screening is active in the central region. However, the explanation is supported by several additional features in the results: By lowering a_{ssb} the effect should still persist in a weaker form – which it does in the *symm_B* data set. Here, clustering the center is effectively weakened for clusters with mass $\gtrsim 10^{13.5} M_\odot h^{-1}$. Consequently, gravitational redshift is decreased in these halos, too. For even smaller values of a_{ssb}, the additional force is too small and the existence of the same effect cannot be confirmed. A special position is taken by the *fofr4* data: The increase of the number of massive clusters is immense (Fig. 5.4) suggesting the same or even stronger merging of clusters. On the other hand, the force enhancement close to the center has not yet reached its maximum, even for the largest halos of the data sample (top left panel of Fig. 5.5) opposed to the *symm_D* case, where this maximum lies around $10^{13}\, M_\odot h^{-1}$ for $R \approx 0.1\, R_v$ (Fig. 5.12). This means, in the *fofr4* the "effective preferred density" is even higher than the one present in the central parts of the biggest clusters. Therefore, the clustering is dominant in the central parts, leading to a higher gravitational redshift as seen in Fig. 5.6. It is more appropriate to compare the *symm_D* with the *fofr5* results due to their bigger similarity in the fifth force profiles. The fifth acceleration in the central region is, however, more present for halos in the mass range $10^{13.5} - 10^{14} M_\odot h^{-1}$ in the *fofr5* data. For the next bigger halos, $\ddot{\mathbf{x}}_{\mathrm{Fifth}}$ is neglectable in the central regions in both models. This could explain the resulting positive deviation in gravitational redshift for the first halo mass bin and the negative deviation in the second (Fig. 5.6). Of course, the different other characteristics of the symmetron and the chameleon model (e.g. the time dependence of the fifth force) have to be taken into account if the data is to be analyzed in more detail. This explanation provided can, after all, clarify the partial contrary results obtained.

6

Conclusions

The main goal of the thesis was to study gravitational redshift profiles of virialized halos in both the symmetron model and chameleon $f(R)$-gravity using N-body simulations. This required several sub-steps, which can be split into three categories: Firstly, the extraction of data from the simulation output; secondly, the identification and definition of a halo and thirdly the question whether a halo is virialized or not.

The gravitational redshift as well as other particle related quantities, such as the acceleration due to the additional force, that were used to explain the results were calculated directly from the N-body simulation. This allowed the straightforward extraction of the gravitational redshift profiles.

In order to obtain the state of virialization, several methods were analyzed and the most adequate one – using the total acceleration of the particles – was employed. This allowed us to calculate the virialization parameter taking the energy of the scalar field into account.

Furthermore, the spherical collapse model was utilized to test if the common halo definition with a fixed density contrast value leading to R_{200} or similar is applicable for screened modified gravity models. The conclusion is mixed as, on the one hand, we found the density contrast value to vary significantly with halo mass. On the other hand, effects like environmental screening have not been taken into account. Therefore, we expect this effect to have a minor impact on the final results. A more detailed analysis of this problem has to be carried out and is subject of future work.

We found the results to be highly dependent on the halo mass, which means the consideration of multiple mass ranges is crucial when analyzing observational data. In particular, three possible regimes were identified:

(i) *No deviation from ΛCDM.* If the halo is fully screened (either through self-screening or environmental screening) or is too small to affect the scalar field, no deviation in the density and, consequently, neither in the gravitational redshift profiles was observed.

(ii) *Enhanced gravitational redshift.* This is the expected result as the fifth force leads to additional clustering in the center of the halo. Additional matter in the central region means a deeper potential well and, therefore, a positive deviation compared to ΛCDM.

(iii) *Weaker gravitational redshift.* If the fifth force is screened in the central region of the halo but not in the outskirts, a negative deviation can appear. The additional force leads to a matter overdensity in the outer regions while – with respect to the halo mass – the inner regions are less dense than in the ΛCDM case.

This shows, that simply assuming the change of the gravitational redshift is equal to the maximum possible change of the gravitational constant, as done frequently when predictions are made, is not sufficient. Instead, the prediction obtained by N-body simulations as in this work should be used.

Finally, the results were compared with existing observational data, mainly to show that only future surveys may allow the exclusion of certain models or the restriction of the parameter space. This topic is referred to in the next section.

6.1 Outlook

As previously mentioned, thanks to the planned next generation experiments like BigBOSS (start in 2017) and Euclid (expected launch 2020), which will cover ten to fifty times more galaxies than the full SDSS survey (completed in 2014), gravitational redshift will become an observationally important tool besides lensing. This quantitative and qualitative improvement offered by the new surveys, will automatically lead to a higher signal to noise ratio. Naturally, the numerous additional effects described by Kaiser (2013) and Zhao et al. (2012) have to be taken into account as well in order to avoid systematic errors. The third point on the observational side will be the combination of data with other measurements as pointed out by Croft (2013) to determine the matter of the object. All these factors will eventually lead to high-precision measurements that can be used to exclude alternative models of gravity and establish further constraints.

Before these future goals can be achieved, more work has to be done on the numerical side. A major part will be to map out the parameter space of various modified gravity models. In order to reduce the computing cost, this can be done by using the spherical collapse model to extrapolate data obtained from N-body simulations beyond the simulation parameters. For this purpose a proper framework using excursion set theory has to be set up as done by Lombriser et al. (2013) for the Hu-Sawicky model. Another question that has to be addressed when using mock data sets is finding the optimal gravitational redshift estimator and binning technique to improve the signal to noise ratio. The last point worth mentioning is the obviously improvable simulation setup, as a higher resolution and added baryonic effects can show hidden features in the low-mass end.

A

Appendix

A.1 Derivation of the Klein-Gordon equation

Varying the the action of a free scalar field given by (Fujii & Maeda, 2007)

$$S_\phi = -\int \mathrm{d}^4x\sqrt{-g}\left\{\frac{1}{2}\partial_\mu\phi\partial^\mu\phi + V(\phi)\right\} \tag{A.1}$$

with respect to ϕ results in

$$\begin{aligned}
\delta S &= -\int \mathrm{d}^4x\sqrt{-g}\left\{\frac{1}{2}\delta\left(\nabla_\mu\phi\nabla^\mu\phi\right) + V_{,\phi}\delta\phi\right\} && \text{(A.2)}\\
&= -\int \mathrm{d}^4x\sqrt{-g}\left\{\nabla_\mu\phi\nabla^\mu\delta\phi + V_{,\phi}\delta\phi\right\} && \text{(A.3)}\\
&= -\int \mathrm{d}^4x\sqrt{-g}\left\{-\nabla_\mu\nabla^\mu\phi\delta\phi + \nabla^\mu\left[\nabla_\mu\phi\delta\phi\right] + V_{,\phi}\delta\phi\right\} && \text{(A.4)}\\
&= -\int \mathrm{d}^4x\sqrt{-g}\left\{-\Box\phi + V_{,\phi}\right\}\delta\phi\ . && \text{(A.5)}
\end{aligned}$$

Where the second term in (A.4) vanishes due to Gauss' theorem if $\delta\phi$ is zero at the boundaries.

Demanding $\delta S = 0$ results in the Klein-Gordon equation

$$\Box\phi - V_{,\phi}(\phi) = 0\ . \tag{A.6}$$

A.2 Gauss Seidel method with successive overrelaxation

The idea behind mesh relaxation is that a matrix equation of the form

$$\mathbf{A}\boldsymbol{y} = \mathbf{q}\ , \tag{A.7}$$

with $\mathbf{A}$ being a matrix and $\boldsymbol{y}$ and $\mathbf{q}$ are vectors is solved using the decomposition of the matrix $\mathbf{A}$

$$\mathbf{A} = \mathbf{B} + \mathbf{R} \,, \tag{A.8}$$

where B is easily invertible. The equation can then be rearranged resulting in

$$\boldsymbol{y} = \mathbf{B}^{-1}\mathbf{q} + \mathbf{M}\boldsymbol{y} \,. \tag{A.9}$$

The matrix $\mathbf{M} = -\mathbf{B}^{-1}(\mathbf{A} - \mathbf{B})$ is usually denoted as iteration matrix.

Mesh relaxation works by starting with an initial guess $\boldsymbol{y}^{(0)}$ and iterating from $t = 0$ to t_c when some convergence criteria is fulfilled using

$$\boldsymbol{y}^{(t+1)} = \mathbf{B}^{-1}\mathbf{q} + \mathbf{M}\boldsymbol{y}^{(t)} \,. \tag{A.10}$$

Convergence towards the exact solution $\boldsymbol{y}$ can be shown (Hockney & Eastwood, 1988) defining the error

$$\boldsymbol{\varepsilon}^{(t)} = \boldsymbol{y}^{(t)} - \boldsymbol{y} \,. \tag{A.11}$$

Substituting this back in (A.10) and noting that (A.9) is fulfilled leaves

$$\boldsymbol{\varepsilon}^{(t)} = \mathbf{M}\boldsymbol{\varepsilon}^{(t-1)} = \mathbf{M}^t\boldsymbol{\varepsilon}^{(0)} \,. \tag{A.12}$$

The equation can also be generalized to a variable $\mathbf{M}$ by replacing $\mathbf{M}^t$ with $\mathbf{M}^{(t)}$:

$$\boldsymbol{\varepsilon}^{(t)} = \mathbf{M}\boldsymbol{\varepsilon}^{(t-1)} = \mathbf{M}^{(t)}\boldsymbol{\varepsilon}^{(0)} \tag{A.13}$$

The error $||\boldsymbol{\varepsilon}^{(t)}|| = \sum_i \boldsymbol{\varepsilon}_i^{(t)}\boldsymbol{\varepsilon}_i^{(t)}$ converges iff the greatest absolute eigenvalue of the matrix $||\mathbf{M}^{(t)}||$ is smaller than 1 for all times bigger than some arbitrary time. This can be seen by taking the norm of Eq. (A.13) and noting that the euclidean (L_2) norm of a matrix is its greatest absolute eigenvalue (Horn & Johnson, 1985):

$$\frac{||\boldsymbol{\varepsilon}^{(t)}||}{||\boldsymbol{\varepsilon}^{(0)}||} \leq ||\mathbf{M}^{(t)}|| = \max\left(\lambda_i^{(t)}\right) \,. \tag{A.14}$$

In the algorithm the matrices $\mathbf{A}$, $\mathbf{B}$ or $\mathbf{M}^{(t)}$ are never actually stored or inverted. For a differential equation - as the Poisson equation - finite difference aproximations are used. E.g. a general two dimensional Laplacian can be aproximated as

$$\nabla^2 f(x,y)\Big|_{\substack{x=x_0\\y=y_0}} \approx \frac{f(x_0-h,y_0) + f(x_0,y_0-h) + f(x_0+h,y_0) + f(x_0,y_0-h) - 4f(x_0,y_0)}{h^2} \,. \tag{A.15}$$

This results in matrix notation for Poisson equation in comoving coordinates Eq. (3.17) on a two dimensional uniform mesh:

$$\tilde{y}_{i,j}^{(t)} = \frac{h^2}{4}\left[y_{i-1,j}^{(t)} + y_{i,j-1}^{(t)} + y_{i+1,j}^{(t)} + y_{i,j+1}^{(t)} - \pi G(\rho'_{i,j} - \rho_0)\right] \tag{A.16}$$

the factors may differ in other applications like non-uniform grids or more dimensional systems.

For the Gauss Seidel method the original matrix **A** is decomposed in a lower triangular part (for **B**) which is easily invertible and the rest, a stricly upper triangular part (for R). After each timestep the new value for is simply

$$y_{i,j}^{(t+1)} = \tilde{y}_{i,j}^{(t)} \ . \tag{A.17}$$

Originally this method only converges certainly if the matrix **A** is diagonally dominant or symmetric positive definite (but may also converge for other cases) (Hockney & Eastwood, 1988).

Therefore - and to decrease the convergence time dramatically - equation (A.17) is altered. Instead of simply taking $\tilde{y}_{i,j}^{(t)}$ as the new value this trend is "over relaxed" to anticipate future changes (Hockney & Eastwood, 1988):

$$y_{i,j}^{\text{new}} = \omega \tilde{y}_{i,j}^{(t)} + (1-\omega) y_{i,j}^{(t)} \text{ with } 1 < \omega < 2 \tag{A.18}$$

This procedure is knows as successive overrelaxation and is controled via the the relaxation factor ω. A value of $\omega = 1$ corresonds to the simple GS method and a value of

$$\omega = \frac{2}{1 + \sqrt{1-\rho^2}} \tag{A.19}$$

is optimal – given the greatest absolute Eigenvalue (spectral radius) of the Jacobi matrix ρ (Hockney & Eastwood, 1988). In `RAMSES` a value of

$$\omega = \frac{2}{1 + \pi/\bar{L}} \ , \tag{A.20}$$

where $\bar{L}$ is the average patch size is used in the `RAMSES` code (Teyssier, 2002).

Bibliography

Aihara, H., Allende Prieto, C., An, D., Anderson, S. F., Aubourg, É., Balbinot, E., Beers, T. C., Berlind, A. A., Bickerton, S. J., Bizyaev, D., Blanton, M. R., Bochanski, J. J., Bolton, A. S., Bovy, J., Brandt, W. N., Brinkmann, J., Brown, P. J., Brownstein, J. R., Busca, N. G., et al. Apr. 2011, *The Eighth Data Release of the Sloan Digital Sky Survey: First Data from SDSS-III*, ApJS, **193**, 29,p. 29

Amendola, L & Tsujikawa, S: *Dark energy: Theory and observations*. Cambridge University Press, 2010

Appleby, S. & Battye, R. Oct. 2007, *Do consistent F(R)F(R) models mimic general relativity plus Λ?*, Physics Letters B, **654**,pp. 7–12

Armendariz-Picon, C, Mukhanov, V & Steinhardt, P. 2000, *Dynamical solution to the problem of a small cosmological constant and late-time cosmic acceleration*, Physical Review Letters

Baldi, M. 2011, *Time-dependent couplings in the dark sector: from background evolution to non-linear structure formation*, Monthly Notices of the Royal Astronomical Society, **27**.February,pp. 1–27

Barnes, J. & Hut, P. Dec. 1986, *A hierarchical O(N log N) force-calculation algorithm*, Nature, **324**,pp. 446–449

Behroozi, P. S., Wechsler, R. H. & Wu, H.-Y. Jan. 2013, *The Rockstar Phase-Space Temporal Halo Finder and the Velocity Offsets of Cluster Cores*, The Astrophysical Journal, **762**.2,p. 109

Bekenstein, J. D. & Sanders, R. H. Mar. 2012, *TeVeS/MOND is in harmony with gravitational redshifts in galaxy clusters*, Monthly Notices of the Royal Astronomical Society: Letters, **421**.1,pp. L59–L61

Bertschinger, E. June 2011, *GRAFIC-2: Multiscale Gaussian Random Fields for Cosmological Simulations*, Astrophysics Source Code Library,p. 6008

Bertschinger, E. Sept. 1998, *Simulations of Structure Formation in the Universe*, Annual Review of Astronomy and Astrophysics, **36**.1,pp. 599–654

Birdsall, C. K. & Fuss, D. Apr. 1969, *Clouds-in-Clouds, Clouds-in-Cells, Physics for Many-Body Plasma Simulation*, Journal of Computational Physics, **3**,p. 494

Bondi, H. 1947, *Spherically symmetrical models in general relativity*, MNRAS, **107**,p. 410

Bouchet, F. R. & Hernquist, L. Dec. 1988, *Cosmological simulations using the hierarchical tree method*, ApJS, **68**,pp. 521–538

Brans, C. & Dicke, R. H. Nov. 1961, *Mach's Principle and a Relativistic Theory of Gravitation*, Phys. Rev. **124**, (3),pp. 925–935

Brax, P., Bruck, C van de & Davis, A. 2004, *Detecting dark energy in orbit: The cosmological chameleon*, Physical Review D,pp. 1–31

Brax, P., Bruck, C. V. D., Davis, A. & Shaw, D. 2008, *f (R) gravity and chameleon theories*, Physical Review D,pp. 1–18

Brax, P., Bruck, C. van de, Davis, A.-C. & Shaw, D. Sept. 2010a, *Dilaton and modified gravity*, Physical Review D, **82**.6,p. 063519

Brax, P., Rosenfeld, R & Steer, D. Aug. 2010b, *Spherical collapse in chameleon models*, Journal of Cosmology and Astroparticle Physics, **2010**.08,pp. 033–033

Brax, P., Davis, A.-C., Li, B., Winther, H. A. & Zhao, G.-B. June 2012, *Systematic simulations of modified gravity: symmetron and dilaton models*, arXiv preprint arXiv:1206.3568,p. 30

Brax, P., Davis, A., Li, B., Winther, H. & Zhao, G. 2013, *Systematic simulations of modified gravity: chameleon models*, arXiv preprint arXiv:1303.0007v2,pp. 1–16

Bryan, G. L. & Norman, M. L. Mar. 1998, *Statistical Properties of X-Ray Clusters: Analytic and Numerical Comparisons*, ApJ, **495**,pp. 80–99

Cappi, A 1995, *Gravitational redshift in galaxy clusters.*, Astronomy and Astrophysics

Carretta, E., Gratton, R. G., Clementini, G. & Fusi Pecci, F. Apr. 2000, *Distances, Ages, and Epoch of Formation of Globular Clusters*, ApJ, **533**,pp. 215–235

Carroll, S. M. Oct. 1998, *Quintessence and the Rest of the World: Suppressing Long-Range Interactions*, Physical Review Letters, **81**,pp. 3067–3070

Carroll, S.: *Spacetime and geometry: an introduction to general relativity*. Addison-Wesley Longman, Incorporated, 2004

Chandrasekhar, S: *Hydrodynamic and hydromagnetic stability*. Dover Publications, Incorporated, 1981

Clifton, T., Ferreira, P. G., Padilla, A. & Skordis, C. Mar. 2012, *Modified gravity and cosmology*, Physics Reports, **513**.1-3,pp. 1–189

Cole, S & Lacey, C July 1996, *The structure of dark matter haloes in hierarchical clustering models*, Monthly Notices of the Royal Astronomical Society, **281**.2,pp. 716–736

Colombi, S., Jaffe, A., Novikov, D. & Pichon, C. Feb. 2009, *Accurate estimators of power spectra in N -body simulations*, Monthly Notices of the Royal Astronomical Society, **393**.2,pp. 511–526

Cooley, J. & Tukey, J. 1965, *An algorithm for the machine calculation of complex Fourier series*, Mathematics of computation,pp. 297–301

Couchman, H. M. P. Feb. 1991, *Mesh-refined P3M - A fast adaptive N-body algorithm*, ApJ, **368**,pp. L23–L26

Croft, R. 2013, *Gravitational redshifts from large-scale structure*, arXiv preprint arXiv:1304.4124, April

Davis, A., Li, B. & Mota, D. 2011, *Structure Formation in the Symmetron Model*, Arxiv preprint arXiv:1108.3081

Davis, M., Efstathiou, G., Frenk, C. S. & White, S. D. M. May 1985, *The evolution of large-scale structure in a universe dominated by cold dark matter*, ApJ, **292**,pp. 371–394

de Blok, W. J. G. 2010, *The Core-Cusp Problem*, Advances in Astronomy, **2010**, 789293

Dehnen, W. & Read, J. 2011, *N-body simulations of gravitational dynamics*, The European Physical Journal Plus,pp. 1–28

Diemand, J., Kuhlen, M. & Madau, P. Sept. 2006, *Early Supersymmetric Cold Dark Matter Substructure*, ApJ, **649**,pp. 1–13

Dodelson, S.: *Modern cosmology*. Academic Press. Academic Press, 2003

Efstathiou, G. & Eastwood, J. W. Feb. 1981, *On the clustering of particles in an expanding universe*, MNRAS, **194**,pp. 503–525

Engineer, S., Kanekar, N. & Padmanabhan, T. May 2000, *Non-linear density evolution from an improved spherical collapse model*, Monthly Notices of the Royal Astronomical Society, **314**.2,pp. 279–289

Everitt, B & Skrondal, A: *The Cambridge dictionary of statistics*. Third Edit. Cambridge University Press, 2002

Ewald, P. P. 1921, *Die Berechnung optischer und elektrostatischer Gitterpotentiale*, Annalen der Physik, **369**.3,pp. 253–287

Faraoni, V., Gunzig, E. & Nardone, P. 1998, *Conformal transformations in classical gravitational theories and in cosmology*, arXiv preprint gr-qc/9811047

Ferraro, S., Schmidt, F. & Hu, W. 2011, *Cluster abundance in f (R) gravity models*, Physical Review D, **1**,pp. 1–8

Forero-Romero, J. E., Gottlöber, S. & Yepes, G. Dec. 2010, *Bullet Clusters in the Marenostrum Universe*, The Astrophysical Journal, **725**.1,pp. 598–604

Fujii, Y. & Maeda, K.: *The Scalar-Tensor Theory of Gravitation*. Cambridge University Press, 2007

Gottloeber, S. 1998, *Galaxy Tracers in Cosmological N-Body Simulations*. In: *Large Scale Structure: Tracks and Traces*. Ed. by V. Mueller, S. Gottloeber, J. P. Muecket & J. Wambsganss. 1998, pp. 43–46

Gunn, J. & Gott, J. 1972, *On the infall of matter into clusters of galaxies and some effects on their evolution*, The Astrophysical Journal

Habib, S., Pope, A., Lukić, Z., Daniel, D., Fasel, P., Desai, N., Heitmann, K., Hsu, C.-H., Ankeny, L., Mark, G., Bhattacharya, S. & Ahrens, J. July 2009, *Hybrid petacomputing meets cosmology: The Roadrunner Universe project*, Journal of Physics Conference Series, **180**.1,p. 012019

Hansen, B. M. S., Brewer, J., Fahlman, G. G., Gibson, B. K., Ibata, R., Limongi, M., Rich, R. M., Richer, H. B., Shara, M. M. & Stetson, P. B. Aug. 2002, *The White Dwarf Cooling Sequence of the Globular Cluster Messier 4*, ApJ, **574**,pp. L155–L158

Hartle, J.: *Gravity: an introduction to Einstein's general relativity*. Addison-Wesley, 2003

Hernquist, L. Aug. 1987, *Performance characteristics of tree codes*, ApJS, **64**,pp. 715–734

Hinterbichler, K. & Khoury, J. June 2010, *Screening Long-Range Forces through Local Symmetry Restoration*, Physical Review Letters, **104**.23,p. 231301

Hinterbichler, K., Khoury, J., Levy, A. & Matas, A. 2011, *Symmetron cosmology*, Physical Review D

Hockney, R. W., Goel, S. P. & Eastwood, J. W. Feb. 1974, *Quiet High-Resolution Computer Models of a Plasma*, Journal of Computational Physics, **14**,p. 148

Hockney, R. & Eastwood, J.: *Computer simulation using particles*. Taylor & Francis, 1988

Horn, R. A. & Johnson, C. R.: *Matrix analysis*. Cambridge University Press, 1985

Hu, W. & Sawicki, I. 2007, *Models of f (R) cosmic acceleration that evade solar system tests*, Physical Review D,pp. 1–13

Jain, B., Vikram, V. & Sakstein, J. Apr. 2012, *Astrophysical Tests of Modified Gravity: Constraints from Distance Indicators in the Nearby Universe*,p. 37

Jessop, C., Duncan, M. & Chau, W. Y. Dec. 1994, *Multigrid Methods for N-Body Gravitational Systems*, Journal of Computational Physics, **115**,pp. 339–351

Johnston, D. & Sheldon, E. 2007, *Cross-correlation Weak Lensing of SDSS galaxy Clusters II: Cluster Density Profiles and the Mass–Richness Relation*, arXiv preprint arXiv:0709.1159v1

Kaiser, N. 2013, *Measuring Gravitational Redshifts in Galaxy Clusters*, arXiv preprint arXiv:1303.3663, **000**.March

Khoury, J. & Weltman, A. 2004a, *Chameleon cosmology*, Physical Review D

– 2004b, *Chameleon fields: Awaiting surprises for tests of gravity in space*, Physical review letters

Kim, Y.-R. Y.-r. & Croft, R. A. C. May 2004, *Gravitational Redshifts in Simulated Galaxy Clusters*, The Astrophysical Journal, **607**.1,pp. 164–174

Klypin, A., Gottlöber, S., Kravtsov, A. V. & Khokhlov, A. M. May 1999, *Galaxies in N-Body Simulations: Overcoming the Overmerging Problem*, ApJ, **516**,pp. 530–551

Klypin, A. A. & Shandarin, S. F. Sept. 1983, *Three-dimensional numerical model of the formation of large-scale structure in the Universe*, MNRAS, **204**,pp. 891–907

Knebe, A., Green, A. & Binney, J. Aug. 2001, *Multi-level adaptive particle mesh (MLAPM): a c code for cosmological simulations*, MNRAS, **325**,pp. 845–864

Knebe, A., Kravtsov, A. V., Gottlober, S. & Klypin, A. a. Sept. 2000, *On the effects of resolution in dissipationless cosmological simulations*, Monthly Notices of the Royal Astronomical Society, **317**.3,pp. 630–648

Knebe, A., Knollmann, S. R., Muldrew, S. I., Pearce, F. R., Aragon-Calvo, M. A., Ascasibar, Y., Behroozi, P. S., Ceverino, D., Colombi, S., Diemand, J., Dolag, K., Falck, B. L., Fasel, P., Gardner, J., Gottlöber, S., Hsu, C.-H., Iannuzzi, F., Klypin, A., Lukić, Z., et al. Aug. 2011, *Haloes gone MAD: The Halo-Finder Comparison Project*, Monthly Notices of the Royal Astronomical Society, **415**.3,pp. 2293–2318

Knebe, A., Pearce, F. & Lux, H. 2013, *Structure Finding in Cosmological Simulations: The State of Affairs*, arXiv preprint arXiv:1304.0585v1, **42**.April,pp. 1–42

Knollmann, S. R. & Knebe, A. June 2009, *AHF: Amiga's Halo Finder*, ApJS, **182**,pp. 608–624

Kravtsov, A. V., Klypin, A. A. & Khokhlov, A. M. July 1997, *Adaptive Refinement Tree: A New High-Resolution N -Body Code for Cosmological Simulations*, The Astrophysical Journal Supplement Series, **111**.1,pp. 73–94

Kuhlen, M., Vogelsberger, M. & Angulo, R. Nov. 2012, *Numerical simulations of the dark universe: State of the art and the next decade*, Physics of the Dark Universe, **1**.1-2,pp. 50–93

Lahav, O., Lilje, P. B., Primack, J. R. & Rees, M. J. 1991, *Dynamical effects of the cosmological constant*, Monthly Notices of the ...

Larson, D., Dunkley, J., Hinshaw, G., Komatsu, E., Nolta, M. R., Bennett, C. L., Gold, B., Halpern, M., Hill, R. S., Jarosik, N., Kogut, A., Limon, M., Meyer, S. S., Odegard, N., Page, L., Smith, K. M., Spergel, D. N., Tucker, G. S., Weiland, J. L., et al. Feb. 2011, *Seven-year Wilkinson Microwave Anisotropy Probe (WMAP) Observations: Power Spectra and WMAP-derived Parameters*, ApJS, **192**, 16,p. 16

Laureijs, R, Amiaux, J, Arduini, S, Augueres, J. L., Brinchmann, J., Cole, R., Cropper, M., Dabin, C., Duvet, L., Ealet, A., Garilli, B., Gondoin, P., Guzzo, L., Hoar, J., Hoekstra, H., Holmes, R., Kitching, T., Maciaszek, T., Mellier, Y., et al. Oct. 2011, *Euclid Definition Study Report*, arXiv preprint arXiv:1110.3193, July,p. 116

Lee, E. & Forthofer, R.: *Analyzing Complex Survey Data*. Analyzing Complex Survey Data. SAGE Publications, 2006

Li, B. & Efstathiou, G. Apr. 2012, *An extended excursion set approach to structure formation in chameleon models*, Monthly Notices of the Royal Astronomical Society, **421**.2,pp. 1431–1442

Li, B., Hellwing, W. A., Koyama, K., Zhao, G.-B., Jennings, E. & Baugh, C. M. Oct. 2012, *The non-linear matter and velocity power spectra in f(R) gravity*, Monthly Notices of the Royal Astronomical Society, **428**.1,pp. 743–755

Li, Y. & Hu, W. 2011, *Chameleon halo modeling in f (R) gravity*, Physical Review D, 1,pp. 1–7

Llinares, C. & Mota, D. F. Apr. 2013a, *Releasing Scalar Fields: Cosmological Simulations of Scalar-Tensor Theories for Gravity Beyond the Static Approximation*, Physical Review Letters, **110**.16,p. 161101

– Apr. 2013b, *Shape of Clusters of Galaxies as a Probe of Screening Mechanisms in Modified Gravity*, Physical Review Letters, **110**.15,p. 151104

Llinares, C., Mota, D. F. & Winther, H. A. 2013, *Isis : a new N-body cosmological code with scalar fields based on Ramses*, (in preparation)

Lokas, E. L. & Mamon, G. a. Feb. 2001, *Properties of spherical galaxies and clusters with an NFW density profile*, Monthly Notices of the Royal Astronomical Society, **321**.1,pp. 155–166

Lombriser, L., Schmidt, F., Baldauf, T., Mandelbaum, R., Seljak, U. & Smith, R. May 2012, *Cluster density profiles as a test of modified gravity*, Physical Review D, **85**.10,p. 102001

Lombriser, L., Li, B., Koyama, K. & Zhao, G. 2013, *Modeling halo mass functions in chameleon f (R) gravity*, arXiv preprint arXiv:1304.6395,pp. 1–11

Ludlow, A. D., Navarro, J. F., Boylan-Kolchin, M., Bett, P. E., Angulo, R. E., Li, M., White, S. D. M., Frenk, C. & Springel, V. Feb. 2013, *The Mass Profile and Accretion History of Cold Dark Matter Halos*, arXiv preprint arXiv:1302.0288, **000**.February,p. 12

Maor, I. & Lahav, O. July 2005, *On virialization with dark energy*, Journal of Cosmology and Astroparticle Physics, **2005**.07,pp. 003–003

Martin, J. 2012, *Everything You Always Wanted To Know About The Cosmological Constant Problem (But Were Afraid To Ask)*

Martizzi, D., Teyssier, R., Moore, B. & Wentz, T. 2011, *The effects of baryon physics, black holes and AGN feedback on the mass distribution in clusters of galaxies*, arXiv preprint arXiv:1112.2752, **000**.April

Mateo, M. L. 1998, *Dwarf Galaxies of the Local Group*, ARA&A, **36**,pp. 435–506

Misner, C., Thorne, K. & Wheeler, J.: *Gravitation:* Physics Series poeng 3. W. H. Freeman, 1973

Mota, D. & Bruck, C van de 2004, *On the spherical collapse model in dark energy cosmologies*, Astronomy and Astrophysics, **81**,pp. 71–81

Navarro, J. F., Frenk, C. S. & White, S. D. M. Dec. 1995, *Simulations of X-ray clusters*, Monthly Notices of the Royal Astronomical Society

– May 1996, *The Structure of Cold Dark Matter Halos*, The Astrophysical Journal, **462**,p. 563

– 1997, *A Universal density profile from hierarchical clustering*, The Astrophysical Journal, **1**.1,pp. 493–508

Oguri, M., Bayliss, M. B., Dahle, H. k., Sharon, K., Gladders, M. D., Natarajan, P., Hennawi, J. F. & Koester, B. P. Mar. 2012, *Combined strong and weak lensing analysis of 28 clusters from the Sloan Giant Arcs Survey*, Monthly Notices of the Royal Astronomical Society, **420**.4,pp. 3213–3239

Okabe, N., Smith, G. & Umetsu, K. 2013, *LoCuSS: The Mass Density Profile of Massive Galaxy Clusters at z= 0.2*, arXiv preprint arXiv:1302.2728v1, **1**,pp. 1–6

Olive, K. & Pospelov, M. 2008, *Environmental dependence of masses and coupling constants*, Physical Review D, September

Oyaizu, H. 2008, *Nonlinear evolution of f (R) cosmologies. I. Methodology*, Physical Review D

Perlmutter, S., Aldering, G., Goldhaber, G., Knop, R. A., Nugent, P., Castro, P. G., Deustua, S., Fabbro, S., Goobar, A., Groom, D. E., Hook, I. M., Kim, A. G., Kim, M. Y., Lee, J. C., Nunes, N. J., Pain, R., Pennypacker, C. R., Quimby, R., Lidman, C., et al. June 1999, *Measurements of Omega and Lambda from 42 High-Redshift Supernovae*, ApJ, **517**,pp. 565–586

Planck Collaboration, Ade, P. A. R., Aghanim, N., Armitage-Caplan, C., Arnaud, M., Ashdown, M., Atrio-Barandela, F., Aumont, J., Baccigalupi, C., Banday, A. J. & al., et Mar. 2013, *Planck 2013 results. XVI. Cosmological parameters*, ArXiv e-prints

Press, W., Flannery, B., Teukolsky, S. & Vetterling, W.: *Numerical Recipes in FORTRAN Example Book: The Art of Scientific Computing*. The Art of Scientific Computing. Cambridge University Press, 1992

Prunet, S., Pichon, C., Aubert, D., Pogosyan, D., Teyssier, R. & Gottloeber, S. Oct. 2008, *Initial Conditions For Large Cosmological Simulations*, ApJS, **178**,pp. 179–188

Riess, A. G., Filippenko, A. V., Challis, P., Clocchiatti, A., Diercks, A., Garnavich, P. M., Gilliland, R. L., Hogan, C. J., Jha, S., Kirshner, R. P., Leibundgut, B., Phillips, M. M., Reiss, D., Schmidt, B. P., Schommer, R. A., Smith, R. C., Spyromilio, J., Stubbs, C., Suntzeff, N. B. & Tonry, J. Sept. 1998, *Observational Evidence from Supernovae for an Accelerating Universe and a Cosmological Constant*, AJ, **116**,pp. 1009–1038

Schlegel, D. J., Bebek, C., Heetderks, H., Ho, S., Lampton, M., Levi, M., Mostek, N., Padmanabhan, N., Perlmutter, S., Roe, N., Sholl, M., Smoot, G., White, M., Dey, A., Abraham, T., Jannuzi, B., Joyce, D., Liang, M., Merrill, M., et al. Apr. 2009, *BigBOSS: The Ground-Based Stage IV Dark Energy Experiment*, ArXiv e-prints

Schmidt, F. 2010, *Dynamical masses in modified gravity*, Physical Review D,pp. 1–18

Shaw, D. J. & Mota, D. F. Feb. 2008, *An Improved Semianalytical Spherical Collapse Model for Nonlinear Density Evolution*, The Astrophysical Journal Supplement Series, **174**.2,pp. 277–281

Shaw, L. D., Weller, J., Ostriker, J. P. & Bode, P. Aug. 2006, *Statistics of Physical Properties of Dark Matter Clusters*, The Astrophysical Journal, **646**.2,pp. 815–833

Silverman, B. W.: *Density estimation for statistics and data analysis*. 1986

Smith, T. L. July 2009, *Testing gravity on kiloparsec scales with strong gravitational lenses*, arXiv preprint arXiv:0907.4829,p. 13

Springel, V., Yoshida, N. & White, S. D. M. Apr. 2001, *GADGET: a code for collisionless and gasdynamical cosmological simulations*, New A, **6**,pp. 79–117

Stadel, J. G.: *Cosmological N-body simulations and their analysis*. PhD thesis. UNIVERSITY OF WASHINGTON 2001

Starobinsky, A. A. Oct. 2007, *Disappearing cosmological constant in f(R) gravity*, Soviet Journal of Experimental and Theoretical Physics Letters, **86**,pp. 157–163

Steinhardt, P., Wang, L. & Zlatev, I. 1999, *Cosmological tracking solutions*, Physical Review D

Teyssier, R 2002, *Cosmological hydrodynamics with adaptive mesh refinement. A new high resolution code called RAMSES*, Astronomy and Astrophysics, **364**,pp. 337–364

Teyssier, R., Moore, B. & Martizzi, D. 2010, *Mass Distribution in Galaxy Clusters: the Role of AGN Feedback*, arXiv preprint arXiv:1003.4744v2, **000**.December

Tolman, R. C. Mar. 1934, *Effect of Inhomogeneity on Cosmological Models*, Proceedings of the National Academy of Science, **20**,pp. 169–176

Tweed, D., Devriendt, J., Blaizot, J., Colombi, S. & Slyz, A. Nov. 2009, *Building merger trees from cosmological N-body simulations. Towards improving galaxy formation models using subhaloes*, A&A, **506**,pp. 647–660

Upadhye, A. 2013, *Symmetron dark energy in laboratory experiments*, Physical Review Letters, **60439**,pp. 2–5

Wang, Y.: *Dark Energy*. Wiley, 2009

Waterhouse, T. P. Nov. 2006, *An Introduction to Chameleon Gravity*, arXiv preprint arXiv:0611.816, November,p. 33

Wetterich, C. 1995, *An asymptotically vanishing time-dependent cosmological "constant"*, Astronomy & Astrophysics, **302**,p. 321

Wintergerst, N. & Pettorino, V. 2010, *Clarifying spherical collapse in coupled dark energy cosmologies*, Physical Review D,pp. 1–16

Winther, H. A., Mota, D. F. & Li, B. 2011, *Environment dependence of dark matter halos in symmetron modified gravity*,pp. 1–10

Wojtak, R., Hansen, S. H. & Hjorth, J. Sept. 2011, *Gravitational redshift of galaxies in clusters as predicted by general relativity*, Nature, **477**.7366,pp. 567–569

Zhao, G.-B., Li, B. & Koyama, K. Feb. 2011, *N-body simulations for f(R) gravity using a self-adaptive particle-mesh code*, Physical Review D, **83**.4,p. 044007

Zhao, H., Peacock, J. & Li, B. 2012, *Gravity theories, Transverse Doppler and Gravitational Redshifts in Galaxy Clusters*, arXiv preprint arXiv:1206.5032, 2,pp. 1–4